Universidade do Minho
Escola de Engenharia

Caroline Gomes Moura

Laser assisted printing of micro communication systems for smart implants

janeiro de 2020

UMinho | 2020
Caroline Gomes Moura
Laser assisted printing of micro communication systems for smart implants

Universidade do Minho
Escola de Engenharia

Caroline Gomes Moura

Laser assisted printing of micro communication systems for smart implants

Tese de Doutoramento
Engenharia Mecânica

Trabalho efetuado sob a orientação de
Professor Doutor Filipe Samuel Correia Pereira da Silva
Professor Doutor Rubens Maribondo do Nascimento

janeiro de 2020

DIREITOS DE AUTOR E CONDIÇÕES DE UTILIZAÇÃO DO TRABALHO POR TERCEIROS

ACKNOWLEDGEMENTS

Concluir uma tese de doutoramento marca o fim de uma longa jornada, na maioria das vezes, individual e solitária, o qual não seria possível sem a ajuda de diversas pessoas e instituições a quem aqui deposito os meus sinceros agradecimentos.

Primeiramente, gostaria de agradecer aos meus orientadores Professor Filipe Samuel Silva e Professor Rubens Maribondo, pela oportunidade de trabalho neste projeto, bem como por todos os ensinamentos adquiridos ao longo do caminho de pesquisa, desenvolvimento e conclusão do mesmo. Gostaria ainda de manifestar a minha gratidão ao Professor Filipe por ter me recebido em seu grupo de pesquisa para a realização desse trabalho, o qual considero uma experiência de enorme ganho profissional e pessoal.

Os meus mais sinceros agradecimentos a todos os meus colegas e membros do laboratório pelo acolhimento, pelo agradável convívio, alguns presentes desde o início e outros mais recentes, um muito obrigado por tudo, vocês foram essenciais. Um especial agradecimento ao Professor Óscar Carvalho, que por muitas vezes me orientou e ajudou quando as dificuldades pareciam insuperáveis. Gostaria ainda de expressar a minha gratidão aos meus amigos Flávio Bartolomeu e Rafael Pereira pela amizade e companheirismo sempre, e por terem tornado mais leve essa longa jornada.

Agradeço aos funcionários e técnicos da Universidade que sempre se mostraram disponíveis e prestativos todas as vezes que fui procurá-los.

Agradeço ao CNPq (Conselho Nacional de Desenvolvimento Científico e Tecnológico) e ao governo do Brasil pelo suporte financeiro no consentimento da bolsa 205791/2014-0. Obrigada à FCT (Fundação para a Ciência e Tecnologia) pelo apoio financeiro no âmbito dos projetos UID/EEA/04436/2019 e NORTE-01-0145-FEDER-000018-HAMaBICo.

Por último, mas indispensáveis, gostaria de agradecer ao meu companheiro da vida, David, pelo apoio incomensurável em todos os momentos, pela ajuda e conselhos naqueles dias mais difíceis e por tornar os meus dias mais felizes. À minha filha, Eva, por ser a principal responsável por minha alegria de viver. À minha família, aos meus pais e à minha irmã pelo amor, pelo incentivo e apoio sempre e por compreender a minha ausência durante todo esse tempo.

STATEMENT OF INTEGRITY

I hereby declare having conducted this academic work with integrity. I confirm that I have not used plagiarism or any form of undue use of information or falsification of results along the process leading to its elaboration.

I further declare that I have fully acknowledged the Code of Ethical Conduct of the University of Minho.

RESUMO

Impressão de micro sistemas de comunicação assistida por laser para implantes inteligentes

O mercado de implantes ortopédicos é um dos maiores no campo da medicina, como consequência do crescimento contínuo da população idosa. Apesar dos avanços tecnológicos, o ciclo de vida de um implante dificilmente excede 15 anos. Assim, as soluções mais promissoras para melhorar a vida útil do implante têm sido direcionadas ao desenvolvimento de novos implantes dotados de funções inteligentes. Contudo, o principal desafio tem sido na acomodação desses componentes inteligentes ao longo da superfície do implante, sem modificar significativamente seu design e performance.

Guiado pela versatilidade da técnica de laser e baseado no conceito de implantes inteligentes, este trabalho está relacionado com a impressão de componentes do sistema de comunicação na superfície do implante. Apesar da liga de titânio (Ti6Al4V) ser considerada a escolha final para a fabricação de implantes ortopédicos, os implantes à base de zircônia surgiram como um material alternativo para superar alguns problemas relacionados aos implantes à base de titânio. Com isso em mente, este trabalho apresenta diferentes abordagens para a impressão do sistema de comunicação, considerando sua aplicação tanto em implantes à base de zircônia, quanto em implantes à base de liga de titânio.

Em relação à superfície do Ti6Al4V, os resultados revelaram que a oxidação natural da texturização a laser é suficiente para evitar perdas elétricas dos fios para o substrato metálico. Além disso, quando comparado aos métodos convencionais, o laser revelou-se eficiente na produção de uma camada de óxido com boas propriedades de isolamento, assim como no processo de sinterização do material condutor. Na impressão dos micro-componentes na superfície da zircônia, os resultados demonstraram que, embora tenha sido verificada uma redução na resistência à flexão, a abordagem proposta permitiu imprimir fios à base de prata e micro-antenas com propriedades elétricas satisfatórias. A antena fabricada mostrou resultados de transmissão de energia bem acima do necessário para a comunicação de dados, o qual valida o seu uso para comunicar dados com o mundo externo.

No geral, os resultados deste trabalho de pesquisa demonstraram que é possível imprimir microcomponentes em superfícies metálicas e cerâmicas, por meio de uma abordagem híbrida a laser, através da combinação de processos aditivos (sinterização a laser e oxidação a laser da superfície) e processos subtrativos (maquinagem a laser).

PALAVRAS-CHAVE: Impressão a laser, implantes inteligentes; Nd:YAG laser; Ti6Al4V; zircônia;

ABSTRACT

Laser assisted printing of micro communication systems for smart implants

The market of orthopedic implants is one of the biggest in medicine field, as a consequence of the continuously growing elderly population. Despite the technological advances, the life cycle of an implant hardly exceeds 15 years Thus, the most promising solutions to improve the lifetime of implant have been targeted at the development of new implants endowed with smart functions. However, the most challenge has been in housing the smart components along the surface of the implant without modifying significantly its design and compromising its performance.

Guided by the versatility of laser technique and based on smart implants concept, this work is concerned with the printing of communication system components on implant surface. Although Ti6Al4V titanium alloy is still the actual choice for orthopedic implants fabrication, due to its various excellent properties, zirconia-based implants have emerged as an alternative material to surpass remaining weakness of titanium-based implants. Bearing this in mind, this work presents different approaches for printing the communication system considering its application in both, zirconia-based implants and titanium alloy-based implants.

Regarding titanium alloy surface, the results revealed that the natural oxidation from the laser texturing is sufficient for avoiding electrical losses from the wires to the metallic substrate. In addition, when compared to the conventional methods, laser revealed efficient for producing an oxide layer with good enough insulation properties, as also for sintering process of the conductor material. In the printing of the micro-components on zirconia surface, the results demonstrated that, although a reduction in the flexural strength has been verified, the proposed approach allowed to print silver-based wires and micro-antenna with satisfactory electrical properties. The fabricated antenna displayed power transmission results well above that required for data communication, which endorses its use to communicate data with the outside world.

Overall, the results of this research work demonstrated that is possible to print micro-components in both, metallic and ceramic surfaces, by means of hybrid laser technique that combines additive (laser sintering and laser surface oxidation) and subtractive (laser machining) processes.

KEYWORDS: Laser printing; Nd:YAG laser; smart implants;: Ti6Al4V; zirconia

CONTENTS

FIGURES

TABLES

Aos meus avós Walda e Jehovah

(in memoriam)

Chapter 1 - Scope of the thesis

This chapter aims to clarify the scope of this thesis by enlightening the motivation, the objectives and the structure of the thesis.

1.1 Motivation and objectives

Orthopedic implants are medical devices which are implanted surgically in human body for replacing missing joints and bones or restoring function of a damaged structure. Some examples include orthopedic implants for joint replacement, implants for fixation of the spine and implants for treat fractures.

The market of orthopedic implants is one of the biggest in the medicine field and it is expected to expand significantly in the future, mainly due to the continuously growing elderly population. To date, metallic material is still the ultimate choice for implants production. However, studies have been directed towards the use ceramics as an alternative material, due to their promising properties.

The lifetime of an implant depends on several factors, such as its geometry, physical activity of the patient, and age of the patient. Although the increasing demand for orthopedic implants and the technological advance in this area, their life cycle does not exceed 10-15 years. Among the potential causes of failure are wear, loosening and misalignment.

Thus, the ability to monitor the implant's performance along its use in real time and establish the communication between the implant and the user, could offer capabilities in detecting early implant-adjacent tissues failures and eventually to remedy some issues. These capabilities may be provided by smart implants, which can be defined as a diagnostic tool able to cater information regarding the environment inside the body, for an external receptor.

Recent advances have shown some solutions regarding accommodation of smart components along the implant. However, the creation of huge cavities to adapt these components, besides altering the implant's design and its properties, may compromise its long-term implant-adjacent tissues performance. In this sense, the smart implants concept combined with laser modification (additive/subtractive), is a suitable solution to overcome the recurring challenges of this area.

On the basis of the foregoing, this work aims at developing an alternative approach for printing integrated communication system on implants, similar to biological nervous system. Laser technology was applied as a versatile tool, whether for prepare the material in subtractive way, by creating micro-cavities, or for print smart components, namely wires and antenna, in an additively way. Besides, laser was also applied for thermal-chemical treatments, namely for creating an oxide layer to act as electrical insulation of communication wires.

In order to keep up with the main trends on implants production, the later approach was applied on ceramic and metallic substrates. Thus, the main objectives of this work were:

Definition of strategies to create micro cavities on the metallic and ceramic's surface, by using laser;

Definition of strategies to create insulation layers between the substrate and the communication wire, when necessary as in the case of metallic substrate;

Definition of strategies to consolidate internal communication system in both substrate materials, Ti6Al4V and zirconia;

Definition of strategies to consolidate a communication system implant-user.

1.2 Structure of the thesis

This thesis is structured as a compilation of research papers (published or submitted for publication in international ISI journals). Before this compilation, two chapter are included: Chapter 1 (the current chapter), which is composed by the motivation, objectives and structure of the thesis and Chapter 2 which presents a general state of the art on some topics.

Based upon the foregoing, in order to contextualize the main aspects discussed along of this work, as well as providing to the readers fundamental concepts and a background regarding some key topics, Chapter 2 brings a brief discussion about implants and smart implants aspects, as well as laser technology, including laser surface modification, laser sintering and laser oxidation.

The research papers are presented from Chapter 3 to Chapter 8. Bearing in mind that this work aims to print the communication system in both, metallic and ceramic-based implants, the Chapters are organized accordingly. The studies addressed to the metallic substrate are exposed from Chapter 3 to Chapter 5. On the other hand, Chapter 6, 7 and 8 present the studies related to the ceramic surface. The papers are composed by the following sections: Introduction; Experimental details; Results and discussion and Conclusions.

Chapter 3 is related to the study of laser texturing parameters on the surface modification of Ti6Al4V substrate. In this research, besides the characterization of the surface, the oxidation from the laser texturing was also evaluated regarding the electrical insulation property. This paper is published in the Journal of Materials Science and Engineering C (impact factor of 4.959, Q1).

Chapter 4 presents the laser printing of the silver-based wires on Ti6Al4V substrate. This paper assembles the best strategy in the micro cavity creation, based on previous study, with the different strategies of surface oxidation, for insulation performance, and the ideal laser sintering approach for the wires printing. Besides, conventional methods for both, surface oxidation and sintering of material, were tested in order to compare with laser approach. This work is under revision in the Journal of Optics and Laser Technology (impact factor of 3.319, Q1).

After printing the wires for the communication system on Ti6Al4V substrate, Chapter 5 is concerned the printing of the antenna on titanium alloy substrate. A laser approach was employed for the antenna production and performance of the fabricated antenna (real condition) was assessed by simulation and compared with the ideal condition. This work is submitted to Bionsensors and Bioelectronics (Impact factor 9.51, Q1).

Chapter 6 reports the printing of the silver-based wires on zirconia substrate. In this work, laser was employed both to create the micro cavities (subtractive) and to consolidate the material within them (additive). The electrical performance of the printed wires was also presented. This work is under revision in the Journal of Optics and Laser Technology (impact factor of 3.319, Q1).

Chapter 7 deals the printing of the antenna on zirconia substrate, based on the conditions studied on the previous work (Chapter 6). The performance of the antenna was assessed concerning its signal transmission capacity into a representative human body environment. This work is submitted to Bionsensors and Bioelectronics (Impact factor 9.51, Q1).

Considering the ceramic's brittleness and the efforts that ceramic-based implant is subjected during its insertion, Chapter 8 deals the evaluation of laser textures on ceramic surface regarding the primary stability, while mimics the efforts during the implant's insertion. This paper is published in the Journal of Ceramics International (impact factor of 3.450, Q1).

Chapter 9 presents the general conclusions drawn from this work and in addition some perspective for future works.

Chapter 2 - Introduction

This chapter aims to provide to the readers fundamental information about the main aspects discussed in the following chapters that will make easier the understanding of the research developed in this work. Accordingly, this chapter gathers fundamental about orthopedic implants, biomaterials for implants, smart implants and laser technology.

2.1 Implants

Medical implants are manmade devices or tissues that are placed over or inside the surface of the body for replacing the missing or damaged biological structure [1]. The global implant market has a growth expectation at an annual rate of 7.07% during the forecast period 2018-2023. The main reasons for the increase of medical implants market are the rising prevalence of the chronic disease, improvement of surgical outcomes, acceptance of medical implants devices by patients and the increase of aging population around the world. It has been estimated that 90% of the population over the age of 40 suffers from these kinds of degenerative diseases. Artificial biomaterials are the solutions for these problems, as surgical implantation of these artificial biomaterials of appropriate shapes helps in restoring the function of the otherwise functionally compromised structures. There is tremendous increase in the demand for the new long lasting implants, as the data collected on total joint replacements surgery it is estimated that by the end of 2030, the number of total hip replacements will rise by 174% (572,000 procedures) and total knee arthroplasties is projected to grow by 673% from the present rate (3.48 million procedures) [2].

The main reasons for joint replacements are attributed to diseases such as osteoporosis (weakening of the bones), osteoarthritis (inflammation in the bone joints) and trauma. Not only the replacement surgeries have increased, but also the revision surgery of hip and knee implants. These revision surgeries besides being expensive and exhibiting low success rate, also cause pain in the patient. The total number of hip and knee revision surgery is expected to increase by 137% and 607%, respectively, between 2005 and 2030 [2]. Thus, a very high boom in implant manufacturing is expected in the coming years. The various causes for revision surgery are depicted in Figure 2.1.

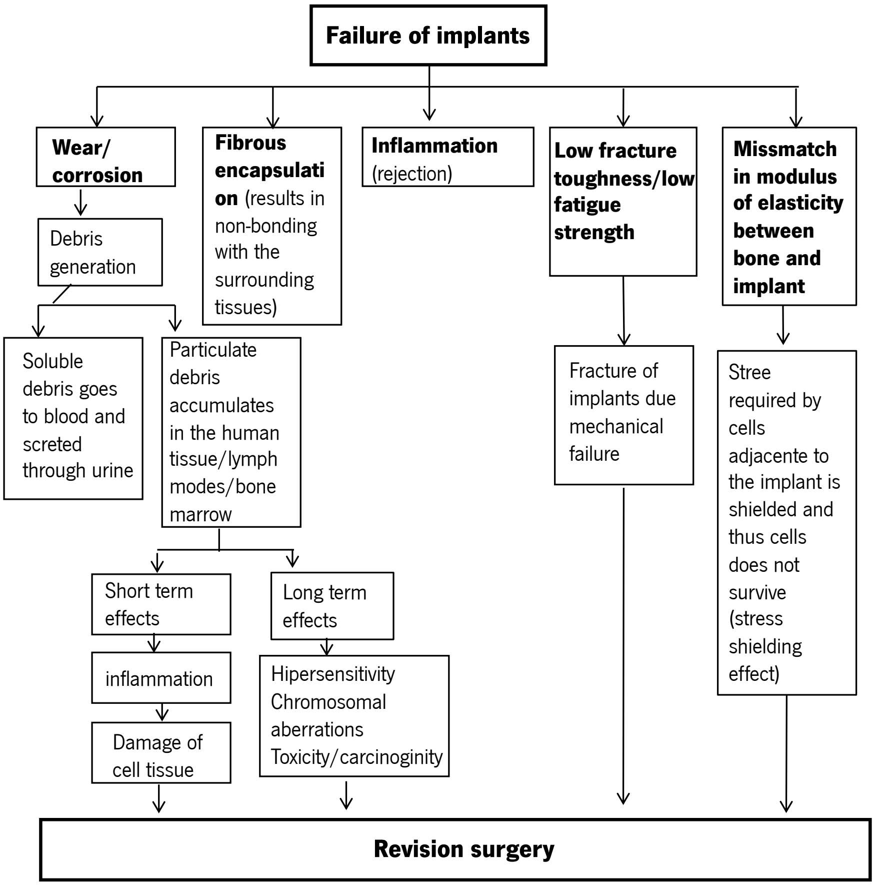

Figure 2.1 Various causes for failure of implants which leads to revision surgery [3].

In this scenario, America dominates the global implants market owing to the increase of chronic diseases. Furthermore, high health care spending and the geriatric population increasing are likely to fuel the growth of the market. However, the saturation of the market, as well as the high cost of the devices and changing reimbursement policies may slow the market growth over a period. In Europe, the medical implants market occupies the second position of the global market due to the increased support from the government, the presence of huge geriatric population and high care spending. Additionally, many Europeans countries have encouraged the manufacturers for research and development of advanced devices.

There are two types of orthopedic implants, namely the permanent implants and temporary implants. The permanent orthopedic implants include different types of total joints like the hip, knee, ankle, shoulder, elbow, wrist, and finger joints [4]. Additionally, permanent orthopedic implants are expected to serve in the human body throughout the life span of the patients. Particularly, hip and knee joint prostheses have experienced rapid development and clinical acceptance in recent years. However, the delicate articulation and complicated load transfer make such prostheses very difficult to design.

The temporary orthopedic implants are used to fix broken or fractured bones during the healing process. They includes plates, screws, pins, wires, and intramedullary nails [4], and are supposed to serve for a relatively short time just long enough to let bones heal. One major concern of bone healing is the bone weakening mainly due to the stress-shielding effect, which is also an important concern for permanent implants. The stress-shielding occurs when metal implants, such as bone plates and screws, are used to repair fractures or for joint replacement surgery. Although rigid metal plates stabilize the fracture site and allow early weight bearing and patient mobility, the higher stiffness of the implant results in bone loss due to a physiologic loading decrease of the bone. According to Wolff's law [5], if a larger load is applied to the bone over a period of time, the osteogenic (bone generating) process is more effective and produces better support for the load. In contrast, a reduced load to the bone induces loss of bone mass.

As stated, the orthopedic implants aim is to restore the structural integrity and functionality of damaged joints and bones. Thus, to produce an implant with a long lifetime and without inducing rejection, the biomaterials should present some desirable characteristics, such as mechanical properties, wear resistance, corrosion resistance, biocompatibility and osseointegration [4].

In relation to mechanical properties for orthopedic implant materials, they are related to the intended working conditions and specific applications. Among the mechanical properties, Young's modulus, yield strength, ultimate tensile strength, fracture toughness, and elongation at break are the five most important. If the materials of the implant have a Young's modulus higher than that of the human bone, stress transfer to the adjacent bone will be prevented, which leads to bone resorption and implant loosening. Thus, the implant materials should have Young's modulus similar to that of the human bones. Another important mechanical requirement for orthopedic implants is the fatigue strength, from the perspective of cyclic local loading, especially joint replacements of the hips, knees, and ankles [4].

2.2. Materials for implants

The most common materials used in orthopedic implants are the metals, due to the proper strength, ductility, fracture toughness, hardness, corrosion resistance, and biocompatibility. The common biomedical metallic alloys can be categorized into several groups, such as stainless steels, Co-based alloys, Ti-based alloys, and biodegradable alloys - Mg-based alloys. The materials of the first three groups have been approved by the US Food and Drug Administration and are currently used in orthopedic implants.

Ceramic materials are commonly used as articular components in total joint replacement but due to their poor ductility, they have not been applied to fracture fixation applications. Ceramics possess excellent wear resistance, high compressive strength, inherent chemical inertness and biocompatibility. The most commons ceramic used in orthopedic implants are Al_2O_3 (alumina), ZrO_2 (zirconia) and silicon nitride (Si_3N_4).

Despite the above brief discussion regarding the materials commonly used in orthopedic implants, this work will be focused on two of them, namely Ti-6Al-4V and zirconia.

2.2.1 Ti-6Al-4V

Pure titanium (Ti) exists as a hexagonal close-packed structure (α phase) up to 885 °C and a body-centered cubic structure (β phase) above this temperature.

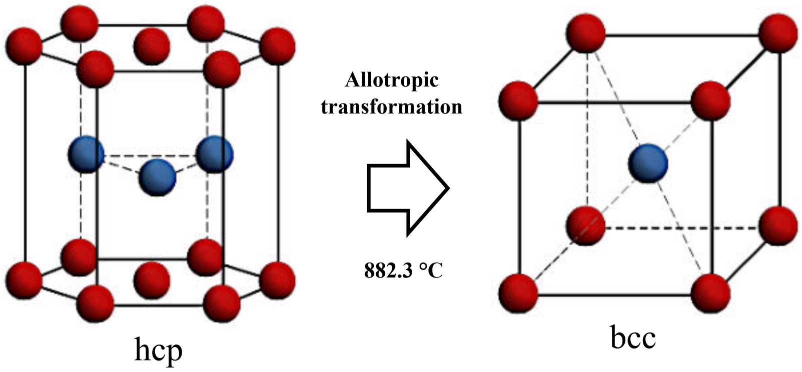

Figure 2.2 Schematic illustration of α → β phase allotropic transformation

In terms of microstructure, Ti-based materials are classified as commercial purity titanium (CP, Ti > 99%) - grades 1 - 4 of ASTM classification, depending on maximum oxygen, carbon, nitrogen, hydrogen, and iron impurities - and titanium alloys, grade 5 - 38 [6]. Titanium alloys, in turn, are classified according to their position in the β isomorphous phase diagram as α, near α, α+β, metastable β and stable β (Figure 2.3).

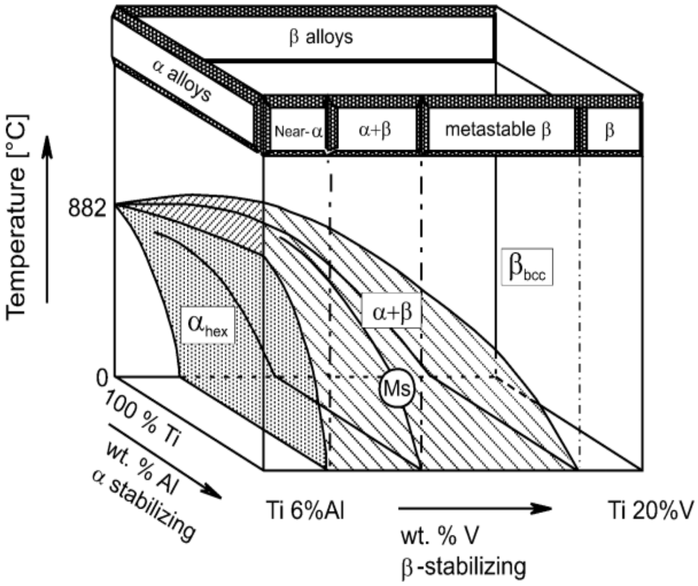

Figure 2.3 Schematic three-dimensional phase diagram for classification of titanium alloys (Taken from [7]).

α alloys: Comprises four grades of commercially pure titanium (Ti-O alloys where O varies between 0.18 – 0.40 wt.% from grade 1 to 4) and alloys with exclusively α stabilizing. Due to their lack of heat treatment response, strengthening by solid solution and cold working are usually applied. Moreover, they are especially suitable for the chemical industry owing to their excellent corrosion and creep resistance.

Near α alloys: contain a smaller amount of β-stabilizers (up to 2 wt.%) forming less than ~ 10 vol.% of β phase. These alloys combine high creep resistance with good strength levels and are mainly used for high temperature applications (~ 500 –550 °C) in the aerospace industry.

α+β alloys: Present additions of β stabilizers of 4 –6 wt.% leading to 5 –40 vol.% fractions of β phase at room temperature. Martensite transformation occurs upon fast cooling from the β phase field to room temperature. These alloys can develop a wide variety of microstructures, i.e. different mechanical properties, by applying different thermal and thermomechanical treatments. Amongst the α+β alloys, the Ti-6Al-4V alloy is one of the first made titanium alloys and the most commercialized nowadays (absorbs more than 50 % of the global market). It has a chemical composition of 6% aluminum, 4% vanadium, 0.25% (maximum) iron, 0.2% (maximum) oxygen, and the remainder titanium. These alloy elements make its microstructure composed, at room temperature, of 91% of α phase and 9% of β phase (Figure 2.4). It is significantly stronger than commercially pure titanium while having similar thermal properties. In addition, it represents the most developed and tested titanium alloy that, at the same time, offers a well-balanced property profile [8].

Stable β alloys: comprise very high addition of β stabilizers (around 30 wt.%) and are constituted by single β phase. β alloys possess a BCC crystal structure, which is readily cold-worked (better than HCP α structure) in the β-phase field. The microstructure after quenching contains equiaxed β- phase. Commercial alloys are not included in this group.

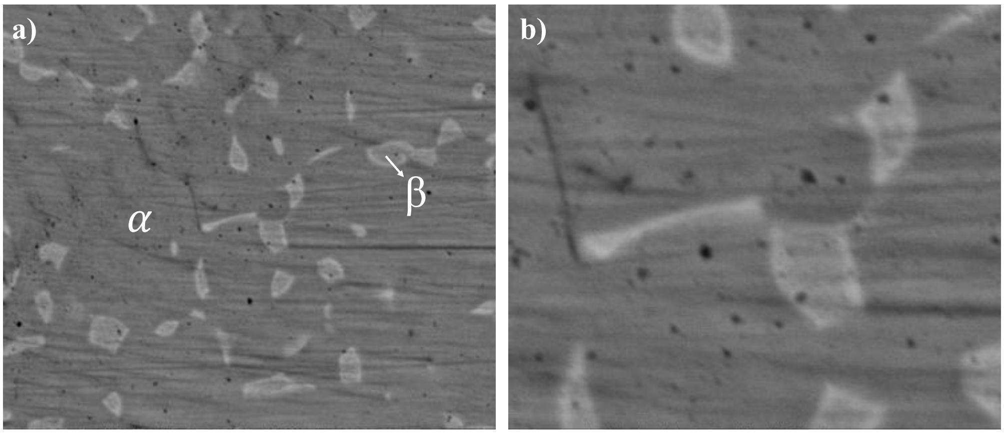

Figure 2.4 Micrographs of as received commercial Ti-6Al-4V titanium alloy at two different magnifications, showing alpha and beta phases. a) 15.000x, b) 50.000x.

The most utilized titanium alloys are summarized in Table 2.1, together with their mechanical properties and composition.

Table 2.1 Mechanical properties and composition of main titanium alloys; grade 2 CP titanium is also exhibited for comparison [6].

				Composition					
	Tensile strength (Mpa)	*0.2% proof stress[a] (Mpa)*	*E[a] (Gpa)*	*Al*	*Sn*	*Mo*	*V*	*Ni*	*Other*
Grade 2 (CP)	485	345	105	–	–	–	–	–	
Grade 5 (α+β) Ti-6Al-4V	985	885	105	6	–	–	4	–	
Grade 6 (α) Ti-5Al-2.5Sn	860	825	110	5	2.5	–	–	–	
Grade 7 (CP) Ti-0.15Pd	430	345	105	–	–	–	–	–	0.15Pd
Grade 9 (α) Ti-3Al-2.5V	650	550	105	3	–	–	2.5	–	
Grade 12 (α) Ti-0.3Mo-0.8Ni	600	460	105	–	–	0.3	–	0.8	
Grade 21 (β) annealed Ti-15Mo-3Nb-3Al-0.2Si	915	880	83	3	–	15	–	–	3Nb, 0.2Si
Grade 21 (β) aged	1310	1210	102	3	–	15	–	–	3Nb, 0.2Si

[a] Data from TIMET Titanium metals coorporation

As above mentioned, among the first-generation $\alpha - \beta$ alloys, Ti–6Al–4V (Ti64) is the most extensively used orthopedic alloys. The Al addition is to stabilize the α phase by increasing the transformation temperature from α to β phases, while V stabilizes the tougher β phase by lowering the temperature of the β transformation. The fatigue strength is higher than that of 316L stainless steel and comparable with that of Orthinox and Co-based alloys. The strength of the titanium alloys is very close to that of 316L SS, and its density is 55% less than steel, hence, when compared by specific strength (strength per density), the titanium alloys outperform any other implant material. Although Ti6Al4V has an excellent reputation for corrosion resistance and biocompatibility, the long-term performance of this alloy have presented some issues regarding aluminum and vanadium ions release.

2.2.2 Zirconia

From low to high temperature, pure zirconia (ZrO_2) exhibits three phases, namely monoclinic, tetragonal and cubic structures, which are of interest to biomedical applications. The monoclinic phase exists below 1170 °C. As the temperature increases, it transforms to tetragonal phase, at approximately 1170 °C, and then the cubic phase at around 2370°C, up to the melting point of 2716°C (see Figure 2.5). The changes in volume and shape on cooling associated with the transformation make pure zirconia unsuitable for biomedical applications. However, with the discovery of transformation zirconia toughening, the engineering applications of zirconia was promoted. In the beginning, metallic oxides (CaO, MgO, and Y2O3) were added to zirconia to stabilize the tetragonal phase under the metastable conditions at room temperature [9].

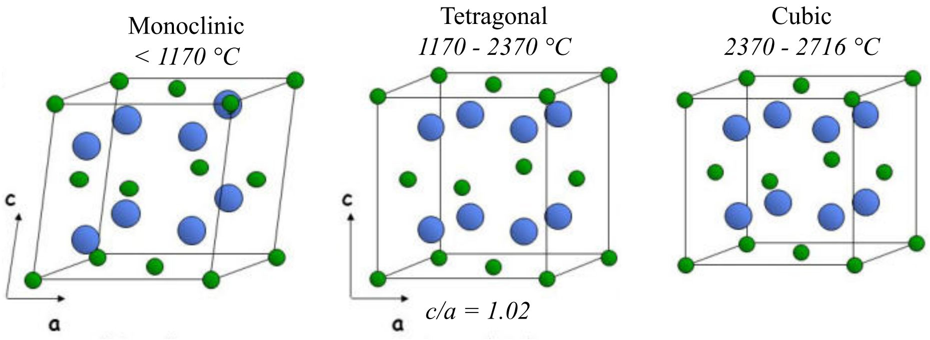

Figure 2.5 Schematic illustration of the three zirconia polymorphs.

Garvie et. al (1975) [10] reported MgO-partially stabilized zirconia (Mg-PSZ) with increased toughness arising from the spontaneous transformation of the metastable tetragonal phase into the more stable monoclinic phase under mechanical stimulation, for instance stress at crack tips associated with a large volume expansion of the structure. This volume expansion, in turn, induces compressive stress and retards the crack propagation, increasing the strength and toughness. Thus, Mg-PSZ was the first zirconia to be used in orthopedics, but no large-scale application has occurred. Afterwards, Yttrium-stabilized zirconia, called yttria (Y_2O_3) - tetragonal zirconia polycrystal (Y-TZP), was developed using Y_2O_3 as the stabilizer and almost completely formed by tetragonal grains at room temperature [11]. Thus, in the 1990s, Y-TZP became the materials of clinical choice for large-scale industrial production of hip joint femoral heads because of the higher strength and toughness than Mg-PSZ and CaO-PSZ. The transformation toughening mechanism of Y-TZP is responsible for enhancing mechanical properties including high fracture strength, which is twice that of high-density alumina and high flexural strength. Young's modulus of zirconia is smaller than that of alumina and similar to those of Ti-based alloys enabling the metal-to-ceramic design transformation.

Biomedical grade zirconia usually contains 3 mol% yttria (Y_2O_3) as a stabilizer, known as 3Y-TZP. While the stabilizing Y3+ cations and Zr4+ are randomly distributed over the cationic sites, the electrical neutrality is achieved by the oxygen vacancies created [12]. Zirconia also has excellent biocompatibility, and 3Y-TZP has been used to manufacture femoral heads in total hip prostheses [4], but its use has been extremally reduced due to a series of failures that occurred in 2001. So, because of the metastability of the tetragonal phase at room temperature, zirconia suffers from a mechanism, known as low-temperature degradation (LTD), in which the transformation of the surface occurs in the presence of water, causing microcracking and roughening [13] (See Figure 2.6). The low temperature degradation (LTD) of zirconia is well-documented phenomenon in literature [14,15]. As shown in Figure 2.5 by Chevalier (2006) this nucleation of the transformation leads then to a cascade of events: the transformation of isolated grain results in a volume increase stressing up the surrounded grains and microcracking. This offers a free path for water penetration into the specimen. The consequences of this aging process are multiple and include surface degradation with grain pullout and microcracking, as well as strength degradation.

According to Chevalier (2006) [16], although LDT is associated with the case of several femoral head prosthesis failures in 2001, there seems to be no clear relationship between LDT and failure predictability when zirconia is used as a biomaterial. Moreover, although intrinsic aging of Y-TZP cannot be eliminated, it can be minimized by controlling the manufacturing process to refine the grain size, increasing the density, reducing the porosity, and avoiding residual stress [17].

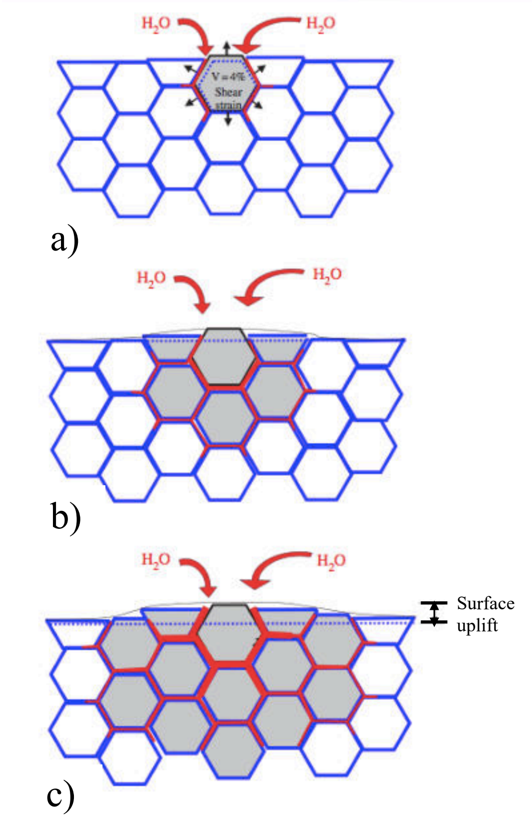

Figure 2.6 Schematic illustration of the ageing process occurring in a cross section, showing the transformation neighbor to neighbor. (a) Nucleation on an isolated grain at the surface, leading to microcracking and stresses to the neighbor's grains. (b) The transformed zone growth, leading to extensive microcracking and surface roughening. Transformed grains are gray. The red path represents the penetration of water due to microcracking around the transformed grains. Taken from Chevalier, 2008 [16].

The mechanical properties of 3Y-TZP strongly depend on its grain size, in which above a critical grain size, 3Y-TZP is less stable and more suitable for t-m transformation. On the other hand, smaller grain sizes are associated with lower transformation rates [18]. When the microstructure present grains around 0.2 - 0.5 μm of diameter, the flexural strength can be in a range of 800 - 1000 MPa and a fracture toughness of 6 - 8 MPa $m^{0.5}$.

2.3. Smart Implants

2.3.1 Introduction

According to Ledet et. al [19], smart implants are implantable devices that provide not only therapeutic benefits but also have diagnostic capabilities. As diagnostic tools, smart implants can provide information regarding the environment inside the body. The transmitted information can provide qualitative data to start treatments and detect eventual problems earlier [1,20]. In all smart implant applications, the implant is the vehicle that carries the diagnostic technology into the body, as can be seen in schematic examples of a total knee replacement, in Figure 2.7. Due to the possibility to integrate sensing technology, there has been much innovation and development in the smart orthopedic implants in the last five decades.

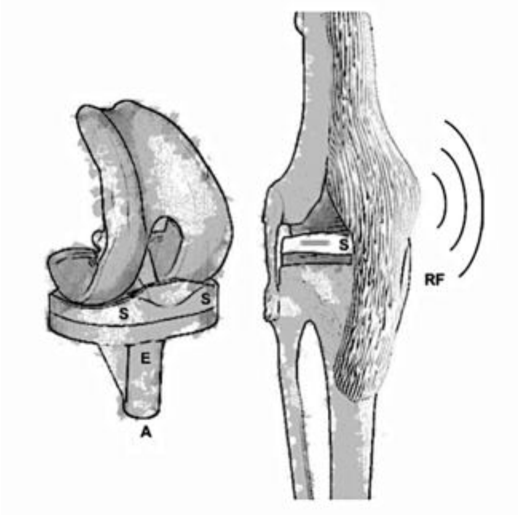

Figure 2.7 Schematic illustration of total knee replacement components (left), have sufficient size and volume for placement of sensors (S), electronics (E) and antenna (A) components within. Once placed in the body (right), radiofrequency (RF) communications facilitate data collection from the implant. (Taken from Ledet et al.) [19].

Inside the implant, the typical smart components include strain gages, a power coil for inductive coupling, an antenna for transmitting data, signal conditioning circuits and a telemetry system. External readers generate a radio-frequency (RF) signal that is transmitted through an external antenna to the implanted system. Strain gage-based sensing has been the mainstay smart implant since the 1960s. The gage is bonded directly to the surface of the implant with an adhesive and, as the implant deforms, the strain gage deforms equivalently. This deformation causes a characteristic change in the resistance of the gage, which is proportional to the strain experienced by the implant. However, protecting strain gages circuits from the bodily fluid remains a challenge [21,22]. The strategy used to overcome this challenge is to modify the implant design in a way where the gages are mounted inside the implant [21,23]. In most of the cases of smart implant applications, the implant is modified by creating a cavity, in which the strain gages can be placed [24,25].

Despite decades of research and advances, smart implants have not yet become a part of daily clinical practice, due to the number of limitations and challenges that still have to be overcome in this research field. In order to reduce the size and signal conditioning circuits, microelectromechanical systems (MEMS)-based technology has been used for smart implant applications [26,27]. The most attractive of MEMS is their microscale components and the well-established fabrication methods. Thus, it seems that the most significant barrier to integration into clinical practice has been the necessity for host implant modification to accommodate the smart components. The creation of cavities to adapt these components is challenging and expensive, besides alters the implant design, which may alter the implant's properties and consequently, compromises its performance [28]. Smart implants for the next generation should be simple, small, efficient and must be integrated with the implant with little to no modification to existing implant design.

2.3.2 Sensors and actuators

Fundamentally, a sensor requires a material that exhibits a detectable, reproducible response to a change in the environment, namely temperature, pressure, acceleration, humidity, chemical or gas composition, and light level. Most of the useful sensor materials generate an electrical signal, such as a current or a voltage, or a change in the electrical properties such as resistivity, capacitance, or remnant polarization that can be calibrated for the change in the environment. The development of an actuator requires a material (or a system) in which there is a large, controllable response to an applied stimulus. An actuator can convert electrical signals into physical phenomena. For many actuators, the desired response is a useful motion [29].

Several materials can work as sensors and actuators, simultaneously, improving their performance in the environment where they are inserted. These materials can alter their properties in response to changing surroundings and with these changes, the sensors can act according to the needs of the intended application [30]. These materials include piezoelectric and shape memory alloys (SMA). Some examples of these materials and their respective applications are shown in Table 2.2.

Table 2.2 Examples of smart materials and their applications.

Materials		Applications	
Piezoelectrics	Shape memory alloys	Sensors	Actuators
Lead zirconate titanate – PZT	NiTi based alloys (NiTiCu, NiTiPd, NiTiFe)	Accelerometers, pressure transducer, force transducer, noise/acoustic sensor, sensor health monitoring, etc.	Precision manipulator, pressure generator, displacement actuator, self-sensing actuator, active structures, etc.
Barium titanato - BaTiO3	Cu based alloys (CuZn, CuZnAl, CuAlNi, CuAlNiMn)		
Polyvinylidene fluoride – PVDF	Polymers: PTFE, PU, Pe		

2.3.3 Antenna/ Communication system

Having in mind the orthopedic implant applications, after integrated and accommodated in the implant, the smart components should be able to transfer their measurements to some central data storage, as also receive commands from this central. Through this data transfer the communication between the smart components and the implant's user is stablished, which ultimately ensure that any problem with the implant is informed directly to the user. This communication can be performed by an antenna, which is able to transmit a signal into the body or pick up a signal from the body, trough the electromagnetic waves propagation [31]. To be printed on the implant surface, the antenna should be small and requires very low power. However, these requirements make difficult the data transmission by an implanted device. Thus, designing an efficient antenna is very important for a reliable implanted communication system [31]. The antenna is included in the implantable medical device (IMD) concept, in which are placed inside the human body by means of surgical operation and may serve all sorts of sensing and stimulating functionalities. Their remarkable feature is the bidirectional link between the implant and its user, enabling medically useful data to be transmitted both ways, and hence playing a key role in the implant durability. Several examples and a vast number of implantable medical technologies can be found in the literature [32–34].

Unlike traditional antennas that operate in free space, the implantable antennas should consider many kinds of requirements as an implantable antenna are placed in human bodies, such as the antenna size (miniaturization), the antenna efficiency (tissue losses) and its biocompatibility. These issues regarding the in-body antennas operation will be briefly commented below.

It is known that decreasing the electrical size of an antenna will lead to a decrease of its electromagnetic performances [35]. A study conducted by Harrington [36] demonstrated that the antenna efficiency is directly proportional to its electrical size and, thus high operating frequencies are required for geometrically small but efficient antennas. Hence, based on this theory the antenna efficiency significantly decreases if lower operating frequencies are used. Despite, recent advances in the technology of implantable medical devices have led to ultra-small designs, driving for a good compromise between size and performances.

All these studies consider however lossless miniature antennas radiating into free space. In the case of implantable antennas, we have an important change of paradigm as the antenna is directly surrounded by loss biological tissues. The main quality criterion in the design of such antennas is the amount of power the antenna is able to transmit out of the host body. The efficient design of such antennas will thus have to take into account the host body and will have to develop specific strategies in order to achieve this goal [35]. Signal losses are an undesirable and inevitable aspect of electromagnetic wave propagation. The human body is not the ideal medium for radio-frequency signal propagation since electromagnetic radiation propagation depends heavily on the tissues water concentration due to the water poor conductivity (~5.5×10^{-6} S/m). Notwithstanding, as the human tissue is more conductive than the air, there are higher losses due to attenuation [31].

The implantable antennas must be biocompatible in order to preserve patient safety. The most common approach to ensure the biocompatibility of the antenna is to cover the structure with a superstrate dielectric material. At the same time, this approach separates the antenna from the body tissue. The most usual materials used as dielectric is Teflon (εr = 2.1; dielectric loss tangent, tan δ = 0.001) and ceramic alumina (εr = 9.4; tan δ = 0.006) [37]. In the current thesis, since the antenna will be printed on the implant surface, the biocompatibility role will be executed by the implant material itself. In addition, for the conventional implants (metal-based substrate), the antenna should be isolated from them, as well as from the body environment. This can be accomplished by using an insulator layer between the antenna and the substrate. It is also important that this insulator layer be a biocompatible material. Because of its electrical properties, zirconia is the best candidate material for a biocompatible insulation layer. Its high permittivity and low loss-tangent values ($\varepsilon r = 29$; $\tan \delta \approx 0$) [35] allow the near fields of the antenna to concentrate in the metal-based antenna path, thus mitigating power loss [38]. Besides, the thickness of the insulation layer is another important factor in antenna design, since the computation of its optimum value is considered to be highly significant to minimize power loss without increase the antenna size [39].

All the aforementioned smart implants, namely, sensors, actuators and antenna should be integrated so that communication is stablished among them. Through this communication, the sensors can transmit a signal to the antenna, which in turn reports the matter to the user. After receiving the information, the user can send back a command in order to trigger the actuator or sensor, which can counteract the reported issue via the releasing of medicines, for instance. The communication among the smart components may be performed by wires made of a material, also printed in the implant surface, able to conduct electricity. One of the main challenge tasks within this approach deals with electrical losses from the wires to the conventional implants, which are also made of a conductive metallic substrate. This issue can be circumvented by the projection of an insulator layer between them.

The next topics will address both the materials used as conductors (the wires), as well as the insulating layer.

2.4. Communication system printing

2.4.1. Materials for communication system (Silver)

Among the conductor's materials, silver presents the greatest electrical conductivity of all metals, with a resistivity of 1.6×10^{-8} ohm.m. Silver is an extremely soft, ductile and malleable transition metal and crystallizes in a face-centered cubic lattice. The only downside is its high cost, which often restricts its application. Silver is stable in pure air and water; the presence of ozone or hydrogen sulfide or sulfur in the air or water may result in silver tarnishing [40] due to the formation of silver sulfide. The most common oxidation states of silver are 0 and +1, but other oxidation states (+2 and +3) are also known. Silver has a specific gravity of 10.5 and a melting point of 960 °C [41].

In the electronic field, silver is widely used for printing circuit boards and keyboards as an electrical contact. Other applications include the preparation of active waveguides in optical devices [42], inks for printed circuit boards [43], optoelectronics, nanoelectronics (such as single-electron transistors, and electrical connectors) and so on. Silver particles are also used for production conductive paste for electronic packaging [44].

The medical properties of silver have been explored for over 2000 years. In this field, silver has always been used against various diseases; in the past, it found use as an antiseptic and antimicrobial against Gram-positive and Gram-negative bacteria [45–47] due to its low cytotoxicity [47]. The US Food and Drug Administration approved silver solutions in the 1920s to be used as antibacterial agents. Silver products have strong inhibitory and bactericidal effects in a wide spectrum of antimicrobial activities. The action mechanism is due to the silver ions which cause the protein precipitation and acts directly in the cytoplasmic bacterial cell membrane, carrying out bactericidal action immediate [48]. Although silver itself is not considered toxic, most of its salts are poisonous, due to the anions involved. The exposure to silver in the air should not exceed 0.01 mg/m^3 [49]. Because of their great surface area, silver nanoparticles present physical, chemical and biological properties markedly different from those of the bulk material of origin [50,51].

Despite several mechanisms of antibacterial effect of silver ions have been proposed by different authors, the mechanism of action is not yet fully elucidated, as well the toxicity effects of silver for human body. According to literature, at minimal and reasonable concentrations of silver, there are no side effects on human body [49]. Some studies reported cytotoxic effects on human health under prolonged exposure to silver nanoparticles, such as the onset of some diseases [52]. Other studies reported that low concentration is required to kill bacteria without presenting any cytotoxic effect [53,54].

Therefore, joining the great electrical properties of silver and considering its good acceptance in the biomedical field, this material seems to be a promising choice to compose the communication system of implants as a conductive path for where the electrical current flow.

2.4.2. Electric insulator materials (Ti-oxide)

The electrical conductivity of material depends on the amount of charges carriers per volume, the charge and their mobility. The main charge carriers in a solid are the electrons. In an isolated atom, an electron occupies determined levels and sub-levels of energy. In a crystal that has millions of atoms, the levels of energy are overlapped and are replaced by densely filled bands [55,56]. Figure 2.8 presents the energy band for metals, semiconductors and insulators materials.

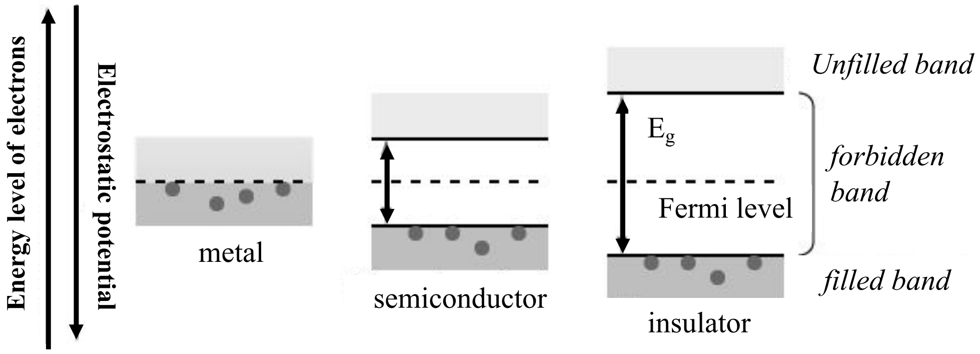

Figure 2.8 Diagram of the energy band gaps of materials.

In conductors' materials, the valence band is either not fully occupied with electrons, or the filled valence band overlaps with the empty conduction band. Generally, both states occur at the same time, so, the electrons can move inside the partially filled valence band or inside the two overlapping bands. In conductors, there is no band gap between the valence band and conduction band. Besides, any fact that makes difficult the electrons motion decreases the electrical conductivity, such as defects in crystalline structure and thermal vibration.

In insulators materials (such as polymers and the majority of ceramics), the valence band is fully occupied with electrons due to the covalent bonds. The electrons cannot move because they're "locked up" between the atoms. To achieve a conductivity, electrons from the valence band have to move into the conduction band. This prevents the band gap, which lies in-between the valence band and conduction band [55,56].

In the semiconductors, the band gap is too small compared with the insulators that even at room temperature electrons from the valence band can be lifted into the conduction band. The electrons can move and act as charge carriers. In addition, each electron also leaves a hole in the valence band behind, which can be filled by other electrons in the valence band. Thus, one gets wandering holes in the valence band, which can be viewed as positive charge carriers. At a certain temperature, an equilibrium is arranged between the electrons elevated to the conduction band and the electrons falling back. With increasing temperature, the number of electrons that can leap the band gap is increased, and thus increasing the conductivity of semiconductors [55,56].

Among the semiconductors materials, Titanium oxide (TiO_2) is one of the most studied transition metal oxide semiconductors due to its nontoxic nature, chemical stability and commercial availability at a low cost. Because of its properties, TiO_2 have been attracted interest in several applications such as photovoltaics [57], spintronics [58] and gas sensors [59]. Most of these applications depends on the remarkable electrical properties of TiO_2. As electrical insulating TiO_2 has an extremely resistivity above 10^8 Ω.m with a wide band gap of about 3.0 eV [60]. The control of these properties can be achieved by controlling the synthesis method, the temperature and environment nature (such as gas nature and partial pressure) [61].

Titanium dioxide, the only oxide of titanium that occurs naturally at atmospheric pressure, exhibits three polymorphs, namely: rutile, anatase and brookite [62]. Rutile is the unique stable phase, while anatase, and brookite are metastable at any temperature. Anatase is kinetically stable at lower temperatures but converts to rutile at temperatures in the range of 600 ° C to 800 ° C. Figure 2.9 presents the titanium oxide rutile (Figure 2.9a) and anatase (Figure 2.9b) phase.

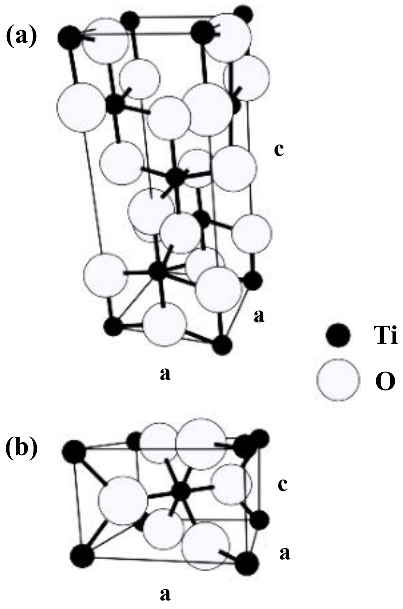

Figure 2.9 Unit cell of anatase (a) and rutile (b) phases of TiO_2. The light circles represent oxygen and the darker circles are titanium. Both forms are tetragonal with lattice constants a and c of 0.4594 nm and 0.2958nm for rutile and 0.3785 nm and 0.9514 nm for anatase. Adapted from [63].

Several methods to obtain titanium oxide have been reported, such as sol-gel synthesis [64,65], hydrothermal [66,67], chemical vapor deposition - CVD [68] and physical vapor deposition - PVD [69]. Generally, in the synthesis of TiO_2 films by several methods, the initial crystalline phase formed is anatase. This can be explained by the less-constrained molecular construction of anatase relative to rutile [70]. In contrast, from a thermodynamic perspective, the faster recrystallization of anatase could be due to the lower surface free energy of this phase, despite the lower Gibbs free energy of rutile [71]. The generation of TiO_2 phases depends significantly on the synthesis parameters, which in turn, affect the product. The kinetics of these processes usually are considered in terms of temperature and time. All the mechanisms involved in anatase to rutile phase transformation are well described in [62].

2.4.3 Ti alloy oxidation and alpha-case formation

Metal oxidation is a special type of degradation of metals which occurs when the metal is subjected to oxygen and/or other oxidizing environment. Most metals in ambient conditions are thermodynamically unstable. The metal's instability may be of little or no practical meaning at room temperature because of the slow reaction rate, but at elevated temperatures the instability of the metal increases rapidly. The process of metal oxidation at high temperature is an important broad field from scientific and technological point of view. It is important to know the oxidation reaction and the subsequent product of the reaction, as well as, the kinetics and the mechanisms of the oxidation process. The oxidation of metals usually results in oxide scale formation and may also cause embrittlement due to dissolution of the gas species (i.e. oxygen) into the metal substrate [72,73]. This oxide scale and subsurface oxygen enriched layer formation can be described by the Wagner's model for high-temperature oxidation of metals [74]. The overall oxidation reaction includes oxide formation and inward oxygen diffusion in the titanium. The oxygen diffusion results in the formation of an oxygen enriched layer beneath the oxide scale, commonly known as alpha–case layer. Alpha-case is defined as a continuous hard and brittle layer that is formed because of oxygen diffusion into the hexagonal closed-packed crystal structure of α-Ti. The name alpha-case originates from the fact that oxygen is a strong α-stabilizing element and its elevated content in titanium and its alloys promotes increase of the β-transus temperature and triggers phase transformation of the retained β-phase to α-phase. The simultaneous oxide scale and alpha–case formation can be described by the Wagner's model [74]. Figure 2.10 schematically shows the oxygen concentration profile during oxide scale and oxygen enriched layer formation as suggested by the Wagner's model.

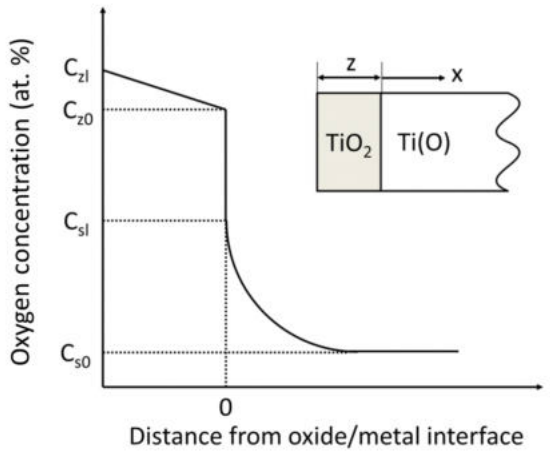

Figure 2.10 Oxygen concentration profile of oxidized titanium according to Wagner's model [74].

As shown in Figure 2.10, the oxygen concentration profile is composed of two individual concentration profiles, one for the oxide (TiO_2) and the other one for the oxygen diffusion layer i.e. alpha–case layer. Both profiles have specific thicknesses, TiO_2 has thickness z, whereas the alpha–case layer has thickness x. The alpha–case layer has large oxygen solubility range starting with the highest oxygen concentration at the point Csl, i.e. the oxide/metal interface, and ending at distance Cso, where the oxygen content reaches the oxygen bulk concentration present in the base metal. In contrast, the solubility of oxygen in the oxide scale is limited and it can be considered to be linear. It can be seen that the oxygen concentration present in the metal gradually decreases. The oxygen concentration at the oxide/metal interface (Csl) is dependent on the exposure temperature and time and can reach a maximum value of 14.3 wt. %, which is the maximum solid solubility of oxygen in α - titanium.

The oxidation behavior of titanium alloys is more complex than that CP- Ti, mainly because of presence of β-phase, the influence of different alloying elements, as well as because of the coexistence of beta and alpha phases arrangement i.e. different microstructures. Although the reaction between titanium and oxygen at room temperature results in the formation of a thin and passive TiO_2 layer, at elevated temperatures, the TiO_2 layer loses its protectiveness and allows oxygen to be dissolved into the titanium bulk metal. The solubility of oxygen in α -titanium is about 30 at. % showing very small variations with temperature, whereas the solubility in β -titanium increases with temperature and at 1720 °C reaches maximum solubility about 8 at. %. Figure 2.11 shows the Ti–O phase diagram, from where it can be seen that many stable titanium oxides such as Ti_2O, TiO, $Ti2O_3$ and Ti_3O_5, TinO2n–1 (4 < n < 38) and TiO_2 can be formed. However, for oxidation at temperatures below 1000 °C and at near–atmospheric pressures only the Ti_2O rutile type modification has been detected in the oxide scales [75].

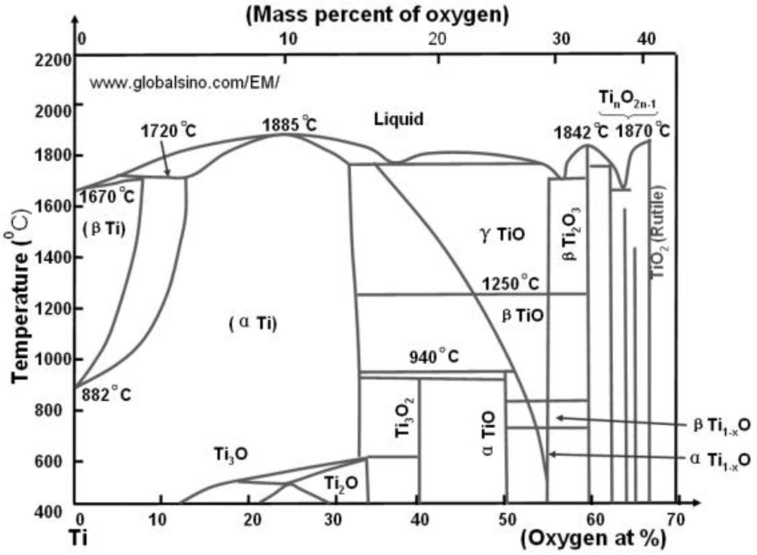

Figure 2.11 Ti-O phase diagram (Adpated from [76]).

2.4.4 Laser technology

Laser can be defined as a consistent and monochromatic light beam with high intensity and energy [77]. The generation of laser light is based on the principle of light amplification by stimulated emission of radiation (corresponding to abbreviation “LASER”). For producing the light beam, it is necessary that an external energy source (electrical, optical and chemical) bombards electrons into an active medium, which can be gaseous, liquid or solid. Thus, the electron excitation releases energy in the form of photons. These photons are reflected several times back in an optical cavity containing two mirrors at both extremities, in which one is totally reflector and the other is only partially reflector. Thus, when the gain positive is achieved, the amplified light with a specified wavelength leaves the system and the laser beam is generated [77,78].

Depending on the medium used to generate and amplify the light beam, laser can be classified as solid-state lasers (e.g. Nd:YAG, Nd:YVO_4, Ti-sapphire, fiber lasers), gas lasers (e.g. CO_2, excimer lasers, semiconductor lasers (e.g. InGaAs, AlGaInP) or as liquid dye lasers (e.g. organic liquid dyes) [77]. In some cases, lasers can operate in either continuous wave mode or pulsed mode (Figure 2.12). In the continuous wave lasers, such as CO_2 lasers, the main characteristic is the nonstop laser beam and hence a continuous output power. In contrast, the pulsed lasers, such as Nd:YAG lasers, operate by pulses, which can last from several hundreds of micro-seconds to femto-seconds

[79]. In the pulsed lasers, all the accumulated energy is released in a single pulse and the pulse duration is usually controlled by a Q-switch module that regulates the amount of stored energy inside the active medium during the laser blocking [77].

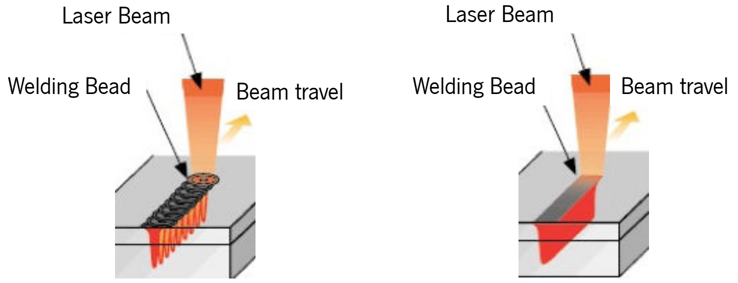

In the case of pulse irradiation

In the case of continuous irradiation

(a)

(b)

Figure 2.12 Schematic representation of the effects between the operation mode of a (a) pulsed laser and a (b) continuous wave laser. Adpted from http://www.avio.co.jp

2.4.4. Laser-matter interaction

The laser-matter interaction in the region near to the surface achieves extreme heating and cooling rates (10^3 - 10^{10} K/s), while the total deposited energy (typically, 0.1 - 10 J/cm^2) is insufficient to affect, significantly, the temperature of the bulk material. This allows this region to be processed in extreme conditions with little effect on the bulk properties [80].

One of the major advantages of the laser as a tool for material processing is the ability to control, precisely, wherein the material and at what rate energy is deposited. This control is possible through the proper selection of laser processing parameters to achieve the desired material modification. Moreover, material processing by laser technology is dependent on several process variables, which influence directly the laser-material interaction and at long last the processing efficiency and quality. To obtain the desired result there must be a good consensus between the material properties (optical and thermal properties), laser beam characteristics (power, wavelength, pulsed duration, etc.) and laser parameters (scanning speed, spot size, laser fluence, etc.).

Thus, as a versatile tool, laser can be applied for different purposes, such as in a subtractive method, which involve ablation mechanisms (i.e. material removal) and additive method, which, in turn, comprises sintering and fusion mechanisms in the material surface. The next subtopics will discuss briefly some aspects regarding the laser approaches performed in this work.

2.4.5. Laser surface modification (subtractive)

Surface properties modification over multiple length scales plays an important role in optimizing the material's performance for a given application. Multiscale surface modification is a critical factor in the development of new material structures and in engineering the detailed interactions which occur at surfaces and interfaces. Since the earliest works with pulsed lasers, it has been understood that the unique interaction of laser light with the material surface can lead to permanent changes in the material's properties not easily achieved by the other methods. Laser irradiation has been shown to induce changes to the local morphology, local chemistry and local structure, all of which affect the material's performance in a given application. Several review articles have been written regarding this subject [77,81–83]. The modification of the surface by laser has several advantages and some disadvantages. The main advantage is the ability to work with different types of materials with no significant setup modification. Laser can also be used to modify select areas of bulk material. The main disadvantage of laser is regarding the reproducibility when a new materials system is employed and the large setup cost for the instrumentation [84].

The modification of the surface by laser can be performed in several ways, such as laser drilling, laser cutting, laser turning, laser cladding, laser texturing and so on. The last one comprehends the heating of the surface, removing material through layer by layer ablation, giving rise periodic structures on the material surface, such as grooves, cavities and holes. Many works have reported laser surface modification in titanium alloy substrate for the most diverse applications, such as tribological [85], biomedical [86,87], fatigue behavior [88]. Recently, the interaction between lasers and Ti6Al4V titanium alloy has been widely investigated, with particular attention to superficial treatments such as texturing. For example, in [89] they studied the effect of various laser texturing strategies in the roughness, surface structure, hardness and water wettability of Ti6Al4V substrate for bonding adhesion. In [90] they examine the effects of Gaussian shaped beam profiles for nanosecond laser processing on the micro-groove characteristics created on Ti6Al4V substrate under different conditions. Laser parameters were also studied. The impact of laser processing parameters on Ti6Al4V samples were also investigated by Campanelli et al.[91]. In their study, the optimization of a nanosecond Nd:YAG laser parameters was performed, aiming to reduce geometrical defects and improving surface quality.

Although many works can be found in the literature on analyses of laser surface treatments of Ti6Al4V titanium alloy, works concerning a systematic study presenting the effects of main process laser parameters on the geometry of structures fabricated by laser ablation are still few.

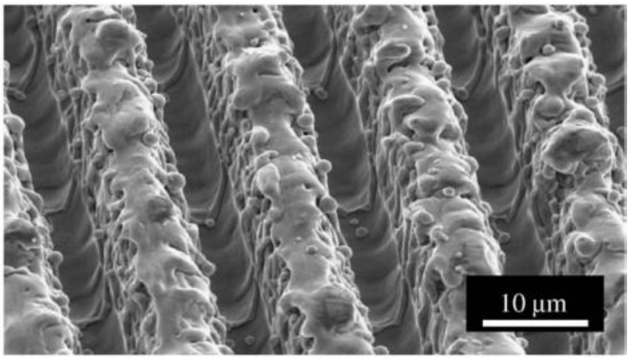

Figure 2.13 SEM image of Excimer laser-irradiated micro-grooves (adapted from [92])

When fluences below the threshold of melting are achieved in laser heating, a variety of temperature dependent process within the solid material can be activated. The high temperature gradients achieved with localized laser heating can lead to rapid self-quenching of the material, trapping in highly non-equilibrium structures. Moreover, the fast generation of high temperature gradients can induce thermal stresses, which in turn, can contribute to the mechanical response of the material, such as work hardening, cracking or warping [93].

At temperatures far above the melting temperature, hydrodynamic motion can reshape and redistribute the material. Radial temperature gradients on the order of 10^2-10^4 K/mm can develop in melt pools, causing convective flows to circulate material [77]. For most materials, the liquid's surface tension decreases with increasing temperature and the liquid is pulled from the hotter to the cooler regions (Marangoni effect) [94].

The mechanism of material removal is based on ablation or vaporization. This phenomenon occurs through the ejection of the material from the target surface due to absorption of a massive quantity of energy. Overall, during processing localized significant rise in temperature occurs near the target surface which results in material melting, vaporization and formation of a plume of hot ionized gas (plasma plume). However, depending on the laser power and the temporal working mode of the laser, specific ablation mechanism can take place. In femtosecond lasers, the removal of the material occurs mostly through non-thermal ablation process, involving the direct rupture of bonds between atoms, ions or molecules from the target [95,96]. Thus, since the temporal distribution of energy is extremely short, the thermal conduction into the bulk material can be despised and consequently only material vaporization is observed. The ultrashort pulse lasers provide great advantages in comparison to the long pulse lasers, such as precise ablation of materials, no microcrack formation and small heat affected zone [97–99]. Figure 2.14 shows the practical effects of long-pulsed and ultra-short pulse lasers on the machining process.

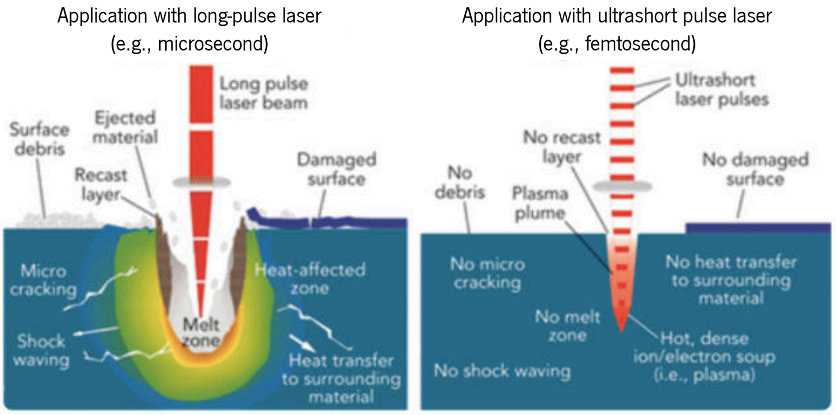

Figure 2.14 Schematic illustration of the comparison between the practical effects of a long-pulse laser and an ultrashort pulse laser. Taken from [98].

Although laser ablation is more discussed in the context of pulsed lasers, it is also possible with intense continuous wave mode irradiation. The onset of ablation occurs above the threshold fluence, which will depend on the absorption mechanism, particular material properties, microstructure, morphology, defects, and also on laser parameters, namely wavelength and pulse duration. According to literature, the typical threshold fluence for metals are between 1 and 10 J/cm^2, for insulators are between 0.5 and 2 J/cm^2, and for organic materials are between 0.1 and 1 J/cm^2 [82]. A detailed study regarding laser interaction with the matter and the phenomena involved is described in [100].

2.4.6. Laser sintering (additive)

The concept of laser sintering comes from the selective laser sintering/melting concept, which is a type of additive manufacturing (AM) process. The term “laser” in the name implies that the laser is used for processing and the term “sintering” implies that the powder is involved in the process. This implies that powder consolidation is done by laser to make products. The term “selective”, in turn, infers that all powder is processed by laser where and when it is required. “Melting” refers to a case in which the powder is completely melted. Although the name shows two processes (selective laser sintering - SLS and selective laser melting - SLM), for convenience they have been combined into one as “selective laser sintering/melting [101]. The main difference between the two processes is that, the first joins the powders by partial melting, while the latter by full melting. Four mechanisms are used to explain consolidation in SLS/SLM, namely (a) solid state sintering, (b) liquid phase sintering, (c) chemical-induced bonding and (d) full melting [102]. In the Solid State Sintering (SSS) the powders are bound by diffusion of atoms. The diffusion can be of type volume diffusion, surface diffusion or boundary diffusion. Thus, the diffusion gives rise to the neck formation at the boundary between two particles, which gets extended, fills the space with diffusion and binds the powders.

The Liquid Phase Sintering (LPS) is a mechanism widely used in SLS. When the interaction laser-materials take place, some of the powders are converted in liquid. Then, the liquid generated flows and fills the porous produced by the adjacent powder particles and thus, the powders are joined [102].

In the Chemical-Induced Binding (CIB) the binding of the powders is made by the chemical reactions which may occur when laser interacts with the material. For example, during the laser irradiation, the material can react with the environment gases (oxygen), forming composts with low melt point. These composts, which are melted, will bind the rest of the powders, giving rise to the consolidation. The chemical reactions can be exothermic and generate enough heat to subsequent consolidation.

Finally, in the full melting mechanism, the powders are fully melted, which on solidification gives rise to consolidation. As the powder bed is porous, the solidification gives rise to shrinkage. A high solidification rate can be responsible for stress residual generation. In this mechanism, for achieving the full melt of the powders, it is necessary for high laser power. Melting gives rise to liquid, which flows and wet the substrate and adjacent powder. The wetting will depend on the contact angle between solid/vapor, vapor/liquid and solid/liquid, as explained in [101].

As the interaction time between the laser and the material is short, a thermal gradient is generated. This leads to a convection motion inside the melt pool, which is called Marangoni effect [103]. The motion goes from the center of the melt pool to the periphery (i.e. from the high temperature region to the low temperature region), to minimize the thermal gradient. This gives rise to the spreading of the melt. In some cases, when there is a foreign element (for example, oxygen) in the melt pool, there is a decrease in the surface tension and the tension increases with an increase in temperature, thus, the direction of the motion is just opposite. Instead of creating the expansion of the pool, it causes the melt to congregate at the center line. Then, it causes a rise in the mass at the center, which is the reason for low surface quality [104].

Another problem regarding consolidation that is important to mention is related to the melt pool size. If the melt pool is longer, it will break in several small fragments [101]. There are many ways by which the formation of a long thin melt pool can be avoided, for instance using lower scan speed, higher spot size and preheating. The preheating decreases the solidification rate, which in turn induces the increase of the melt pool width and changes its proportion.

A single track process map was created by [105], as can be seen in Figure 2.12. The map is divided into five areas and each one represents the single-track shape for 314 stainless steel with different laser power and scanning speeds.

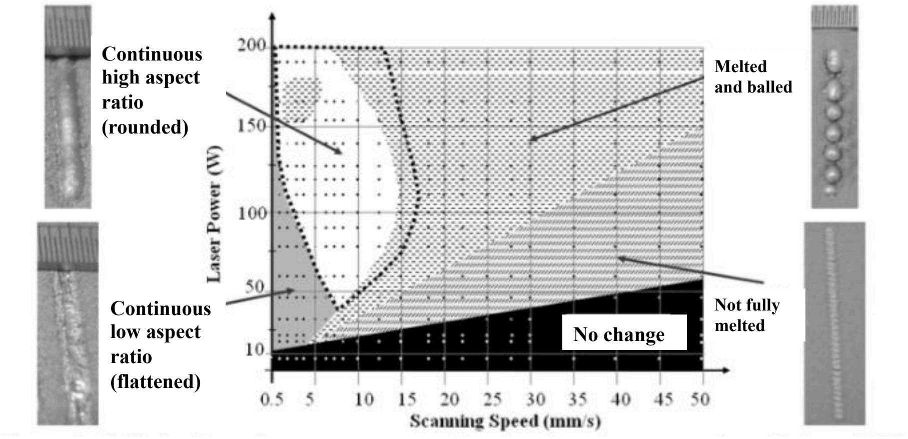

Figure 2.15 314S single track process map produced using a laser spot size of 1.1mm [105].

2.4.7. Laser oxidation

Heating of the titanium surface (along with other metals) in the air by laser source results in the growth of an oxide film due to the chemical interaction with the air components. The thin film properties are dependent on the temperature and heat time, while the application of pulsed laser radiation makes it possible to vary some characteristics of the film, namely compositions and thickness. Thus, it is therefore not surprising that oxidation of metals through laser processing is becoming attractive for applications requiring selectivity and high precision [106]. In particular, oxidation by laser can offer several advantages over the other methods, namely: high precision spatial-temporal control; less processing time for relatively small processing areas; high repeatability. Another important limitation of the other traditional methods to oxide titanium surface is that the majority of them are nonselective and the resulting oxide thickness is not totally controllable. Besides, high power and wet chemical bath are required, which make them hazardous processes [107]. The formation of a thin oxide film by laser can be achieved not only heating the metal surface but also by generating surface modification (which can involve the metal layer fusion) [107]. Notwithstanding, it is imperative a detailed characterization of the oxide layer properties produced by laser irradiation, such as chemical composition, thickness and morphology. Studies concerning the characterization of oxide layer in titanium surface have already been performed in literature, namely the composition and mechanism of laser oxidation [108], structures of Ti oxide films [106], laser oxidation versus anodizing [107] and the dependence of Ti oxide formation on laser parameters [109–111]. However, composition analysis is complicated since, during laser exposure in air, similar processing models can result in different compositions and thickness of the obtained films. Many divergences in results have been found in different authors regarding the determination of films' composition [108,112]. In the papers published to date, the authors have been reported oxide layers constituted mainly by TiO_2 [107] or a conglomeration of titanium oxides, namely Ti_2O, TiO, Ti_2O_3, TiO_2 [108,113]. In addition, abrupt temperature changes involved in laser oxidation can cause lasting structural defects, such as dislocations and microcracks, which may influence the diffusion of oxygen and change the reaction speed [113,114].

References

[1] C. O'Connor, A. Kiourti, Wireless Sensors for Smart Orthopedic Implants, J. Bio- Tribo-Corrosion. 3 (2017) 1–8. doi:10.1007/s40735-017-0078-z.

[2] B.S.M. Kurtz, K.L. Ong, J. Schmier, F. Mowat, K. Saleh, E. Dybvik, L.I. Havelin, O. Furnes, H. Malchau, E. Lau, U. States, N. Revision, Future Clinical and Economic Impact of Revision Total Hip and Knee Arthroplasty, 89 (2007) 144–151. doi:10.2106/JBJS.G.00587.

[3] M. Geetha, A.K. Singh, R. Asokamani, A.K. Gogia, Ti based biomaterials , the ultimate choice for orthopaedic implants – A review, Prog. Mater. Sci. 54 (2009) 397–425. doi:10.1016/j.pmatsci.2008.06.004.

[4] R.S. Park, J., & Lakes, Biomaterials: an introduction, Springer Science & Business Media, 2007.

[5] C. Ruff, B. Holt, E. Trinkaus, Perspectives Who ' s Afraid of the Big Bad Wolff ? : '" Wolff " s Law '' and Bone Functional Adaptation, 498 (2006) 484–498. doi:10.1002/ajpa.

[6] M. V Diamanti, M.P. Pedeferri, P. Milano, The Anodic Oxidation of Titanium and Its Alloys, 3 (2018) 41–54.

[7] C.L. and M. Peters, Titanium and titanium alloys: Fundamentals and applications, Wiley-

VCH, 2003.

[8] M.E.T. S. Bruschi, S. Poggio, F. Quadrini, Workability of Ti-6Al-4V alloy at high temperatures and strain rates, Mater. Lett. 58 (2004) 3622–3629. doi:10.1016/j.matlet.2004.06.058.

[9] I.D. J. Robert Kelly, Stabilized zirconia as a structural ceramic: An overview, Denatl Mater. J. 24 (2008) 289–298. doi:10.1016/j.dental.2007.05.005.

[10] R.T. Garvie, R. C., Hannink, R. H., & Pascoe, Ceramic steel?, Nature. 258 (1975) 703–704.

[11] B.R.R. T.K. Gupta, J.H. Bechtold, R.C. Kuznicki, L.H. Cadoff, Stabilization of tetragonal phase in polycrystalline zirconia, J. Mater. Sci. 12 (1977) 2421–2426.

[12] A. Eichler, Tetragonal Y-doped zirconia : Structure and ion conductivity, 64 (2001) 1–8. doi:10.1103/PhysRevB.64.174103.

[13] P. Ducheyne, Comprehensive biomaterials (Vol. 1)., Elsevier, 2015.

[14] T. Sato, Transformation of yttria partially stabilized zirconia by low temperature annealing in air, 20 (1985) 1466–1470.

[15] X. Guo, On the degradation of zirconia ceramics during low-temperature annealing in water or water vapor, 60 (1999) 539–546.

[16] J. Chevalier, What future for zirconia as a biomaterial?, Biomaterials. 27 (2006) 535–543. doi:10.1016/j.biomaterials.2005.07.034.

[17] W. Jin, P.K. Chu, H. Kong, Orthopedic Implants, (2017).

[18] N. Claussen, W.M. Kriven, M. Ruhle, Stability of Tetragonal Zr02 Particles in Ceramic Matrices, (n.d.) 642–650.

[19] E.H. Ledet, B. Liddle, K. Kradinova, S. Harper, Smart implants in orthopedic surgery , improving patient outcomes : a review, (2018) 41–51.

[20] A.-P. J., L. D.R., I. H.M.D., Y. G.-Z., From Wearable Sensors to Smart Implants-Toward Pervasive and Personalized Healthcare, IEEE Trans. Biomed. Eng. 62 (2015) 2750–2762. doi:10.1109/TBME.2015.2422751.

[21] F. Graichen, R. Arnold, A. Rohlmann, G. Bergmann, Implantable 9-Cavity Telemetry System for In Vivo Load Measurements With Orthopedic Implants, 54 (2007) 253–261.

[22] V.L. Roberts, Strain-gage Techniques in Biomechanics response of biological system to mechanical inputs, (n.d.) 19–22.

[23] G. Bergmann, Four-cavity measurement, J Biomed Eng. 13 (1991) 370–374.

[24] F. Burny, M. Donkerwolcke, F. Moulart, R. Bourgois, R. Puers, Concept , design and

fabrication of smart orthopedic implants, 22 (2001) 469–479.

[25] G. Bergmann, F. Graichen, Hip joint contact forces during stumbling, (2004) 53–59. doi:10.1007/s00423-003-0434-y.

[26] L.A. Ferrara, A.J. Fleischman, D. Togawa, T.W. Bauer, E.C. Benzel, S. Roy, An in vivo Biocompatibility Assessment of MEMS Materials for Spinal Fusion Monitoring, (2003) 297–302.

[27] R. Melik, N.K. Perkgoz, E. Unal, C. Puttlitz, H.V. Demir, Bio-implantable passive on-chip RF-MEMS strain sensing resonators for orthopaedic applications, J. Micromechanics Microengineering. 18 (2008) 115017. doi:10.1088/0960-1317/18/11/115017.

[28] P.J. Sell, Instrumented, J. Biomed. Eng. 11 (1989) 111–112.

[29] R.E. Newnham, ensors, Actuators, and Smart Materials, (1993) 27–33.

[30] R.K.S. Parul Gupta, Vineet Tirth, Structural Applications of Smart Materials in Construction Engineering Using Robotics, IEEE. (2006) 8–11.

[31] K.Y. Yazdandoost, Wireless Communications for Body Implanted Medical Device, (2007).

[32] A. Kiourti, K.A. Psathas, K.S. Nikita, Review Implantable and Ingestible Medical Devices WithWirelessTelemetry Functionalities : A Review of Current Status and Challenges, 15 (2014). doi:10.1002/bem.21813.

[33] A. Kiourti, K.S. Nikita, S. Member, A Review of In-Body Biotelemetry Devices :, 64 (2017) 1422–1430.

[34] M.M. Ahmadi, G.A. Jullien, L. Fellow, A Wireless-Implantable Microsystem for Continuous Blood Glucose Monitoring, 3 (2009) 169–180.

[35] A.K. Skrivervik, F. Merli, Design Strategies for Implantable Antennas, (2011) 1–5.

[36] R.F. Harrington, Effect of Antenna Size on Gain , Bandwidth , and EfficiencyI, 64 (1960).

[37] P. Soontornpipit, C.M. Furse, Y.C. Chung, Design of Implantable Microstrip Antenna for Communication With Medical Implants, 52 (2004) 1944–1951.

[38] Asimina Kiourti and Konstantina S. Nikita, A Review of Implantable Patch Antennas for Biomedical Telemetry : Challenges and Solutions, IEEE Antennas Propag. Mag. 54 (2012) 210–228.

[39] J. Abadia, F. Merli, 3D-Spiral Small Antenna Design and Realization for Biomedical Telemetry in the MICS band, 18 (2009) 359–367.

[40] C. R. Hammond, The elements, 2000.

[41] A. Reti, Silver: Alloying, Properties, and Applications $, (2016) 1–7. doi:10.1016/B978-0-

12-803581-8.02583-2.

[42] N.P. M.V.Róldan, A. Frattini, O. de Sanctis, H. Troiani, Characterization and applications of Ag nanoparticles in waveguides, Appl. Surf. Sci. 254 (2007) 281–285. doi:10.1016/j.apsusc.2007.07.059.

[43] F. Wang, N. Nie, H. He, Z. Tang, Z. Chen, W. Zhu, Ultrasonic-Assisted Sintering of Silver Nanoparticles for Flexible Electronics, (2017). doi:10.1021/acs.jpcc.7b09581.

[44] H. Zhang, G. Zou, L. Liu, A. Wu, Y.N. Zhou, paste for electronic packaging, (n.d.) 314–317.

[45] V. Lazar, Anaerobe Quorum sensing in bio fi lms e How to destroy the bacterial citadels or their cohesion / power ?, 17 (2011) 280–285. doi:10.1016/j.anaerobe.2011.03.023.

[46] R.M. Donlan, J.W. Costerton, Biofilms : Survival Mechanisms of Clinically Relevant Microorganisms, 15 (2002) 167–193. doi:10.1128/CMR.15.2.167.

[47] M.A. Biel, C. Sievert, M. Usacheva, M. Teichert, J. Balcom, sinusitis biofilms, 1 (2011) 329–334. doi:10.1002/alr.20089.

[48] H. Dargo, A. Ayaliew, H. Kassa, Synthesis paradigm and applications of silver nanoparticles (AgNPs), a review, 13 (2017) 18–23.

[49] N.R. Panyala, E.M. Peña-méndez, J. Havel, Silver or silver nanoparticles : a hazardous threat to the environment and human health ?, (2008) 117–129.

[50] G. Franci, A. Falanga, S. Galdiero, L. Palomba, M. Rai, G. Morelli, M. Galdiero, Silver Nanoparticles as Potential Antibacterial Agents, (2015) 8856–8874. doi:10.3390/molecules20058856.

[51] G. Nam, B. Purushothaman, S. Rangasamy, Investigating the versatility of multifunctional silver nanoparticles : preparation and inspection of their potential as wound treatment agents, (2016) 51–63. doi:10.1007/s40089-015-0168-1.

[52] C. Greulich, S. Kittler, M. Epple, G. Muhr, M. Köller, Studies on the biocompatibility and the interaction of silver nanoparticles with human mesenchymal stem cells (hMSCs), (2009) 495–502. doi:10.1007/s00423-009-0472-1.

[53] L. Zhao, H. Wang, K. Huo, L. Cui, W. Zhang, H. Ni, Y. Zhang, Z. Wu, P.K. Chu, Biomaterials Antibacterial nano-structured titania coating incorporated with silver nanoparticles, 32 (2011) 5706–5716. doi:10.1016/j.biomaterials.2011.04.040.

[54] V. Alt, T. Bechert, P. Steinr, M. Wagener, P. Seidel, E. Dingeldein, E. Domann, R. Schnettler, An in vitro assessment of the antibacterial properties and cytotoxicity of nanoparticulate silver bone cement, 25 (2004) 4383–4391. doi:10.1016/j.biomaterials.2003.10.078.

[55] A.F. Padilha, Materiais de Engenharia-Microestrutura e Propriedades, Hemus, 2007.

[56] and D.G.R. Callister, William D., Materials science and engineering: an introduction., John Wiley & Sons, Inc., New York, N.Y, 2007.

[57] Z.H.K. and A.P. H. KIm, G. P. Kushto, C. B. Arnold, Laser processing of nanocrystalline for dye-sensitized solar cells, Appl. Phys. Lett. 85 (2004) 1–4. doi:10.1063/1.1772870.

[58] Y. Matsumoto, Y. Matsumoto, M. Murakami, T. Shono, Room-Temperature Ferromagnetism in Transparent Transition Metal – Doped Titanium Dioxide, 854 (2014). doi:10.1126/science.1056186.

[59] E.-K.S. B. Karunagaran, Periyayya Uthirakumar, S.J. Chung, S. Velumani, TiO2 thin film gas sensor for monitoring ammonia, Mater. Charact. 58 (2007) 680–684. doi:10.1016/j.matchar.2006.11.007.

[60] Y. Ju, M. Wang, Y. Wang, S. Wang, C. Fu, Electrical Properties of Amorphous Titanium Oxide Thin Films for Bolometric Application, 2013 (2013).

[61] D.M. A. Yildiz, S.B. Lisesivdin, M. Kasap, Electrical properties of TiO2, J. Non. Cryst. Solids. (2008) 5–9. doi:10.1016/j.

[62] D.A.H. Hanaor, C.C. Sorrell, Review of the anatase to rutile phase transformation, (2011) 855–874. doi:10.1007/s10853-010-5113-0.

[63] S.A. Campbell, H.-S. Kim, D.C. Gilmer, B. He, T. Ma, W.L. Gladfelter, Titanium dioxide (TiO 2)-based gate insulators, IBM J. Res. Dev. 43 (1999) 383–392. doi:10.1147/rd.433.0383.

[64] S.D. Sharma, D. Singh, K.K. Saini, C. Kant, V. Sharma, S.C. Jain, C.P. Sharma, Sol-gel-derived super-hydrophilic nickel doped TiO2 film as active photo-catalyst, Appl. Catal. A Gen. 314 (2006) 40–46. doi:10.1016/j.apcata.2006.07.029.

[65] N. Smirnova, A. Eremenko, V. Gayvoronskij, I. Petrik, Y. Gnatyuk, G. Krylova, A. Korchev, A. Chuiko, Sol-gel processed functional nanosized TiO 2 and SiO 2-based films for photocatalysts and other applications, J. Sol-Gel Sci. Technol. 32 (2004) 357–362. doi:10.1007/s10971-004-5817-1.

[66] M. Hirano, C. Nakahara, K. Ota, O. Tanaike, M. Inagaki, Photoactivity and phase stability of ZrO2-doped anatase-type TiO2 directly formed as nanometer-sized particles by hydrolysis under hydrothermal conditions, J. Solid State Chem. 170 (2003) 39–47. doi:10.1016/S0022-4596(02)00013-0.

[67] H. Dia, Sol-Hydrothermal Synthesis and Hydrothermally Structural Evolution of Nanocrystal Titanium Dioxide, (2002) 1974–1980.

[68] A. Mills, N. Elliott, I.P. Parkin, S.A. O'Neill, R.J. Clark, Novel TiO2 CVD films for semiconductor photocatalysis, J. Photochem. Photobiol. A Chem. 151 (2002) 171–179. doi:10.1016/S1010-6030(02)00190-9.

[69] S. Meyer, R. Gorges, G. Kreisel, Preparation and characterisation of titanium dioxide films for catalytic applications generated by anodic spark deposition, Thin Solid Films. 450 (2004) 276–281. doi:10.1016/j.tsf.2003.11.168.

[70] Alan Matthews, The crystallization of anatase and rutile from amorphous titanium dioxide under hydrothermal conditions, Am. Mineral. 61 (1976) 419–424.

[71] T.B. Ghosh, S. Dhabal, A.K. Datta, On crystallite size dependence of phase stability of nanocrystalline TiO 2 On crystallite size dependence of phase stability of nanocrystalline TiO 2, 4577 (2013). doi:10.1063/1.1604966.

[72] P. Kofstad, High temperature oxidation of metals, New York, N.Y, 1966.

[73] A. Fromhold, Theory of Metal Oxidation, Amsterdam, 1976.

[74] W.J. C. Wagner, Diffusion in solids, liquids, gases, Academic P, New York, N.Y, n.d.

[75] P. Kofstad, High temperature corrosion, in: C.H. Elsevier Applied Science Publishers (Ed.), Linton Road, Barking, Essex IG 11 8 JU, UK, 1988.

[76] H. Okamoto, O-Ti (Oxygen-Titanium), J. Phase Equilibria. 22 (2011) 515–515.

[77] J. C. Ion, Laser processing of engineering materials principles, procedure and industrial application, Elsevier Butterworth-Heinemann, 2005.

[78] R. Paschotta, Lasers, RP Photonics Encycl. (n.d.).

[79] G. Plohl, Pulsed Laser Ablation, 2012.

[80] J.D. Majumdar, Laser processing of materials, (2014). doi:10.1007/BF02706446.

[81] N. Dahotre, Lasers in surface engineering, in: Surf. Eng. Ser., ASM International, OH, USA, 1998.

[82] D. Bauerle, Laser processing and chemistry, Springer, 2000.

[83] W.M. Steen, Laser material processing, Springer, 2003.

[84] V.K. Balla, J. Soderlind, S. Bose, A. Bandyopadhyay, Microstructure, mechanical and wear properties of laser surface melted Ti6Al4V alloy, J. Mech. Behav. Biomed. Mater. 32 (2014) 335–344. doi:10.1016/j.jmbbm.2013.12.001.

[85] C. Gachot, A. Rosenkranz, S.M. Hsu, H.L. Costa, A critical assessment of surface texturing for friction and wear improvement, Wear. 372–373 (2017) 21–41. doi:10.1016/j.wear.2016.11.020.

[86] A. Cunha, A.M. Elie, L. Plawinski, A.P. Serro, A.M. Botelho Do Rego, A. Almeida, M.C. Urdaci, M.C. Durrieu, R. Vilar, Femtosecond laser surface texturing of titanium as a method to reduce the adhesion of Staphylococcus aureus and biofilm formation, Appl. Surf. Sci. 360 (2016) 485–493. doi:10.1016/j.apsusc.2015.10.102.

[87] O. Raimbault, S. Benayoun, K. Anselme, C. Mauclair, T. Bourgade, A.M. Kietzig, P.L. Girard-Lauriault, S. Valette, C. Donnet, The effects of femtosecond laser-textured Ti-6Al-4V on wettability and cell response, Mater. Sci. Eng. C. 69 (2016) 311–320. doi:10.1016/j.msec.2016.06.072.

[88] A.J. Sterling, B. Torries, N. Shamsaei, S.M. Thompson, D.W. Seely, Fatigue behavior and failure mechanisms of direct laser deposited Ti-6Al-4V, Mater. Sci. Eng. A. 655 (2016) 100–112. doi:10.1016/j.msea.2015.12.026.

[89] I.A. Milton Sérgio Fernandes Lima, Surface Modification of Ti6Al4V Alloy by Pulsed Lasers : Microstructure and Hydrophobic, Mater. Res. 20 (2017) 8–14.

[90] A.Y. Fasasi, S. Mwenifumbo, N. Rahbar, J. Chen, M. Li, A.C. Beye, C.B. Arnold, W.O. Soboyejo, Nano-second UV laser processed micro-grooves on Ti6Al4V for biomedical applications, Mater. Sci. Eng. C. 29 (2009) 5–13. doi:10.1016/j.msec.2008.05.002.

[91] S.L. Campanelli, F. Lavecchia, N. Contuzzi, G. Percoco, Analysis of shape geometry and roughness of Ti6Al4V parts fabricated by nanosecond laser ablation, Micromachines. 9 (2018). doi:10.3390/mi9070324.

[92] John L. Ricci and Harold Alexander, Laser microtexturing of implant surfaces for enhaced tissue integration, Trans Tech Publ. 199 (2001) 179–202. doi:10.4028/www.scientific.net/KEM.198-199.179.

[93] M.S. Brown, C.B. Arnold, Fundamentals of Laser-Material Interaction and Application to Multiscale Surface Modification, (n.d.) 91–120. doi:10.1007/978-3-642-10523-4.

[94] T.D. Bennett, D.J. Krajnovich, C.P. Grigoropoulos, P. Baumgart, A.C. Tam, Marangoni Mechanism in Pulsed Laser Texturing of Magnetic Disk Substrates, J. Heat Transfer. 119 (1997) 589. doi:10.1115/1.2824146.

[95] D. Baeuerle, Laser Processing and Chemistry, Springer, Heidelberg Berlin 13, 2000.

[96] J. D. Majumdar and I. Manna, Laser-Assisted Fabrication of Materials, vol. 161, Berlin, Heidelberg, 2013.

[97] N. Dahotre, A. Samant, Laser machining of advanced materials, 2011. doi:10.1201/b10862-3.

[98] S.H. and G. Shannon, Precision machining with no thermal effects and minimal post processing," Femtosecond laser processing of metal and plastics in the medical device industry, (2014). http://www.industrial-lasers.com/articles/print/volume-29/issue-5/features/femtosecond-laser-processing-of-metal-and-plastics-in-the-medical-device-industry.html (accessed September 2, 2019).

[99] K.M. Tanvir Ahmmed, C. Grambow, A.M. Kietzig, Fabrication of micro/nano structures on metals by femtosecond laser micromachining, Micromachines. 5 (2014) 1219–1253. doi:10.3390/mi5041219.

[100] A. Soveja, J. Jouvard, Metal surface laser texturing: multiphysics modelling of a single impact effect, Excerpt from Proc. (2007) 1–6. http://cds.comsol.com/access/dl/papers/2727/Soveja.pdf.

[101] S. Kumar, Selective Laser Sintering / Melting, 2014.

[102] T.H.C.C. J.-P. Kruth, G. Levy, F. Klocke, Consolidation phenomena in laser and powder-bed based layered manufacturing, Ann. CIRP. 56 (2007).

[103] T.D. Bennett, D.J. Krajnovich, Marangoni Mechanism in Pulsed Laser Texturing of Magnetic Disk Substrates, 1 (2016).

[104] M. Rombouts, L. Froyen, P. Mercelis, K.U. Leuven, K.U. Leuven, Fundamentals of Selective Laser Melting of alloyed steel powders, 1 (2006) 4–9.

[105] M.B. T.H.C. Childs, C. Hauser, Mapping and modeling single scan track formation in direct metal selective laser melting, 8506 (n.d.) 7–11. doi:10.1016/S0007-8506(07)60676-3.

[106] J.L.M. Gyorgy, E., A. Perez del Pino, P. Serra, Structure formation on titanium during oxidation induced by cumulative pulsed Nd : YAG laser irradiation, Appl. Phys. A Mater. Sci. Process. 78 (2004) 765–770. doi:10.1007/s00339-002-2054-8.

[107] A. Pérez del Pino, J.M. Fernández-Pradas, P. Serra, J.L. Morenza, Coloring of titanium through laser oxidation: Comparative study with anodizing, Surf. Coatings Technol. 187 (2004) 106–112. doi:10.1016/j.surfcoat.2004.02.001.

[108] A. Pérez Del Pino, P. Serra, J.L. Morenza, Oxidation of titanium through Nd:YAG laser irradiation, Appl. Surf. Sci. 197–198 (2002) 887–890. doi:10.1016/S0169-4332(02)00447-6.

[109] A.J.A.· B.S.· P.E.K.· K.M. Abramski, the influence of process parameters on the laser-induced coloring of titanium, Appl. Phys. A Mater. Sci. Process. 115 (2014).

[110] A.A.W. L. Skowronski, A.J. Antónczak, M. Trzcinski, L. Lazarek, T. Hiller, A. Bukaluk, Optical

properties of laser induced oxynitride films on titanium, Appl. Surf. Sci. 304 (2014) 107–114.

[111] B.H.J. D.P. Adams, R.D. Murphy, D.J. Saiz, D.A. Hirschfeld, M.A. Rodriguez, P.G. Kotula, Nanosecond pulsed laser irradiation of titanium: oxide growth and effects on underlying metal, Surf. Coatings Technol. 248 (2014) 38–45.

[112] L. Lavisse, M.C. Sahour, J.M. Jouvard, G. Pillon, M.C.M. De Lucas, S. Bourgeois, D. Grevey, Applied Surface Science Growth of titanium oxynitride layers by short pulsed Nd : YAG laser treatment of Ti plates : Influence of the cumulated laser fluence, 255 (2009) 5515–5518. doi:10.1016/j.apsusc.2008.07.197.

[113] D.P. Adams, R.D. Murphy, D. Saiz, M. Rodriguez, D. Hirschfeld, Nanosecond Pulsed Laser Color Marking of Titanium : Analysis of Oxide Layer Phase, (2013) 6–7.

[114] S. O'Hana, A.J. Pinkerton, K. Shoba, A.W. Gale, L. Li, Laser surface colouring of titanium for contemporary jewellery, Surf. Eng. 24 (2008) 147–153. doi:10.1179/174329408X315607.

Chapter 3 - Laser surface texturing of Ti-6Al-4V by nanosecond laser: Surface characterization, Ti-oxide layer analysis and its electrical insulation performance

Published in Journal of Materials Science & Engineering C, 2019, 104: 109901

C. G. Moura[1]*, O. Carvalho[1], L.M.V. Gonçalves[1], M. F. Cerqueira[2,3], R. Nascimento[4], F. Silva[1]

[1]CMEMS-UMinho, University of Minho, 4800-058, Guimarães, Portugal
[2]Centro de Física, University of Minho, 4710-057, Braga, Portugal
[3]International Iberian Nanotechnology Laboratory (INL), 4715 Braga, Portugal
[4]Materials Science and Engineering Post-Graduate Program, UFRN, 59078-970 Natal, Brazil

*Corresponding author – C. G. Moura (caroline.materiais@gmail.com)

Abstract

The development of smart biomedical implants with intrinsic communication system between sensors and actuators, or between implant and patient, remains a challenge for scientific community. Titanium and its alloys, especially Ti6Al4V, are the most used materials in the implant's fabrication. The present work is concerned with implant internal communication printing process and presents a detailed study on titanium alloy (Ti6Al4V) surface texturing and their characterization (morphological and chemical) produced by a Nd: YAG laser, aiming to create localized electrical insulation zones, necessary to accommodate electrical communication systems. The characterization of the textured surface was carried out by scanning electron microscopy and the heat affected zone was analyzed by X-ray diffraction. The results showed the formation of α-Ti, Ti_6O and Ti_2O phases on the textured surface. Through simulations in *TINA* software, the outer oxide layer formed during laser texturing had efficiency above 90% as insulator when an electrical current was applied.

Keywords:

3.1 Introduction

Smart implants are implantable devices that not only provide therapeutic benefits but also diagnostic capability [1]. The technological advances in this area are related to the possibility of developing intelligent implants, capable of providing the patient real-time feedback on the performance of the implants, thus allowing the identification of possible problems such as inflammations, or other abnormal body reactions. Although the development of smart implants to integrate additional functions to implants, including sensing functions, power transfer functions, energy storage functions, and an internal communication system, has matured over the last decades, there are still many challenges to be overcome. This is particularly important if we consider that the additional functions should be fully integrated within the implant or in its surface, during manufacturing, mainly through additive technologies, and not assembled as a post processing. The pairing of these additional functions on the implant, such as diagnostics and treatment, with self-storage capable to provide energy to activate sensors and actuators on the implants surface, as well as communication between sensorized/actuating areas, and from implant to patient, may be the key to enable the long-term success of the implants.

As biomedical material, titanium and its alloys, especially Ti6Al4V, are the most used due to its excellent biocompatibility, high corrosion resistance and high strength [2,3]. Due to the fact that Ti6Al4V is a bioinert material, it has been the subject of several studies [4–8], which reveals big improvements of properties upon surface modification. Several techniques can be used to perform the surface modification of titanium-based materials [9]. Among them, laser surface texturing (LST) has demonstrated to be a promising alternative to overcome the conventional existent methods, since it is versatile and environmentally friendly. Laser, as a direct energy source, can enable deposition, removal and alteration of material property through changes in its configuration. The mainly advantage of using laser as an energy source is due to its efficient control of depth and amount of energy. This technique is desirable for microtechnology due to its high lateral resolution, low heat input and high flexibility [10,11]. For these laser approach has been extremally explored by several works, for instance in texturing field [7,12–14]. In this method a high energy density is applied on the surface, by using the laser, allowing material ablation which result in surface roughness with preferred orientations, meaning different structures on the surface [15]. Furthermore, laser surface texturing has proven to be efficient not only to produce periodic surface structures but also to oxidize metal surfaces, which results in formation of a coating film through anodic oxidation. Thus, this approach allows to combine a groove formation with surface oxidation at the same time, since the oxide layer grows on the sample surface as a result of the gases mixture and oxygen diffusion existent in the atmospheric environment [16].

Studies concerning laser surface texturing on titanium alloys, namely the analysis of the heat affected zone due to the Ti oxide layer formation are very scarce. Furthermore, in literature the studies are more focused on the investigation of the crystalline structures and optical properties of TiO_2 [17,18], very few have been concerned the electrical properties of TiO_2 thin film [19,20]. However, the electrical characterization of the formed oxide layer becomes crucial if we aim to create electrical barriers (cavities) between electrical conductors for electronic circuit printed on Ti6Al4V (either on implant's surface or inside the component, during additive printing), which is the idea behind the concept of smart implants. Figure 3.1 shows a schematic representation of this potential application, which will be described in more detail in this work.

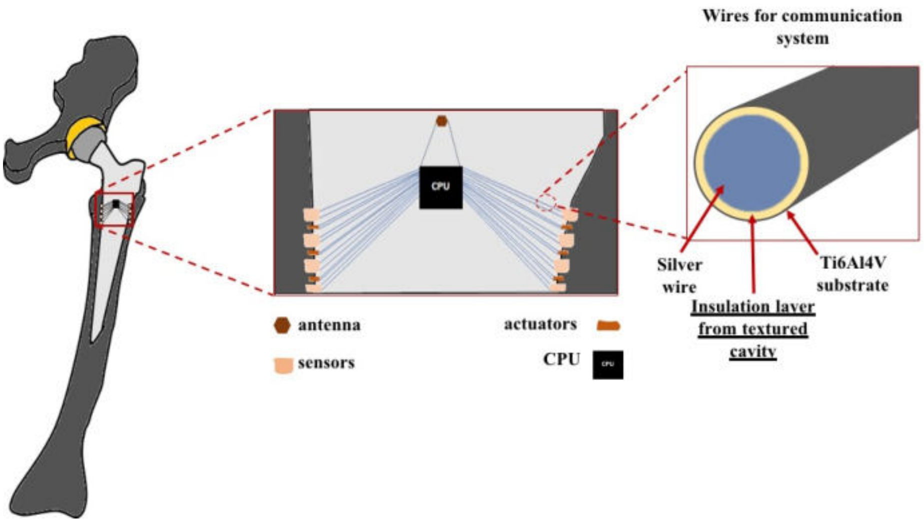

Figure 3.1 Schematic representation of electronic circuit printed on Ti6Al4V substrate.

Figure 3.1 presents the concept of a smart hip implant where actuating and sensoring areas are printed in the surface, and an internal electrical communication system is printed between them and a CPU-central processing unit. The whole system may be printed in the component surface, or, preferably inside the component, by using smart additive technologies, as the one being developed in the CMEMS research centre [21], where the component and the communication, sensoring and actuating areas, are printed sequentially, being thus fully integrated in the implant. In this sense, this work presents a detailed study on titanium alloy (Ti6Al4V) grooves manufacturing and their electrical insulation, for posterior communication systems printing (for example in Silver), and their morphological and chemical characterization. A Nd:YAG laser was used to produce both the grooves and the thermo-chemical oxidation treatment for their electrical insulation. Cavities with different depths and surface topology have been produced, in order to determine the most adequate strategy to produce cavities in Ti6Al4V surface. Due to the high flexibility of the laser system, structural features such as topology, morphology and depth can be achieved by changing the laser parameters. An optimization of the parameters, namely scanning speed, laser power and number of passes, were performed aiming to obtain less amount of defects and better surface groove quality. The structural and electronic properties of Ti oxides thin-layers resulting from laser surface texturing were studied and discussed. The electrical insulation property of Ti-oxide/Ti6Al4V interface was analyzed based on current-voltage measurements in a metal conductor structure and its insulator capacity was simulated through *TINA* simulation software.

3.2 Experimental details

3.2.1 Surface laser texturing

A Nd:YAG laser (OEM Plus, working in wavelength of 1064 nm and 6 W of maximum power) was used to texture grooves in the surface of a 2 mm thick Ti6Al4V titanium alloy target. Figure 3.2 shows a scheme illustrating the used experimental set up (Fig 3.2b). The laser is pulsed and the laser spot has a diameter of 3 μm, then each laser textured line consists in a sequence of several pulses with an overlap area (Figure 3.2a). For texturing the grooves, the distance between each line was changed from 10 to 50 μm in order to study the effect on the groove quality (Fig 3.2c). Table 1 shows the combination of parameters used in this work. Figure 3.2d) shows a photo of a real sample after laser processing.

As can be seen in Figure 3.2b, we have different groups of cavities represented by grey and black rectangles. In each rectangle there are five groups of lines with different distance between them, which will result in five different cavities after laser scanning. The grooves were designed by using a drawing software mask and the width of the cavities was projected to have 250 μm. Using these masks, the sample laser scanning was approached. Three laser scanning parameters were varied in this study, namely laser power, scanning speed and number of passes, in order to evaluate i) their influence on the quality of the grooves, ii) the amount of material re-solidified and iii) the depth achieved. Laser power represents the laser beam energy delivered per pulse in Watts; the scanning speed is the marking speed at the leading edge of the beam front in mm/s and the number of passes corresponds to the number of scans carried out by the laser during the process, which will affect the depth of groove.

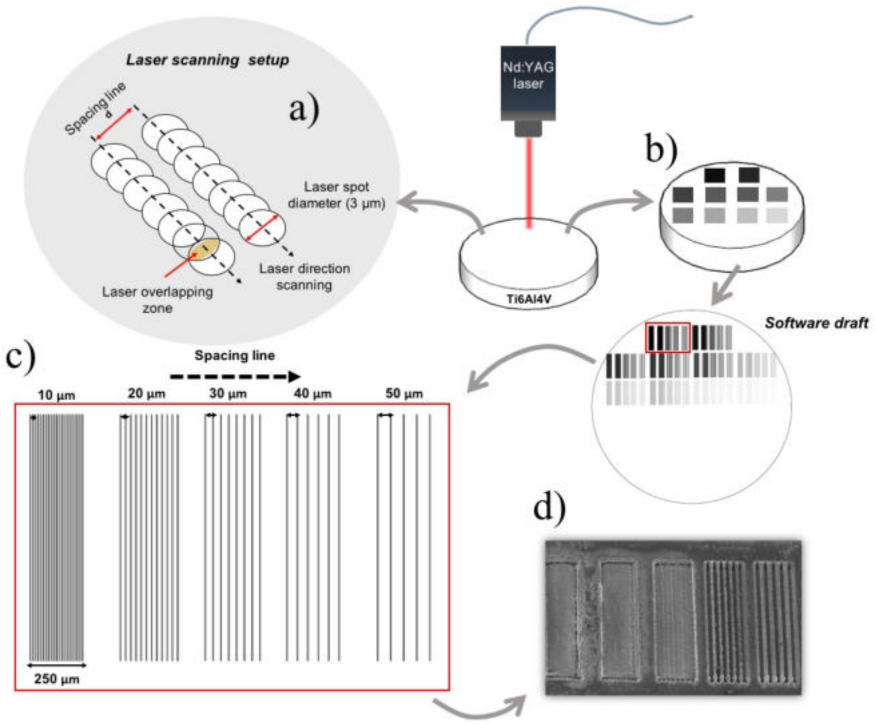

Figure 3.2 Scheme illustrating the experimental set-up of the laser processing (a and b). It is also shown a Scheme illustrating the different kinds of grooves performed (b) and (d) is a photo of a real sample after processing.

Table 3.1.Laser parameters combination

Laser power (W)	Scanning speed (mm/s)			
	64	128	256	400
6	● ▲ ✖	● ▲ ✖	● ▲ ✖	● ▲ ✖
3	● ▲ ✖	● ▲ ✖	● ▲ ✖	● ▲ ✖
1.5	● ▲ ✖	● ▲ ✖	● ▲ ✖	● ▲ ✖

Number of passes:

● 1 pass ▲ 4 passes ✖ 16 passes

The laser energy density (E) was calculated for each condition through the equation below:

$$E = \frac{P \times n}{v}$$ *Equation 1*

Where P is the laser power (Watts), *E* is energy density in J/mm; *n* is the number of passes and *v* is the scanning speed in mm/s.

3.2.2 Surface characterization

The surface morphology of irradiated samples was analyzed by scanning electron microscopy (SEM). The phase composition of the titanium oxide layer was analyzed by X-ray diffraction (XRD-Bruker D8 Discover) using a CuKα radiation at a grazing angle of 1°.

3.2.3 Insulation properties of Ti-oxide layer

After the parameters' study for a good quality groove formation and corresponding characterization of the Ti-oxide obtained layer, we devote our study to analyze the insulation property of the Ti-oxide layer formed during laser texturing on the surface. For this study the following methodology was used.

A Ti6Al4V sample was irradiated using the optimal laser parameters creating a desired groove. Then, Ag powder (average size particle of 230 nm) was compacted inside the created groove and exposed again to the laser (Nd:YAG, laser fluence of 5.6 x 10^3 J/mm^2), in order to form an Ag wire (diameter around 250 μm), as illustrated in Figure 3.3a). The resistance of each component of the final structure, namely the resistance of oxide layer (R_o), resistance of the wire (R_w) and the resistance of the substrate-Ti alloy (R_s) was measured by using four-point probe method, using different configurations (Fig 3.3b). In this method a current is passed through the outer probes and induces a voltage in the inner voltage probes. For this, in configuration 1, the current was applied to the wire and the voltage was also measured on it, thus the resistance of the wire was obtained. In configuration 2, the current was applied to the substrate and the voltage was measured on the wire, allowing to obtain the resistance of the oxide layer. Finally, in configuration 3, the current was applied to the substrate and the voltage was also measured on it, the resistance of the substrate was achieved. After obtaining the resistances, an electrical circuit was built and simulated through the *TINA* software and a current of 100mA was applied. In Figure 3.3c) this methodology is outlined. This circuit models the interface between the substrate and the wire. The series resistances R1 and R2 represents the measured wire resistance (R_W), the series resistances R3 and R4 the substrate resistance (R_S) and parallel of R6 resistors the measured interface resistance (R_{OL}).

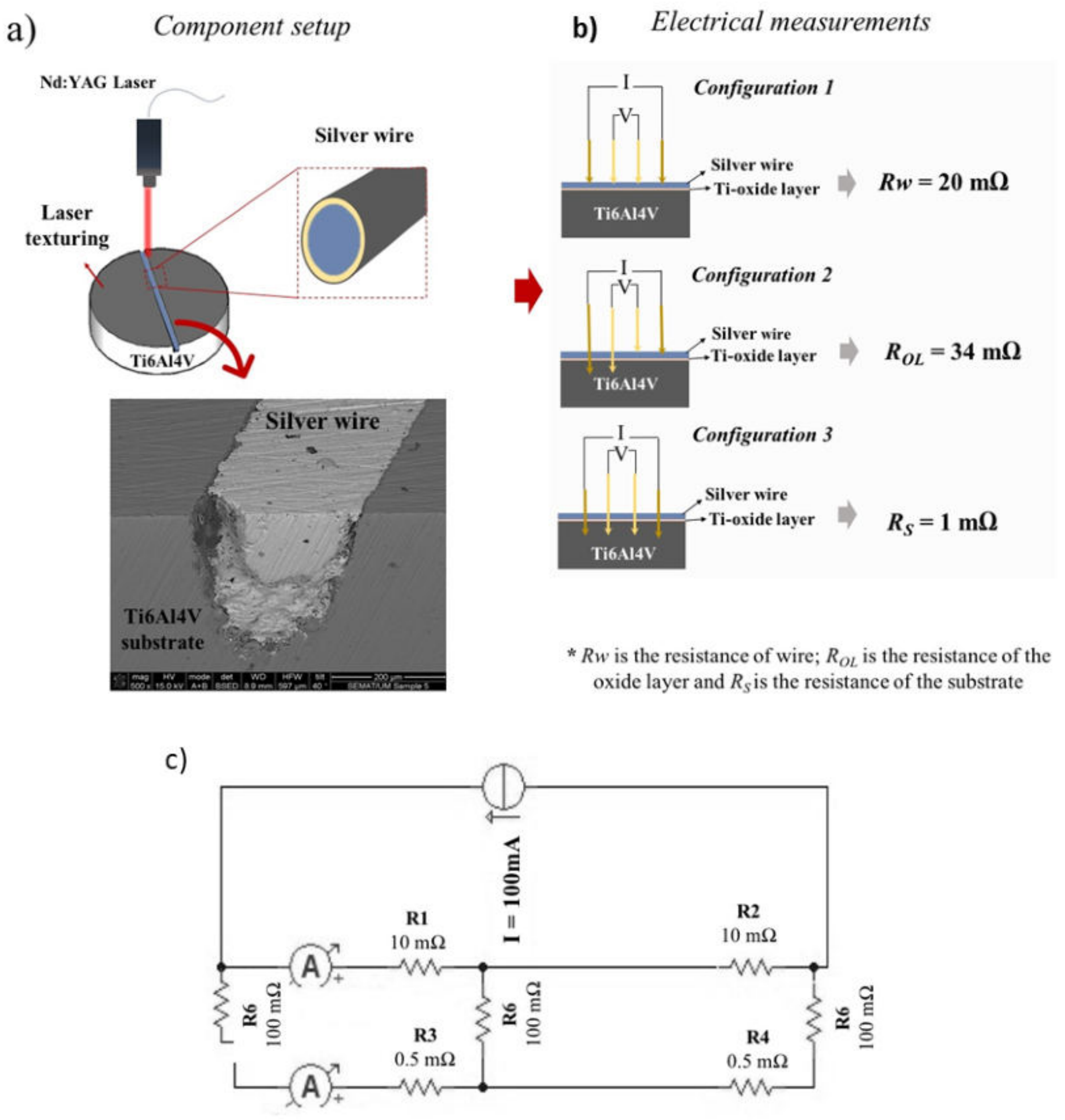

* Rw is the resistance of wire; R_{OL} is the resistance of the oxide layer and R_S is the resistance of the substrate

R1 and **R2** correspond to R_W (resistance of the wire), **R3** and **R4** correspond to R_S (resistance of the substrate) and **R6** corresponds to R_{OL} resistance of the oxide layer.

Figure 3.3.Illustration of the process for the Ag wire formation. (a) The SEM image illustrates the Silver wire inside the groove (scale bar=200 µm). (b) Experimental methodology used for electrical measurements. (c) Electrical circuit built through TINA software.

3.3 Results and discussion

3.3.1 Surface morphology of the laser grooves

Figure 3.4 (a-c) shows the SEM micrographs of the laser textured surface of Ti-6Al-4V processed in air, in which (a) n=1, (b) n=4 and (c) n=16 refer to the number of laser passes. Figure 3.4(a) reveals the results of the parameters map tested, compound by 5 grooves (for each condition), with widths around 250 µm, wherein each one was built by periodic lines spaced with different values: from 10 to 50 µm - as can be seen in Figure 3.2. For some of the combinations of the used parameters, the application of equation 1, results in the same value of energy density. However, analyzing the SEM images in Fig 3.4 it is seen that each parameters combination result in different surface changes (even if the energy density is the same), which means that each parameter has an important role on the surface modification, as seen in Figure 3.4. The contour plots of laser energy density (E) for the studied numbers of passes (n) is demonstrated in the plot shown in Figure 3.5. These contour plots are directly associated with the matrix of conditions that make up each group (the latter being defined by the different number of passes used) and represents the energy density (using Equation 1) distribution in each group, as a function of the different values of laser power and scan speed. In Figure 3.4 the conditions corresponding to the highest laser energy are highlighted in red color contour.

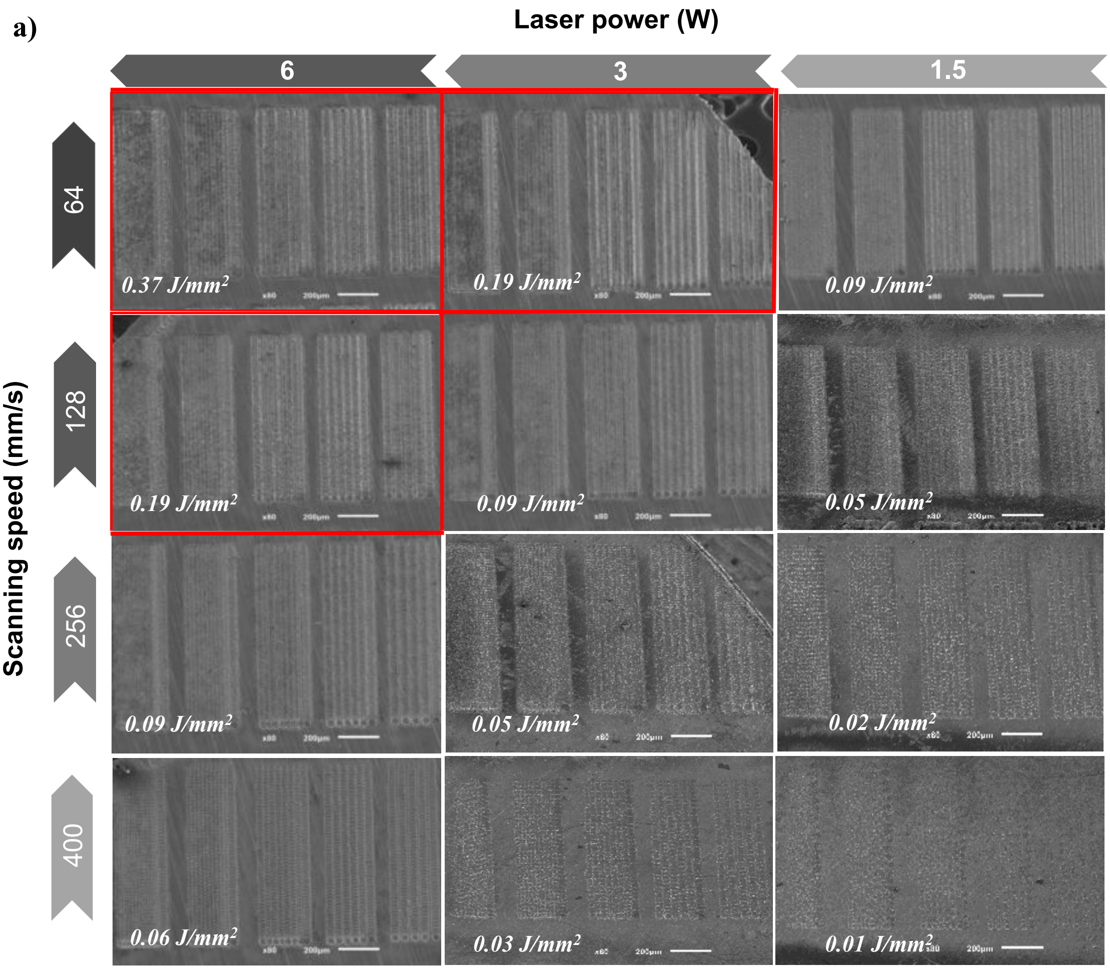

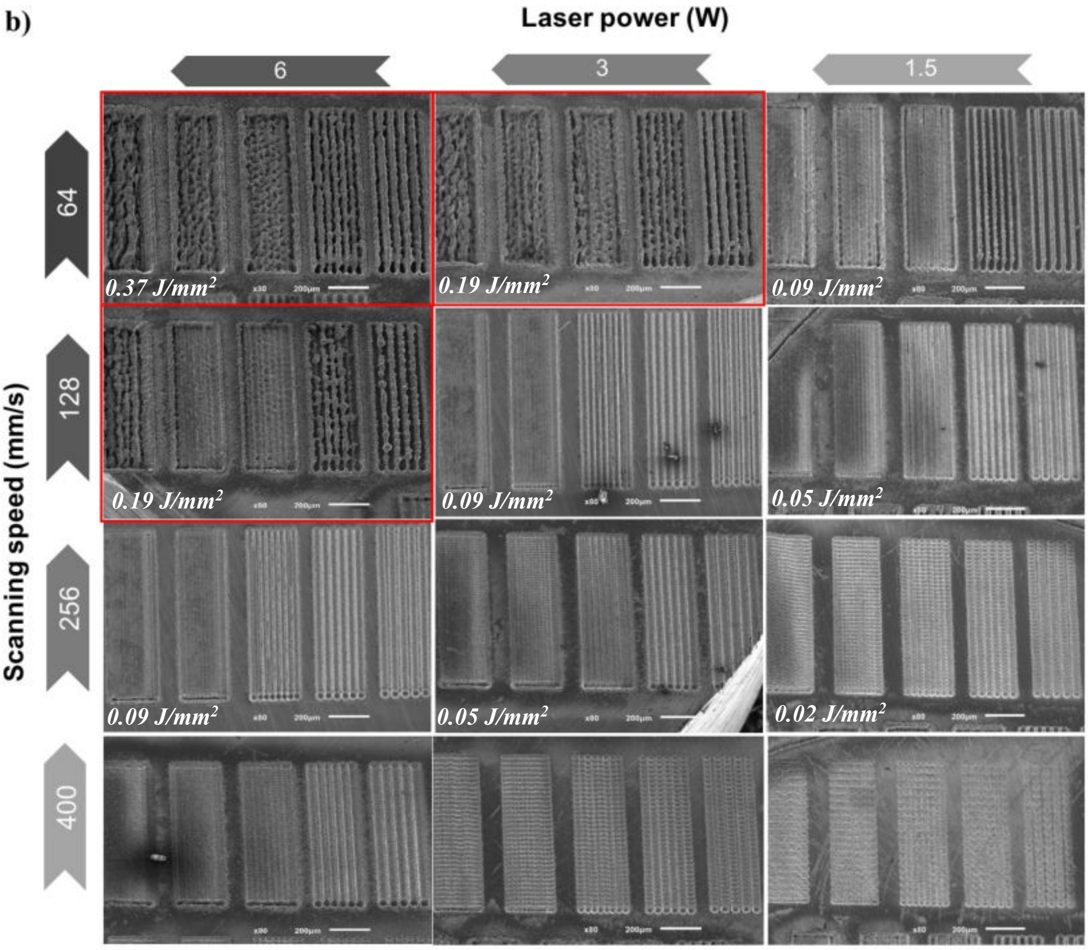
b)
Laser power (W)
6
3
1.5
Scanning speed (mm/s)
64
128
256
400
0.37 J/mm²
0.19 J/mm²
0.09 J/mm²
0.19 J/mm²
0.09 J/mm²
0.05 J/mm²
0.09 J/mm²
0.05 J/mm²
0.02 J/mm²
x80
200µm

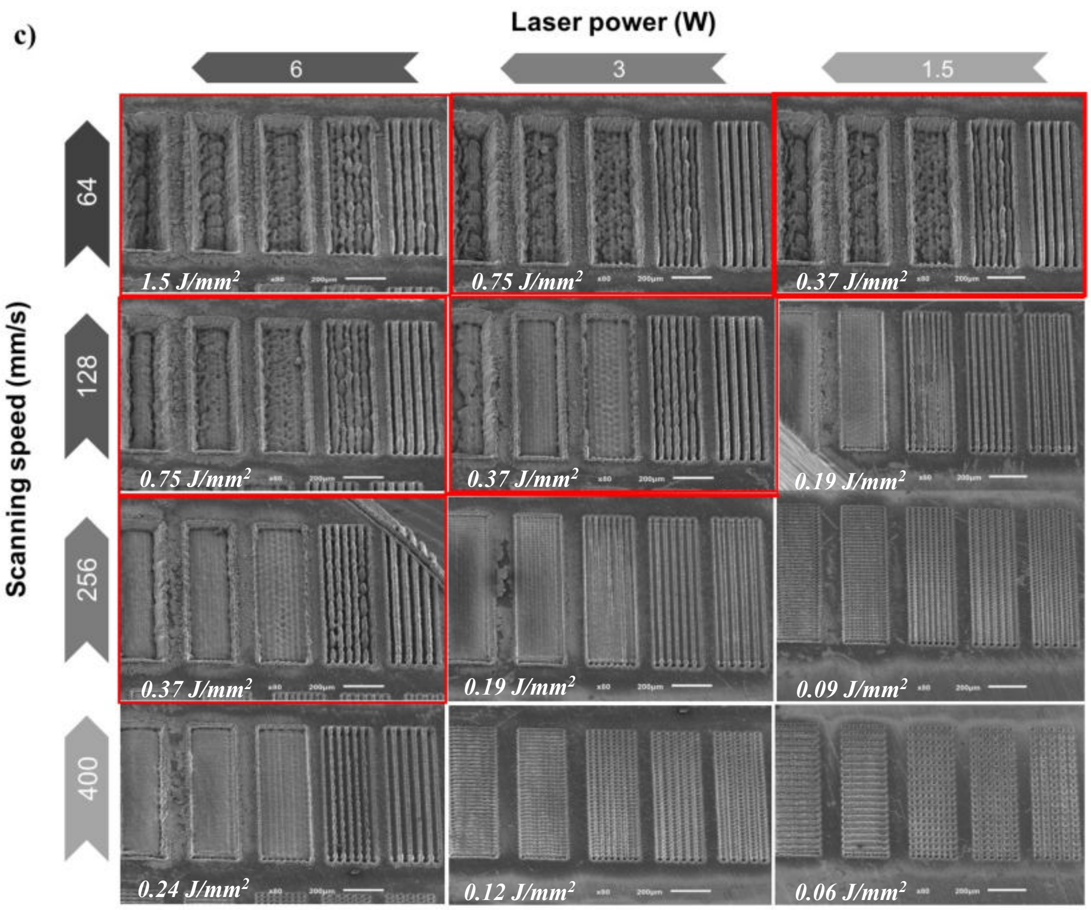

Figure 3.4 SEM micrographs of top surface of laser textured Ti-6Al-4V with different number of laser passes: a) n=1, b) n=4 and c) n=16. Each textured area has 5 grooves formed by lines with different spacing between the lines, varying from 10 to 50 µm (from left to right).

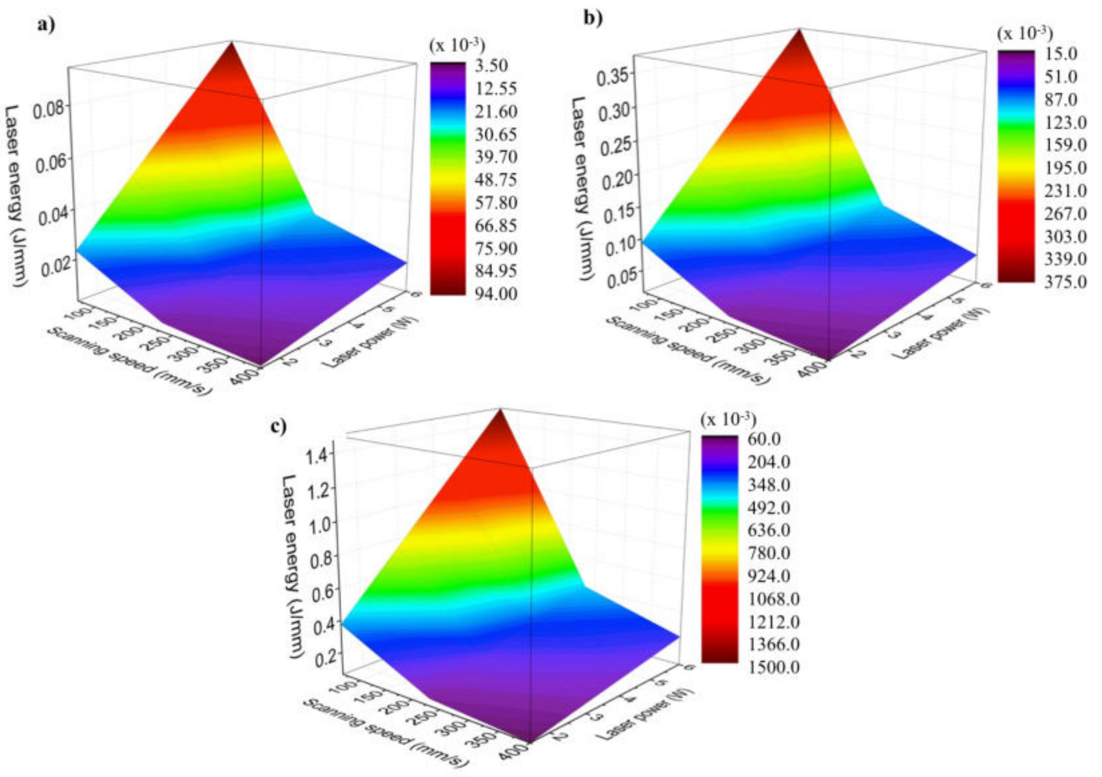

Figure 3.5.3D contour plot correlating laser energy, scanning speed and laser power at constant laser passes. a) n=1, b) n= 4 and c) n=16.

As can be observed from Figure 3.4, high laser energies resulted in higher marking depths as a consequence of greater ablation rates of the material, which produced grooves with a high density of re-solidified material droplets (debris) accumulated after polished areas. On the other hand, low laser energies resulted in melt pool tracks and cleaner surfaces with less re-solidified material droplets. Besides, for the same laser energy density, it is seen that the increase of scanning speed resulted in a smaller overlapping between the successive marks and in a decrease of ablation rate, leading to disruptions (or discontinuities) on the laser marking. It is known that in any laser ablation process, there is a removal of material from substrate by direct absorption of laser energy. In metals this absorption is dominated by the free electrons and the energy is subsequently transferred to lattice phonons by collisions [22]. Thus, fluences above the melting threshold can lead to the formation of pools of molten material on the surface. This molten material will support greater atomic mobilities and solubilities than the solid phase, which result in a rapid material homogenization [23].

Analyzing the micrographs evolution with the number of laser passes, it can be observed that one laser passage (n=1), resulted in a melt pool groove and in a clean surface, without re-solidified droplet, even when the laser energy is high. Moreover, for this case, an excessive scan speed (400 mm/s) combined with low laser power (1.5 W), resulted in deficiencies on the laser marking process, in which it is possible to see the individual laser pulses in some cases. Indeed, this trend was observed for all the laser passes (n=1, n=4 and n=16), meaning that higher scan speeds do not allow a continuous marking on the surface. Besides, as from n=4 the micrographs reveal grooves more chaotic with a high amount of re-solidified material debris spread to the polish areas around, even for low scan speed. This occurs due to the temperature gradients, which develop in melt pools, causing convective flows to circulate material [23]. Also, in laser processing, when temperatures above the melting point are attained, hydrodynamic motion can reshape and redistribute material. Thus, as explained by the Marangoni effect, the liquid is pulled from the warmer to the cooler zone [24].

From the microstructure of the textured zones it is also evident the presence of refined microstructures, as shown in Figure 3.6, which are partly due to deposition of ablated species and partly due to grain refinement resultant from the fast cooling of the molten state, that is usual in laser texturing. Besides, the surface becomes more rough due mainly to the liquid phase formed during the laser scanning, as also observed by other authors [7].

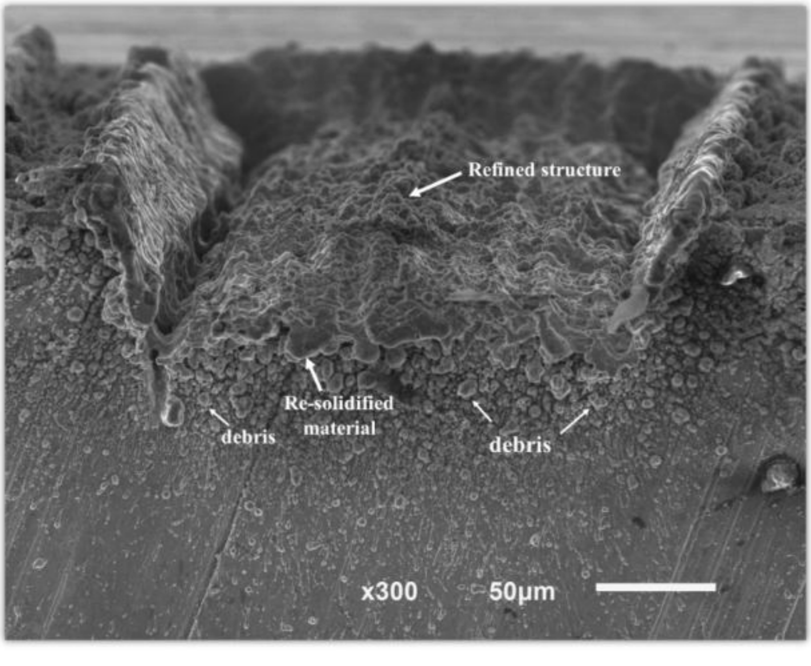

Figure 3.6 Scanning electron micrograph (300x) of cross-section of a groove, illustrating the presence of refined particular.

Figure 3.7 shows the evolution of the line spacing of two higher energy conditions (0.75 and 1.5 J/mm^2), in which for values between 10-30 μm the line spacing is not remarkable in the groove. However, for line spacing ≥ 40 μm it is possible to see the space between each line inside the groove, which turns out to be an opposite result to that objectified, since a groove is not formed. Thus, by analyzing the depth and the amount of re-solidified material inside the groove, for the texturing conditions used, we verify an increase in the amount of material accumulated in the center of the material with the decrease of the line spacing, which corresponds to a greater overlap of the textured areas. This effect is clearly seen for 10 μm lines spacing. In fact, of all the separations between lines studied, the one that results in a greater groove depth (d in the inset of Figure 3.7) is the one that is realized with a separation between lines of 10 μm, disregarding the conditions a.3, a.4, b.3 and b.4, in which the line spacing were 40 and 50 μm, respectively, since they presented varied depths along the cavities formed. Although in Figure 3.7 there are only the micrographs of two conditions, this trend was observed for all the textured conditions.

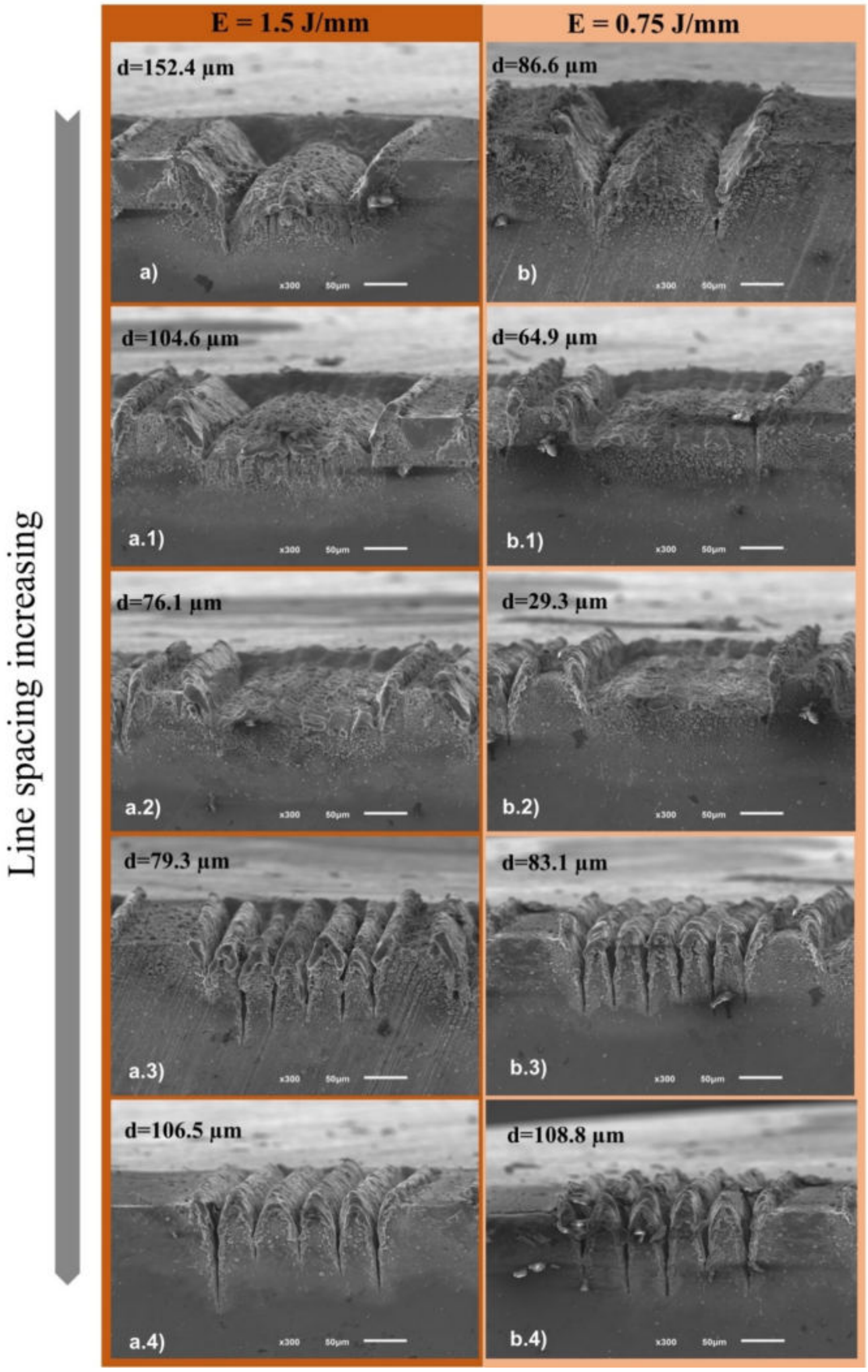

Figure 3.7 Micrographs showing the line spacing effect: a - a.4) correspond to 10 to 50 μm (left side) and b - b.4) correspond to 10 to 50 μm (right side) and energy values of 1.5 and 0.75 J/mm and scanning speed of 64 and 128 mm/s, respectively. Cross-section at 300x. In each micrograph is indicated the groove depth (d).

In general, the number of laser passes had an important role on the resultant groove depth, in which from n=4 to n=16 the average depth tripled for the same texturing conditions. Furthermore, when we compare all the parameters regarding their effects on the surface modification, we conclude that for the same energy value it is possible to obtain a different surface modification, which means that although the energy is the same, each parameter has a different contribution and a particular effect on the final result. Among the conditions analyzed, we conclude that the texturing conditions with 16 laser passes, scanning speeds of 64, 128 and 256 for all the laser power used (presented in Table 3.2) presented the best result, since a greater depth and more homogeneous groove was obtained. Amongst these conditions, for the following studies the groove built with the line spacing of 10 μm was selected, since this condition allowed a more homogeneous groove.

Table 3.2. List of chosen conditions and the samples name.

Sample name	***Conditions***	***Energy density (J/mm)***
A1	P6 v64 n16	1.5
A2	P6 v128 n16	0.75
A3	P6 v256 n16	0.375
A4	P3 v64 n16	0.75
A5	P3 v128 n16	0.375
A6	P1.5 v64 n16	0.375

* P=laser power; v=scanning speed and n= number of passes.

In order to correlate scanning speed, laser power and the depths obtained, a 3D plot is presented in Figure 3.8 for the samples presented in Table 3.2, in which three lines spacing values were considered for each condition: 10, 20 and 30 μm. The groove depths were measured by using image processing (ImageJ) and the obtained values reveal that the maximum depth values were achieved using the lowest scanning speed (64 mm/s). On the other hand, for high scanning speed (above 128 mm/s), low depths are produced, especially for scanning speed of 400 mm/s due to the lower interaction time between the laser beam and the machined surface [24]. From this study we also confirm the effect of the line spacing on the groove depth: the groove depth decreases as the line spacing increases. This behavior may be a consequence of greater material removal in the cases of smaller line spacing values.

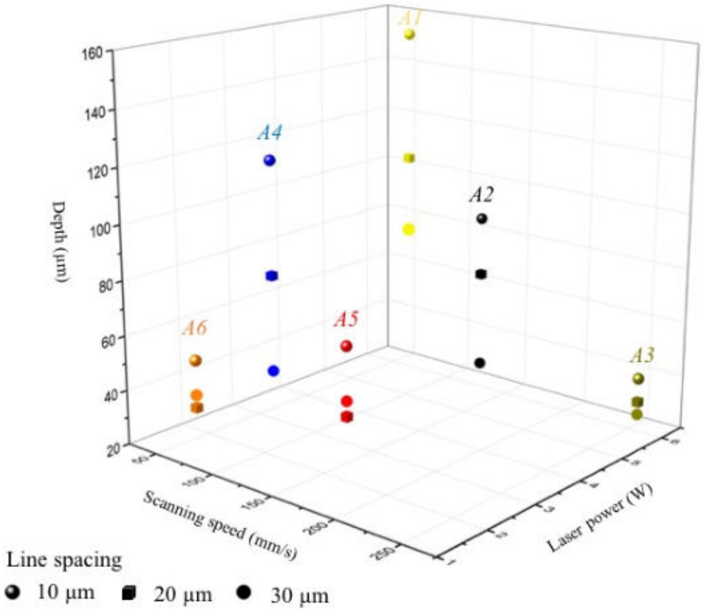

Figure 3.8 3D plot correlating scan speed (mm/s), laser power (W) and depth (μm) of the samples analyzed for each line spacing (10, 20 and 30 μm).

3.3.2 Surface oxidation analysis

Morphology and composition

As already mentioned, an oxide layer can be obtained by laser texturing the surface. During the laser texturing, the samples are superficially melted, by the laser beam, leading to oxygen diffusion through the molten material and, thus, to the oxidation of the material (titanium in the present study). In particular, by changing the parameters used for laser texturing, different oxidation states can be achieved. For the purpose of the present work, the six conditions (Table 3.2) of laser texturing were analyzed regarding oxide layer composition (but only with 10 μm lines spacing). The XRD diffractograms for angles from 20° to 80° are shown in Figure 3.9. The peaks presented in the XRD diffractograms reveal the presence of α-Ti (ICDD 1-1198) and Ti_2O phases for all the samples, being α-Ti the main phase formed. Some vestiges of Ti_6O phase was also observed by the presence of a very weak and broad peak around 38° [25–27]. No peaks of TiO_2 (rutile), oxynitrides and β-Ti are visible in any case.

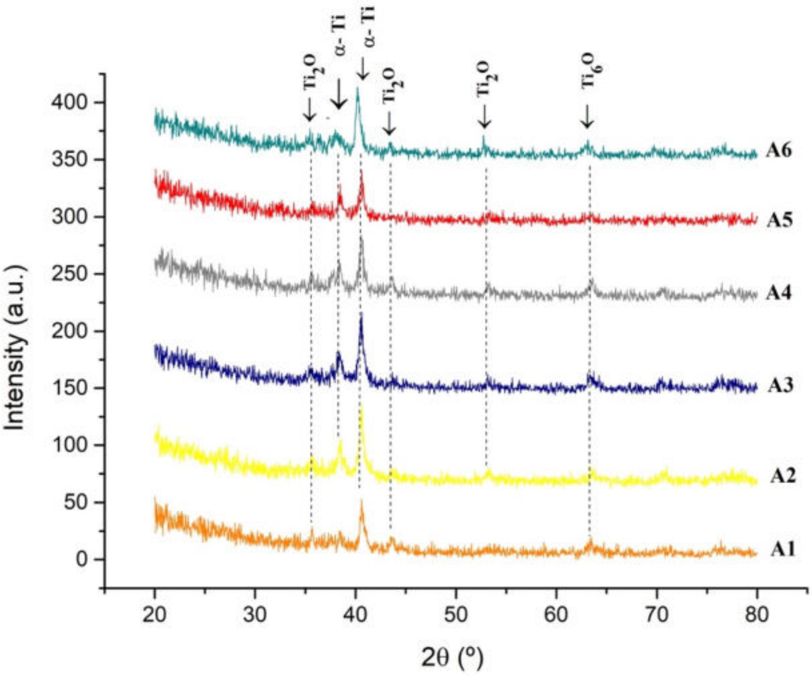

Figure 3.9 XRD diffractogram of the textured samples at different conditions.

The formation of α-Ti phase was already discussed in literature [28], which is referred to as "alpha-case". Titanium has two allotropic forms: α-Ti (hexagonal close-packed form - hcp) and β-Ti (body-centered cubic form - bcc). The α-Ti is an interstitial solid solution Ti(O), which forms a thick oxygen-rich metallic layer under the main oxide layer on titanium surface. This phenomenon occurs during the process of high-temperature oxidation, when the concentration of oxygen is high, and thus, at temperatures above 600 °C, α-Ti is capable of dissolving a great amount of oxygen (33 at.%) and nitrogen (23 at.%), which locate themselves in the interstitial positions of the lattice. The amount of oxygen present in this phase hardens the layer and it is responsible to its embrittlement and, depending on the thickness of the layer, the generated relaxing stress can cause its exfoliation [29].

The thickness of the Ti-oxide layer can be seen in the SEM images shown in Figure 3.10. The Ti-oxide layer has a thickness around 1.5 μm and the layer cross-section show a dense and rough oxide film without pores on the surface. EDS analysis of sample A2 in two zones (Z1 and Z2) is presented in Figure 3.10 (Complement table below the images). Z1 refers to the oxide layer on the surface and Z2 is the substrate zone. Oxygen was detected in both zones, while the other elements (Al and V) were detected only in Z2. It can be also observed a slight increase in oxygen percentage in Z1, which can indicate a higher oxidized state of the surface, in comparison to Z2. This emphasizes the oxide layer formation.

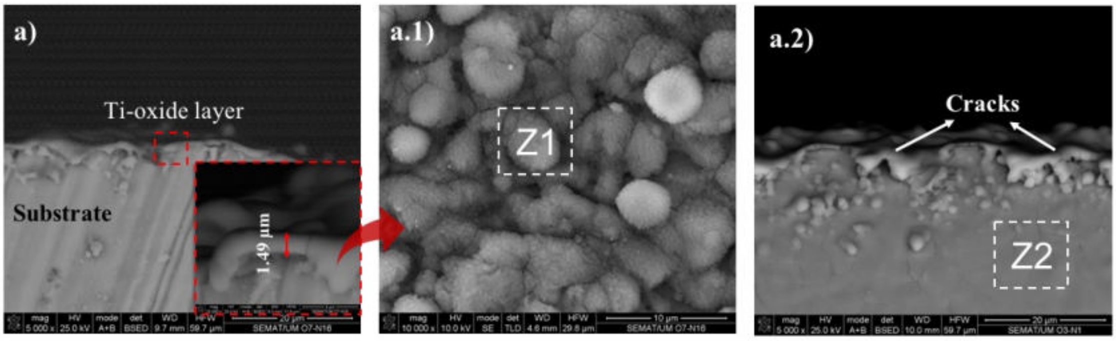

	Element	O	Ti	Al	V
Z1	Wt (%)	28.28	71.72	--	--
	At (%)	54.14	45.86	--	--
Z2	Wt (%)	31.34	62.37	4.16	2.13
	At (%)	56.66	37.67	4.46	1.21

Figure 3.10 Micrographs of Titanium oxide layer cross-section (Sample A2) and EDS in different sample zones.

Electrical insulation capacity

In order to evaluate the electrical insulation capacity of the oxide layer formed on titanium alloy surface during the laser texturing, electrical measurements were performed. Taking into account that all the studied samples (A1 to A6) presented the same phases on the surface, and since the oxide layer is too thin to have a significantly variation regarding its insulation property, the conditions A1, A2 and A4 were chosen for this study. For this purpose, the electrical measurements were performed by using four-point probe method, by applying an electrical current and measuring the voltage resultant. Assuming a uniform oxide layer thickness, the resistivity (ρ) can be obtained by using the relation $\rho = Ro * t$, where t is the oxide layer thickness and R_0 is the measured sheet resistance [30]. The obtained I-V curves for the 3 samples are shown in Figure 3.11(a). The resistivity of the oxide layer was obtained measuring through a silver wire deposited and sintered into the groove (as shown in scheme of Figure 3.3a). The obtained resistivities are not compatible with the resistivity of an insulating material. Several factors may have influenced this result. It is well known that the electrical properties of titanium oxide strongly depended depends on the layer composition, oxygen pressure, layer thickness and so on [30]. Furthermore, the defect disorder and O/Ti stoichiometry play an important role in the insulation property of titanium oxide [31]. Indeed, our previous studies showed that α-Ti is the main phase (but not unique-by XRD) and the SEM studies showed the presence of superficial defects (microcracks and discontinuities on the layer) resulting from laser treatment, which may have been detrimental to electrical insulation property of the layer. These defects in the insulation layer may lead to the current applied on the wire to flow to the metal substrate, losing efficiency. In literature, the studies are more focused on the electrical properties of TiO_2 phase, which is the mainly oxide of Ti. In fact, this material has a great insulation capacity, as shown by Ju et al [31], with resistivity (*ρ)* in a range of 0.0026 - 0.101 Ω.m, for different film thickness.

Despite this result, a simulation was performed (through *TINA* software) to evaluate the use of the fabricated silver wire to transport a current between two points. Using the measured electrical resistance values (as shown in section 2), a current of 100 mA was applied between the ends of the silver wire, resulting that 90.95 mA flows through the silver wire, while only 9.05 mA flows through the substrate, i.e. the silver wire efficiency is above 90% when Ti-oxide and α-Ti are simulated with the ohmic values presented in Figure 3.11(b).

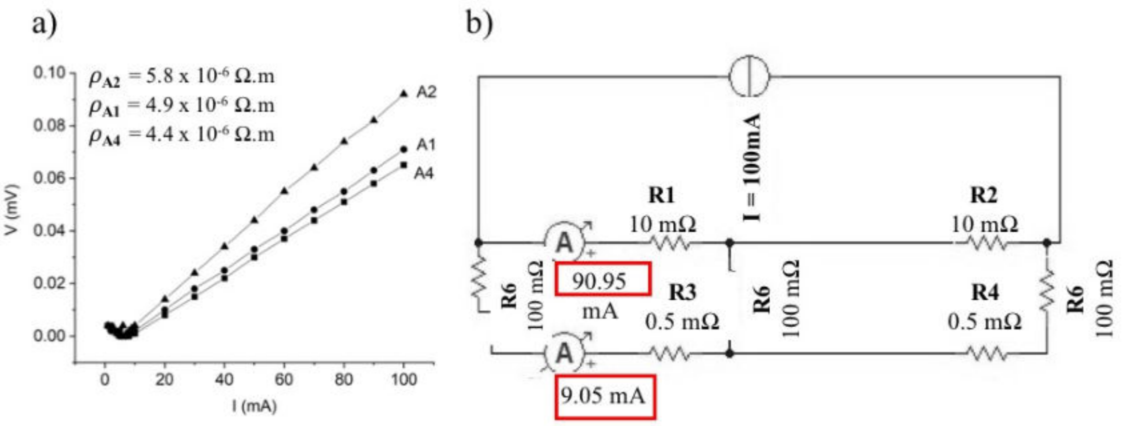

Figure 3.11. a) I-V curves for samples A1, A2 and A4. b) Electrical circuit from *TINA* software simulation.

On the other hand, when the resistors are removed from the circuit, the wire efficiency decreases to 50 %. This means that the Ti-oxide/α-Ti layer obtained after laser texturing is efficient to insulate the metal substrate for the applied current.

3.4 Conclusions

The study presents laser surface texturing of titanium alloy (Ti-6Al-4V) by using a Nd:YAG laser source. The texture was performed by scanning the laser along the surface producing grooves formed by consecutive lines having different line separation. A detailed characterization of the textured surface as a function of texturing parameters was performed. Moreover, the study of the Ti-oxide layer, formed during the laser texturing, has been undertaken. Besides, the electrical insulation capacity of this Ti-oxide layer was analyzed through current-voltage measurements and by using *TINA* simulation software. From the above mentioned investigation, the following conclusions may be drawn:

(1) Laser surface texturing of Ti-6Al-4V with linear and dimple structure geometries were successfully developed with Nd:YAG laser radiation. The periodic lines revealed low amount of surface defects. For the same value of laser energy density, but different combination of the processing parameters, different characteristics of the textured grooves were obtained. The depth of the textured grooves increases as the number of laser passes increase.

(2) Due to the fast cooling of the molten state of the surface promoted by laser irradiation, the presence of refined microstructure is evident. In order to obtain a groove with a considerably depth and low density of debris on the surface, the best laser processing parameters are: intermediate scanning speeds (64-128 mm/s), high laser power (1.5 W) and the maximum number of laser passes (n=16).

(3) Regarding the Ti-oxide layer formed as a result of laser texturing, the XRD study revealed peaks of Ti oxides and α-Ti phases. The thickness of the Ti-oxide/α-Ti layer is around 1.5 μm and the layer cross-section showed a dense and rough oxide film without pores on the surface.

(4) The insulation capacity of the Ti-oxide/α-Ti layer obtained from laser texture was performed. According to the results, this layer is capable of a good electrical insulation when a current of 100 mA was applied in the circuit through a silver wire.

Conflicts of interest

The authors have no conflict of interest to declare.

Acknowledgement

This work has been supported by FCT (Fundação para a Ciência e Tecnologia -Portugal) in the scope of the projects UID/EEA/04436/2019 and NORTE-01-0145-FEDER-000018-HAMaBICo and Add.Additive_Manufacturing to Portuguese Industry_POCI-01-0247-FEDER-024533. Thank the CNPq (205791/2014-0) and CAPES for the financial support.

FCT
Fundação para a Ciência e a Tecnologia
Cofinanciado por:
COMPETE 2020
PORTUGAL 2020
UNIÃO EUROPEIA
Fundo Europeu de Desenvolvimento Regional
CNPq
SCIENCE WITHOUT BORDERS

References

[1] E.H. Ledet, B. Liddle, K. Kradinova, S. Harper, Outcomes : a Review, (2018) 41–51. doi:10.2147/IEH.S133518.Smart.

[2] V.Y. Zadorozhnyy, E. V. Kaevitser, A.N. Kopylov, Y. V. Borisova, V. V. Sudarchikov, R.S. Khasenova, M. V. Gorshenkov, M.Y. Zadorozhnyy, S.D. Kaloshkin, Synthesis of the hydroxyapatite coatings on the Ti substrates by mechanical alloying, Surf. Coatings Technol. 281 (2015) 157–163. doi:10.1016/j.surfcoat.2015.09.056.

[3] E. Mohseni, E. Zalnezhad, A.R. Bushroa, Comparative investigation on the adhesion of hydroxyapatite coating on Ti-6Al-4V implant: A review paper, Int. J. Adhes. Adhes. 48 (2014) 238–257. doi:10.1016/j.ijadhadh.2013.09.030.

[4] S. Shaikh, S. Kedia, D. Singh, M. Subramanian, Surface texturing of Ti6Al4V alloy using femtosecond laser for superior antibacterial performance, (n.d.).

[5] O. Raimbault, S. Benayoun, K. Anselme, C. Mauclair, T. Bourgade, A.M. Kietzig, P.L. Girard-Lauriault, S. Valette, C. Donnet, The effects of femtosecond laser-textured Ti-6Al-4V on wettability and cell response, Mater. Sci. Eng. C. 69 (2016) 311–320. doi:10.1016/j.msec.2016.06.072.

[6] A. Cunha, A.M. Elie, L. Plawinski, A.P. Serro, A.M. Botelho Do Rego, A. Almeida, M.C. Urdaci, M.C. Durrieu, R. Vilar, Femtosecond laser surface texturing of titanium as a method to reduce the adhesion of Staphylococcus aureus and biofilm formation, Appl. Surf. Sci. 360 (2016) 485–493. doi:10.1016/j.apsusc.2015.10.102.

[7] W. Pfleging, R. Kumari, H. Besser, T. Scharnweber, J.D. Majumdar, Laser surface textured titanium alloy (Ti-6Al-4V): Part 1 - Surface characterization, Appl. Surf. Sci. 355 (2015) 104–111. doi:10.1016/j.apsusc.2015.06.175.

[8] A. Soveja, E. Cicală, D. Grevey, J.M. Jouvard, Optimisation of TA6V alloy surface laser texturing using an experimental design approach, Opt. Lasers Eng. 46 (2008) 671–678. doi:10.1016/j.optlaseng.2008.04.009.

[9] L.M. Vilhena, M. Sedlaček, B. Podgornik, J. Vižintin, A. Babnik, J. Možina, Surface texturing

by pulsed Nd:YAG laser, Tribol. Int. 42 (2009) 1496–1504. doi:10.1016/j.triboint.2009.06.003.

[10] I. Etsion, State of the Art in Laser Surface Texturing, J. Tribol. 127 (2005) 248. doi:10.1115/1.1828070.

[11] P.A. Sugioka K, Meunier M, Laser precision microfabrication, Springer Verlag Limited, Berlin, Heidelberg, 2010.

[12] J. Bonse, S. V. Kirner, M. Griepentrog, D. Spaltmann, J. Krüger, Femtosecond laser texturing of surfaces for tribological applications, Materials (Basel). 11 (2018) 1–19. doi:10.3390/ma11050801.

[13] M. Erdoğan, B. Öktem, H. Kalaycıoğlu, S. Yavaş, P.K. Mukhopadhyay, K. Eken, K. Özgören, Y. Aykaç, U.H. Tazebay, F.Ö. Ilday, Texturing of titanium (Ti6Al4V) medical implant surfaces with MHz-repetition-rate femtosecond and picosecond Yb-doped fiber lasers, Opt. Express. 19 (2011) 10986. doi:10.1364/OE.19.010986.

[14] Z. Wu, Y. Xing, P. Huang, L. Liu, Tribological properties of dimple-textured titanium alloys under dry sliding contact, Surf. Coatings Technol. 309 (2017) 21–28. doi:10.1016/j.surfcoat.2016.11.045.

[15] 5–50. doi:10.1177/0885328205052974 Kurella, A., & Dahotre, N. B. (2005). Review paper: Surface Modification for Bioimplants: The Role of Laser Surface Engineering. Journal of Biomaterials Applications, 20(1), Wash2013, (n.d.).

[16] T. Jwad, S. Deng, H. Butt, S. Dimov, Laser induced single spot oxidation of titanium, Appl. Surf. Sci. 387 (2016) 617–624. doi:10.1016/j.apsusc.2016.06.136.

[17] E. Akman, E. Cerkezoglu, Compositional and micro-scratch analyses of laser induced colored surface of titanium, Opt. Lasers Eng. 84 (2016) 37–43. doi:10.1016/j.optlaseng.2016.03.026.

[18] Z.W. Wang, Y.M. Wang, Y. Liu, J.L. Xu, L.X. Guo, Y. Zhou, J.H. Ouyang, J.M. Dai, Microstructure and infrared emissivity property of coating containing TiO2 formed on titanium alloy by microarc oxidation, Curr. Appl. Phys. 11 (2011) 1405–1409. doi:10.1016/j.cap.2011.04.011.

[19] L. Mi, P. Xu, P.N. Wang, Experimental study on the bandgap narrowings of TiO2 films calcined under N2 or NH3 atmosphere, Appl. Surf. Sci. 255 (2008) 2574–2580. doi:10.1016/j.apsusc.2008.07.150.

[20] M.S.P. Sarah, M.Z. Musa, M.N. Asiah, M. Rusop, Electrical conductivity characteristics of

TiO2thin film, 2010 Int. Conf. Electron. Devices, Syst. Appl. ICEDSA 2010 - Proc. (2010) 361–364. doi:10.1109/ICEDSA.2010.5503040.

[21] Hamabico, (n.d.). www.hamabico.pt (accessed February 25, 2019).

[22] A. Allmen, Martin V. and Blatter, Laser-beam interactions with materials: physical principles and applications., Springer Science & Business Media, 2013. doi:10.1088/0034-4885/33/3/306.

[23] J. Ion, Laser processing of engineering materials: principles, procedure and industrial application., Elsevier, 2005. doi:10.1039/b900654k.

[24] T.D. Bennett, D.J. Krajnovich, C.P. Grigoropoulos, P. Baumgart, A.C. Tam, Marangoni Mechanism in Pulsed Laser Texturing of Magnetic Disk Substrates, J. Heat Transfer. 119 (1997) 589. doi:10.1115/1.2824146.

[25] A. Pérez Del Pino, P. Serra, J.L. Morenza, Coloring of titanium by pulsed laser processing in air, Thin Solid Films. 415 (2002) 201–205. doi:10.1016/S0040-6090(02)00632-6.

[26] A. Pérez Del Pino, P. Serra, J.L. Morenza, Oxidation of titanium through Nd:YAG laser irradiation, Appl. Surf. Sci. 197–198 (2002) 887–890. doi:10.1016/S0169-4332(02)00447-6.

[27] A.J. Antończak, Ł. Skowroński, M. Trzcinski, V. V. Kinzhybalo, Ł.K. Łazarek, K.M. Abramski, Laser-induced oxidation of titanium substrate: Analysis of the physicochemical structure of the surface and sub-surface layers, Appl. Surf. Sci. 325 (2015) 217–226. doi:10.1016/j.apsusc.2014.11.062.

[28] G.Z. Chen, D.J. Fray, T.W. Farthing, Cathodic deoxygenation of the alpha case on titanium and alloys in molten calcium chloride, Metall. Mater. Trans. B Process Metall. Mater. Process. Sci. 32 (2001) 1041–1052. doi:10.1007/s11663-001-0093-8.

[29] H. Dong, X.Y. Li, Oxygen boost diffusion for the deep-case hardening of titanium alloys, Mater. Sci. Eng. A. 280 (2000) 303–310. doi:10.1016/S0921-5093(99)00697-8.

[30] H. Kim and C. M. Gilmore, Characterization of calcium-binding sites in development-specific protein S of Myxococcus xanthus using site-specific mutagenesis, J. Biol. Chem. 263 (1988) 1199–1203. doi:10.1063/1.371708.

[31] Y. Ju, T. Chen, Z. Wu, Y. Jiang, Electrical properties of amorphous titanium oxide thin films, Adv. Condens. Phys. 33 (2012) 676–679. doi:10.1155/2013/365475.

Chapter 4 - Laser printing of silver-based communication system on Ti-6Al-4V substrate for smart implants applications

Under review in Journal of Optics and Laser Technology

C. G. Moura[1], O. Carvalho[1], M. F. Cerqueira[2,3], L.M.V. Gonçalves[1], V. H. Magalhães[1], R.S.F Pereira[4], R. M. Nascimento[4], F.S. Silva[1]

[1]CMEMS-UMinho, University of Minho, 4800-058, Guimarães, Portugal
[2]Centro de Física, University of Minho, 4710-057, Braga, Portugal
[3]International Iberian Nanotechnology Laboratory (INL), 4715 Braga, Portugal
[4]Federal Institute of Education Science and Technology of Santa Catarina, IFSC, Florianópolis, Brazil
[5]Materials Science and Engineering Post-Graduate Program, UFRN, 59078-970 Natal, Brazil

*Corresponding author – C. G. Moura (caroline.materiais@gmail.com)

Abstract

Endow the implant with intrinsic capabilities such as sensing, actuating and control to solve problems can be determinant for its long-term success. The capacity of early diagnosis of failures and the ability to remedy them are necessary to minimize expensive complications and reducing revision procedures. Ti6Al4V is the most used titanium alloy for implant's fabrication. In this sense, this work presents a promising approach to print communication systems by using laser technology, aiming integrate the smart components on titanium implants. Silver wires have been printed on Ti6Al4V surface in order to conduct electrical current. To minimize current loss for the substrate, titanium oxide layer has been produced by different methods (laser and anodization). Laser sintering (LS) has been also compared to a conventional method (Hot-pressing- HP) to consolidate the silver powder into the cavities. Electrical resistivity of the wire has been calculated and the results showed a great wire contribution for the electrical flow in laser group. The thin oxide layers produced have demonstrated good insulation capacity, minimizing the current loss from the wire to the substrate.

4.1 Introduction

Commercial pure titanium and titanium alloy (Ti6Al4V) are still the elected materials in the fabrication of implants, due to their great biocompatibility and mechanical properties [1,2]. Although it has a high success rate of these implants, some failures are still arising, leading to an early revision surgery and implant replacement. Many studies have been undertaken to improve the titanium implants properties, such as osseointegration, bioactivity, surface and the material itself [3–5]. However, the early diagnosis and remediation of failures may play a prominent role for increasing the implant's lifetime, minimizing expensive complications and reducing revision procedures [6].

In this context, smart implants concept has been extensively explored in the development of new implants endowed with several capacities. Smart implants are defined as implantable devices that provide not only therapeutic benefits, but also diagnostic capabilities and they have been applied in knee arthroplasty, hip arthroplasty, fracture fixation and others. To date, smart implants have been used to measure several physical parameters from inside the body (such as pressing, force, strain, displacement and temperature) [7]. The data prevenient from the smart implants have led to the refinement and improvement of design and implant technology. Despite recent technological advances, the smart implants are yet part of the daily clinical. This is because the actual sensors technology requires significant modification of the implants design which may compromise its long-term performance.

Based on the foregoing, the need to integrate the smart components (sensors, actuators and antennas) and to establish a communication among them and an external receptor has emerged. However, the assembly of these elements along the implant's surface, in a microscale, with no jeopardize the implants design is still a challenge. [8,9]. Nonetheless, with the advances in the 3D printing technology with multi-material approaches, it is feasibly to print, layer by layer, implants where a communication system (comprised by sensors and actuators materials) may be integrated, giving rise to a component with an internal communication array of wires and local surface areas with the capacity to sense or actuate. This potential application is described in details in our previous work [10]. The overall idea presented in Figure 4.1.

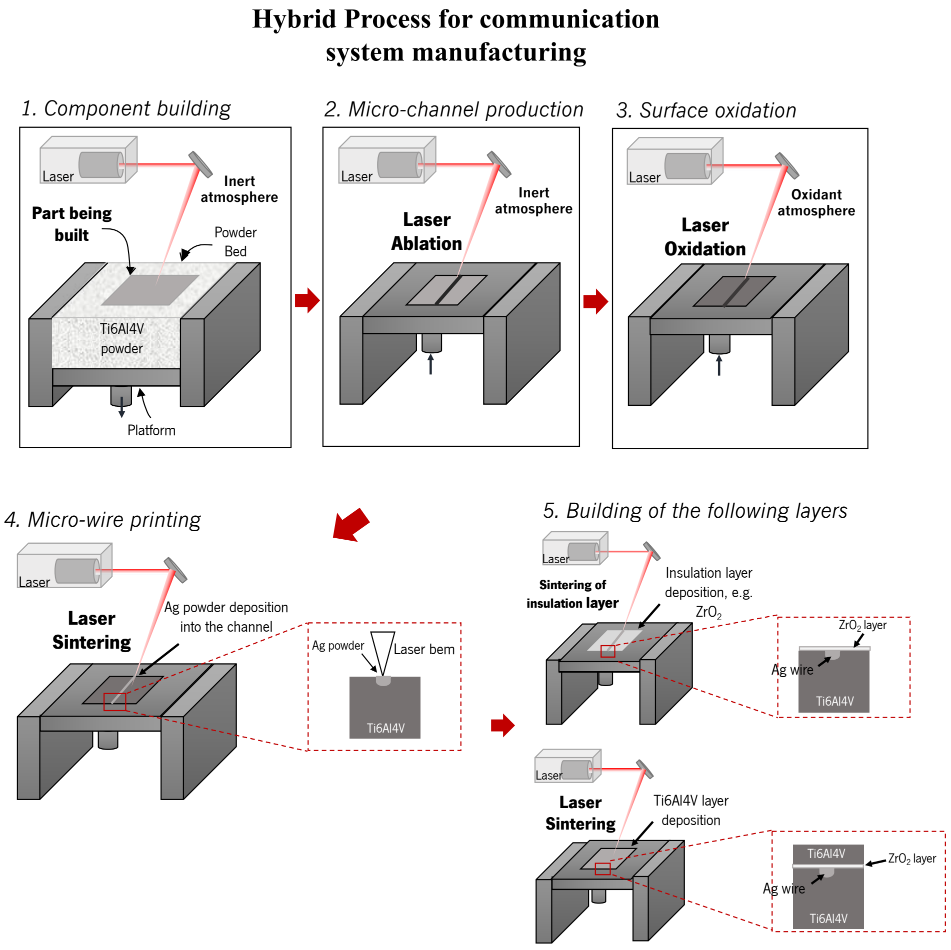

Figure 4.1 Scheme of the communication system production steps by laser additive manufacturing.

In this sense, this work concerns of print the communication systems on titanium alloy surface by using laser technology, aiming integrate the smart components on titanium implants. For this, micro-cavities were created on Ti6Al4V substrate, where silver powder was then deposited and sintered, forming a wire. In order to avoid or reduce the electrical current loss to the substrate, an insulator layer is necessary between the Ti6Al4V substrate and the silver wire. Two approaches were tested to create TiO_2 films on the surface, since it presents insulation property. The electrical resistance of the wires was measured by using the four-probe method.

4.2 Experimental details

4.2.1 Micro-cavities production

A Nd:YAG laser (OEM Plus, working in wavelength of 1064 nm and 6 W of maximum power) was used to produce the micro-cavities on the surface of a 2 mm thick Ti6Al4V titanium alloy target. To create the micro-cavities, a strategic design was used, in which overlapping lines with different wobble amplitudes were built by laser, aiming to produce a micro-cavity with more rounded shape (Figure 4.2). A sequence of 10 wobbles lines with different widths (from 25 to 250 µm) overlapped was performed, where the scanning speed has been changed in each one (from 20 to 2 mm/s), in order to better distribute the laser energy along the cavity. While the wobble amplitude increased, the scanning speed has decreased aiming to machine more evenly from the inside out of the micro-cavity. The final width of the cavity was around 250 µm. The laser is pulsed, and the spot has a diameter of 3 µm, then each laser textured line consists in a sequence of several pulses with an overlap area.

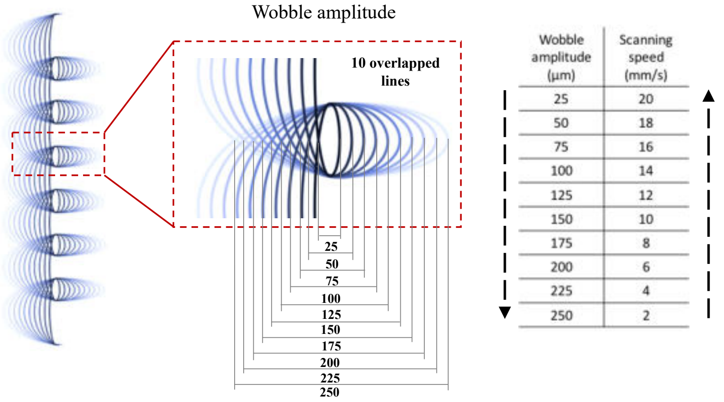

Wobble amplitude (µm)	Scanning speed (mm/s)
25	20
50	18
75	16
100	14
125	12
150	10
175	8
200	6
225	4
250	2

Figure 4.2 Schematic drawing of the micro-cavity build produced by laser.

4.2.2 Surface oxidation

The anodic oxidation was carried out in potentiostatic mode at room temperature using 0.4 M H_3PO_4 as electrolyte. A rectangular graphite plate was used as the counter-electrode. The exposure area was 8 mm in diameter of the sample in all the experiments. Two voltages were tested: 20 V and 120 V for 1 minute, in order to evaluate the effect of the thickness in the insulation performance of the film. This results in films with different colors, being purple and green for 20 V and 120 V condition, respectively.

For the laser oxidation a Nd:YAG (1064 nm of wavelength) was used to make a thin texture on the surface, in order to obtain the oxidized layer. A laser energy of 0.094 J/mm was used to irradiate all the surface.

The morphology of the oxidized films was analyzed using scanning electron microscope (SEM - FEI Nova 200) and the phase composition was analyzed by X-ray diffraction (XRD- Bruker D8 Discover) using a CuKα radiation at a grazing angle of 1°. The thickness of the anodized films was measured by an atomic force microscope (AFM - Bruker), using a scan rate of 0.7 Hz at room temperature in tapping in air mode. In this regard, the samples were carefully polished till mirror finishing. The half of the surface was then covered by a piece of DUPONT™ KAPTON® tape (polyamide film resistant to acid), in order to obtain two zones: the anodized zone and the non-anodized zone.

4.2.3 Silver powder deposition

In the silver (Ag) wire printing, silver powder (≥ 99% pure) with an average grain size of 230 nm, from Metalor Technologies-USA, was deposited and compacted into the micro-cavity on Ti6Al4V substrate. After the deposition, the powder was compacted by using a pressure of 8 MPa to ensure the total accommodation of the powder into the micro-cavity. The excess of the powder on the surface was removed through polishing with P800 grit SiC paper. This step is illustrated in Figure 4.3.c).

4.2.4 Micro-wire printing

In the silver wire printing, two techniques were performed to sinter the powder deposited on the cavities, laser sintering (LS) and hot-pressing (HP), in order to compare a conventional method with laser technique in terms of densification and quality of the wire (Figure 4.3.d). Laser sintering was performed by a Nd:YAG (Sisma - 1064 nm of wavelength) with a spot size of 0.3 μm and 40 W of power. An energy of 10 Joules was used in all the samples. This value of energy was chosen as the best condition to melt the powder with less defects after several parameters' tests.

In the conventional method, silver wire has been prepared by hot-pressing the silver powder at 960 °C under a normal pressure of 1 bar in vacuum in a graphite die. For this, silver powder is deposited on top of the micro-cavity of Ti6Al4V sample. The silver wires were characterized by scanning electron microscope (SEM - FEI Nova 200) in order to evaluate the quality of the wire, in terms of densification. Table 4.1 shows the different types of Ti6Al4V samples produced and tested in this work.

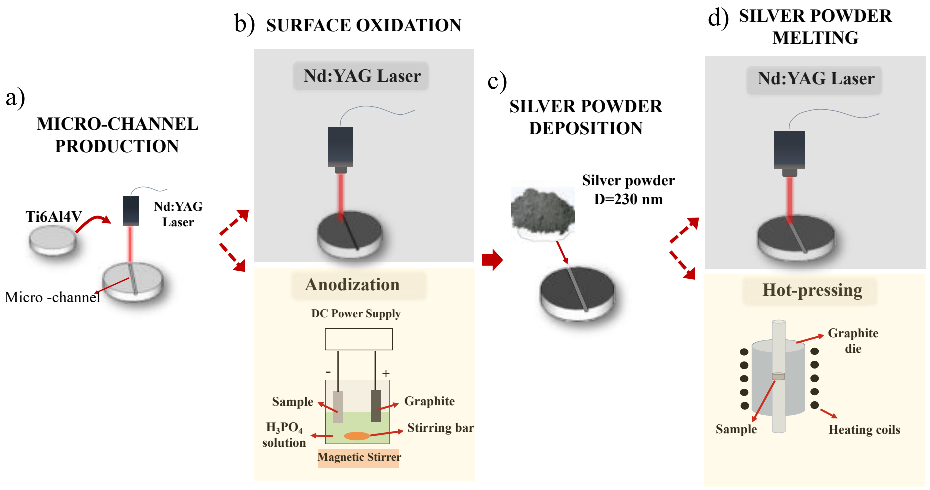

Figure 4.3. Experimental set up.

Table 4.1. Ti6Al4V samples details.

Sample	**Surface oxidation method**	**Wire sintering method**
ST	No oxidation	Laser
STLO	Laser oxidation	Laser
STA20	Anodization	Laser
STA120	Anodization	Laser
STHP	No oxidation	Hot-pressing
ST20HP	Anodization	Hot-pressing
ST120HP	Anodization	Hot-pressing

4.2.5 Electrical measurements of the wires

In order to evaluate the electrical conductivity of the printed silver wires, the four-point probe method has been used. In this method a current is passed through the outer probes and induces a voltage in the inner voltage probes, resulting in a I x V curve. The range of applied current was 0.01 to 0.1 Ampere. In order to exclude the bias of the printed wires, the resistivity (ρ) was calculated using Eq. 1 to evaluate the electrical performance. The resistance values were taken from V x I curves.

$$\rho = R\frac{A}{L} \qquad (1)$$

Where ρ is the resistivity, R is the resistance measured on the wire, L is the distance between each probe, and A is the cross-sectional area of the Ag wire. To obtain accurate resistivity, the actual cross-sectional area was assumed to be a uniform wire with approximately 250 μm of diameter. This equation for the resistivity calculation was chosen considering the wire deposited on an insulating substrate, in which all the current flows through the wire.

4.3 Results and discussion

4.3.1 Surface morphology of the micro-cavities

Figure 4.4 shows the SEM micrographs of the micro-cavities produced by laser on Ti-6Al-4V surface processed in air. The micro-cavity presents a width and depth around 250-300 μm, as expected. The strategy used to produce the micro-cavities consists of an overlap of different wobbles' width, starting from 25 μm and increasing until the desired width is reached, in this case, 250 μm. This strategy resulted in a round-shaped cavity, since the emitted laser energy was better distributed along the cavity. It is notable a rough surface into the cavity with flat walls.

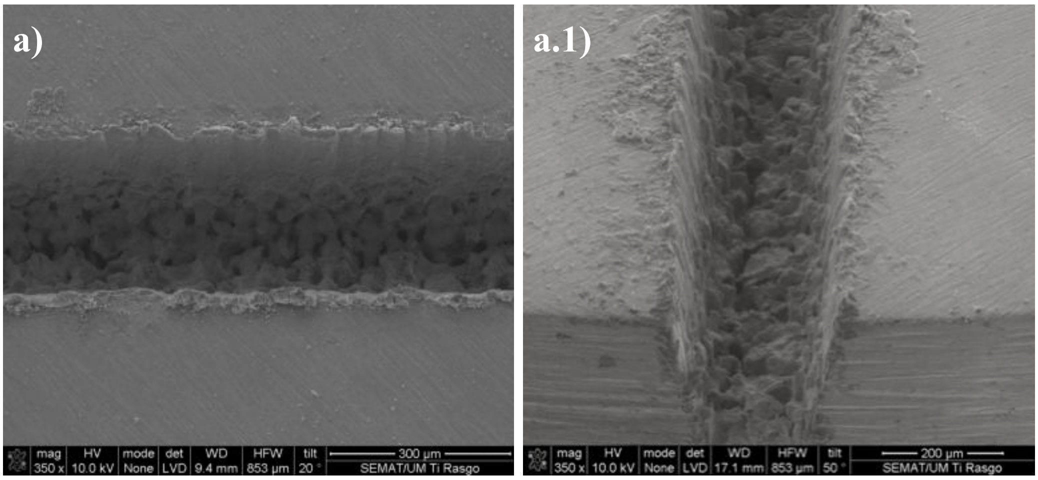

Figure 4.4.SEM micrographs of the micro-cavity created by Nd:YAG laser.

4.3.2 Oxidized surface characterization

Oxidation by anodization

The oxidized surface from the micro-cavity production by laser was compared to the surface oxidation by anodization method. In order to evaluate the electrical insulation capacity of the anodizing oxides, two different voltages were studied, namely 20 V and 120 V. The tested conditions were chosen based on other studies reported in literature, taking into account the achievement of a uniform film with no porosity and cracks-free in order to obtain great insulation properties [11–13]. In terms of the oxide phases formation, the results of the phase analysis by XRD are shown in Figure 4.5.a). As can be observed, the anodic film formed after anodizing at 20 V shows a more amorphous structure with α-Ti peaks mostly. In contrast, when the voltage increases to 120 V, crystalline peaks of anatase phase (Ti_2O) were detected, in agreement with other reports [14].

The crystalline transformation is closely related to the dielectric rupture of the film during anodizing process and, at low voltages, the anodic oxide film is amorphous. By increasing the voltage, the film structure changes from amorphous to crystalline. Peaks of α-Ti, Ti_2O_3 and TiO were also detected at 120 V. These phases have been reported by others works, in which phosphoric acid has been used [13,15]. According to literature, in the synthesis of TiO_2 films by various methods in pure titanium, the initial crystalline TiO_2 phase formed is generally anatase [16,17]. Despite this, the oxide formation is different for Ti6Al4V, in which anatase become the dominant phase. The reason for the growth of anatase in Ti6Al4V is not yet understood by literature, but it is unlikely that this is due to the presence of the alloying elements V and Al. Actually, aluminum tends to favor the rutile phase by creation of oxygen, and vanadium rather promotes the transformation of anatase to rutile in bulk titania, lowering the transition temperature [18].

In anodizing process, the surface of a metal is transformed into an oxide layer, through the passage of electric current, in which this layer formed anodically is allowed to dye in many different shades. In addition to the phenomenon of light interference, the coloring may be related to the crystalline structure of the film. The morphology of the surface and the thickness of the oxide layer depend on the method applied for the formation of the oxide layer and the relation between color and thickness of the oxide depends on the anodization process and the nature of the electrolyte [19].

The morphology of the anodic films produced by using 20 and 120 V during 1 minute is presented in Figure 4.6, where two regions are presented, a non-anodized region and an anodized region of the same sample. The α- and β-Ti phase can be distinguished on the surface of both conditions presented. According to literature, the anodic films are composed by two layers: the inner Ti-oxide, which is composed by anatase crystals and the outer Ti-oxide formed at the film/electrolyte interface, which is composed by an amorphous oxide. During the anodization of Ti, an amorphous-crystalline transition is involved and at relative low voltages, this transition might not be completed, resulting in an amorphous and thinner oxide layer [20]. As can be observed (Figure 4.6b), the anodic oxide film formed is more pronounced at the 120 V condition, since the thickness is higher when compared to 20 V (Figure 4.6a). In addition, the film seems to be uniform and continuous in the case of 20 V and some defects (porous/impurities) in the 120 V condition (Figure 4.6a1 and 4.6b1) is presented. Similar morphology was already obtained by other works, wherein phosphoric acid (H_3PO_4) in low concentration has been used [11,21]. The anodizing curve (current vs time) of each condition is also presented in Figure 4.6.

a)

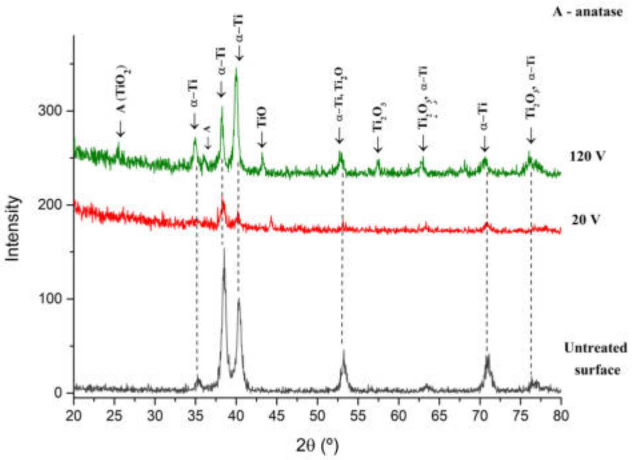

b)

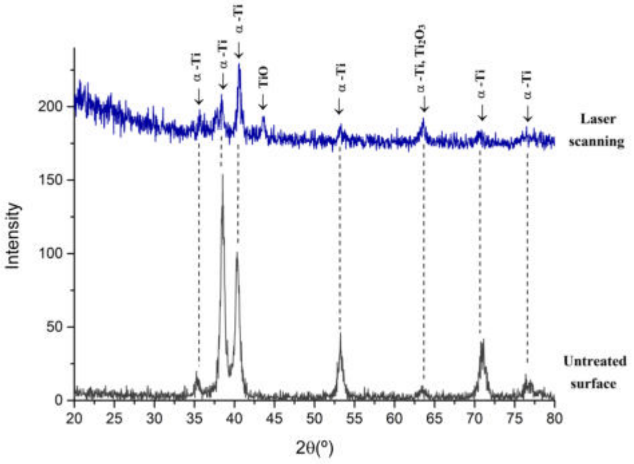

Figure 4.5.XRD patterns of untreated Ti6Al4V alloy and samples with oxidized surface by: (a) anodization at 20 V and 120 V during 1 minute and (b) laser scanning.

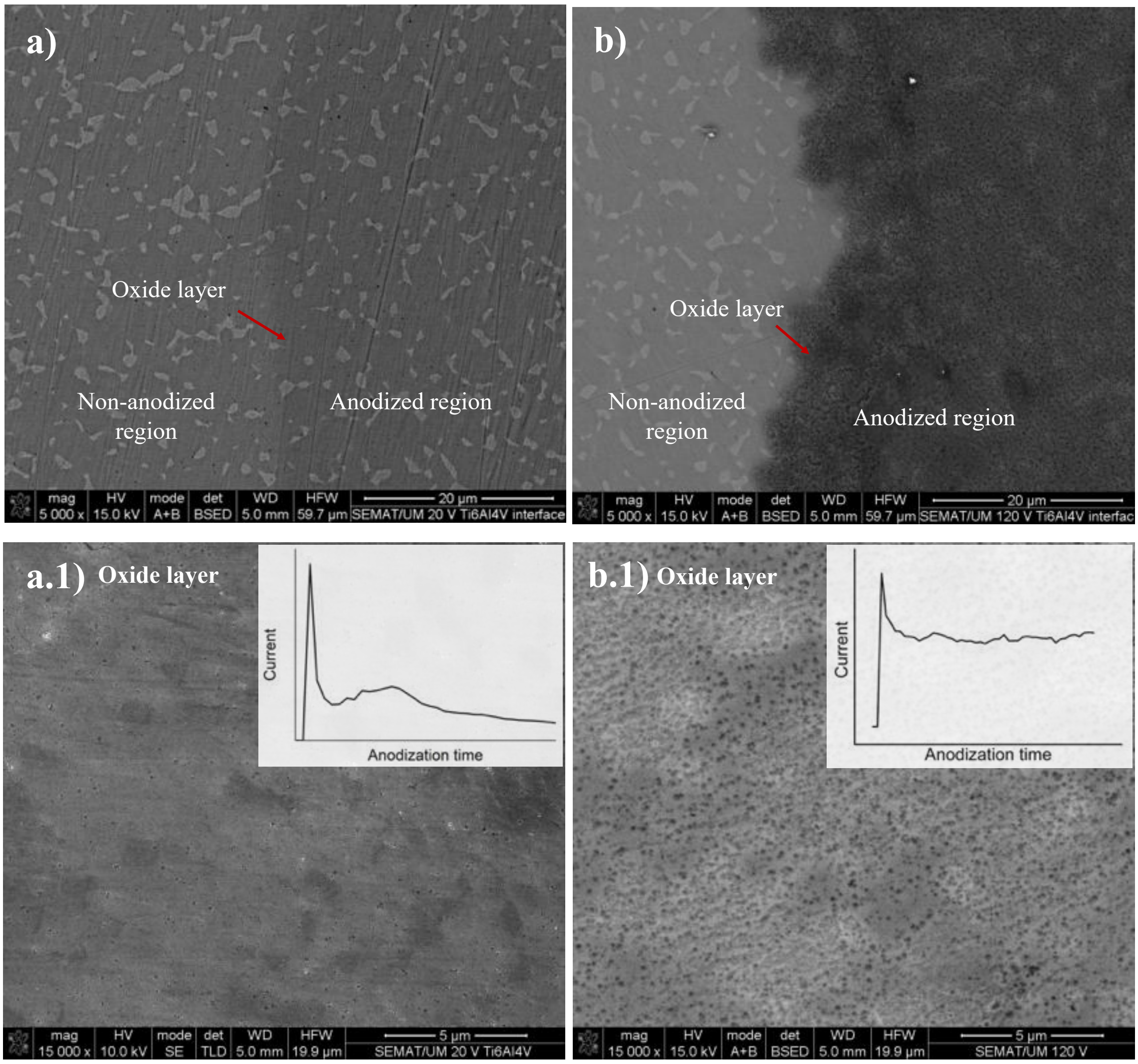

Figure 4.6 SEM micrographs of Ti6Al4V surface after anodizing at 20 V (a) and 120 V (b). The interface between two regions (anodized and non-anodized) is presented. Images a.1) and b.1) show the zone of the oxide layer and their correspondents anodization curves for 20 and 120 V, respectively.

In order to determine the thickness of each anodizing condition, atomic force microscope was performed. AFM images are presented in Figure 4.7. The thickness was measured after obtaining an AFM image from the region of the interface between non-anodized surface (A) and TiO_2 film (B). A line was traced from the region A to B and the thickness of the film is a result of the difference in the height of these regions. The film produced with the lowest voltage (20 V) resulted in a thickness around 20 nm and the film produced by using 120 V presented a thickness of 152 nm. These values of thickness are in agreement with some works in literature [11,12].

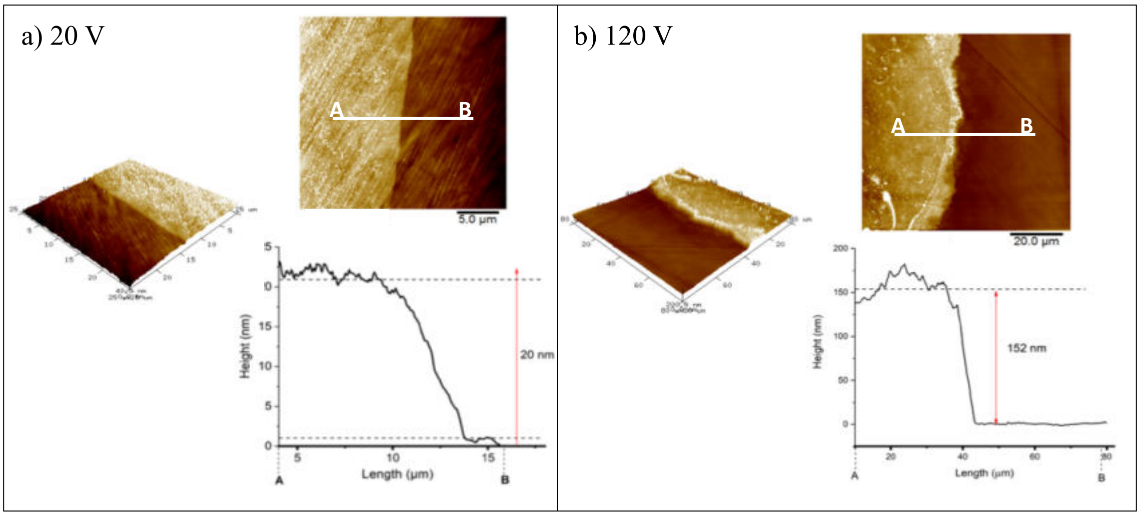

Figure 4.7. AFM images of anodic titanium oxide on Ti6Al4V surface: a) 20 V and b) 120 V.

Oxidation by laser

During the laser scanning, the samples are superficially melted, by laser beam, leading to oxygen diffusion through the molten material and, thus, to its surface oxidation. The XRD diffractograms of untreated Ti6Al4V and the oxidized surfaces after laser scanning are shown in Figure 4.5b. The peaks presented in the XRD diffractograms reveal the presence of α-Ti, TiO and Ti_2O_3 phases, being α-Ti the main phase formed [22–24]. No peaks of TiO_2 (anatase/rutile) are visible. These sub-stoichiometric phases formation has been shown in other studies, in which titanium alloy surface was oxidized by using laser [22,25]. The formation of α-Ti is discussed in literature [26], which consists in an interstitial solid solution Ti(O) that forms a thick oxygen-rich metallic layer under the main oxide layer on titanium alloy surface [27]. The thickness of the Ti-oxide layer can be seen in the SEM images shown in Figure 4.8. The Ti-oxide layer has a thickness around 916 nm and the layer cross-section show a dense and rough oxide film without pores on the surface.

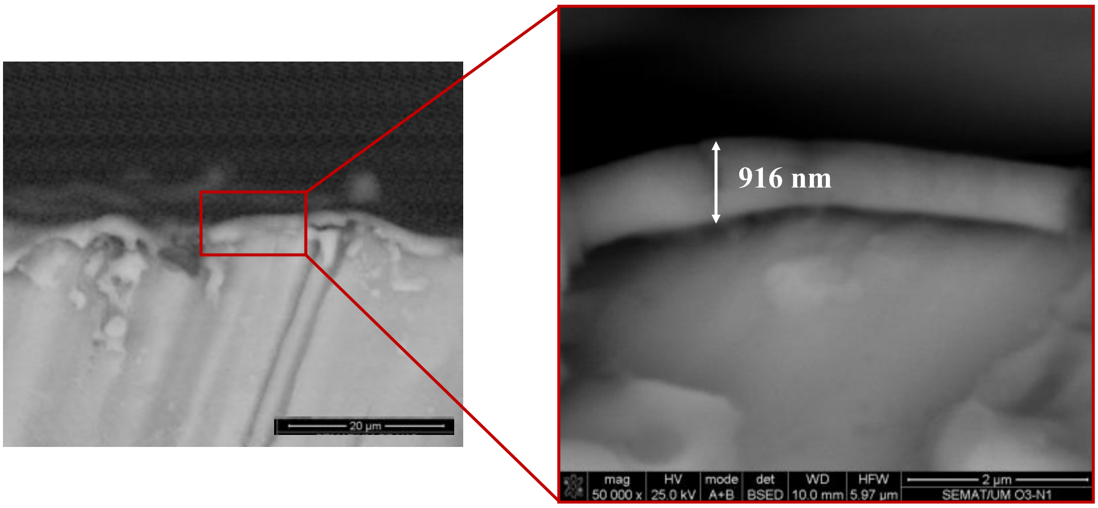

Figure 4.8. Cross-section micrograph of Ti6Al4V surface oxidized by laser micro-scanning.

4.3.3 Silver powder sintering - Wire printing

After micro-cavity creation and insulation layer production on the micro-cavity, silver powder was deposited and accommodated into the cavities. Then, silver powder was sintered by using two methodologies, such as hot-pressing and laser sintering. Figure 9 presents SEM images of the silver wires after sintering, in which Figure 9 a) corresponds to the wire sintered by laser at average power of 4 W and Figure 9 b) is the wire after sintering by hot-pressing. As can be observed the silver powder grains were apparently melted and spread to completely merge together with neighboring grains in both sintering conditions. However, the wire sintered by laser presents more imperfections on the surface. The contraction of the silver powder after sintering is more evident in this condition.

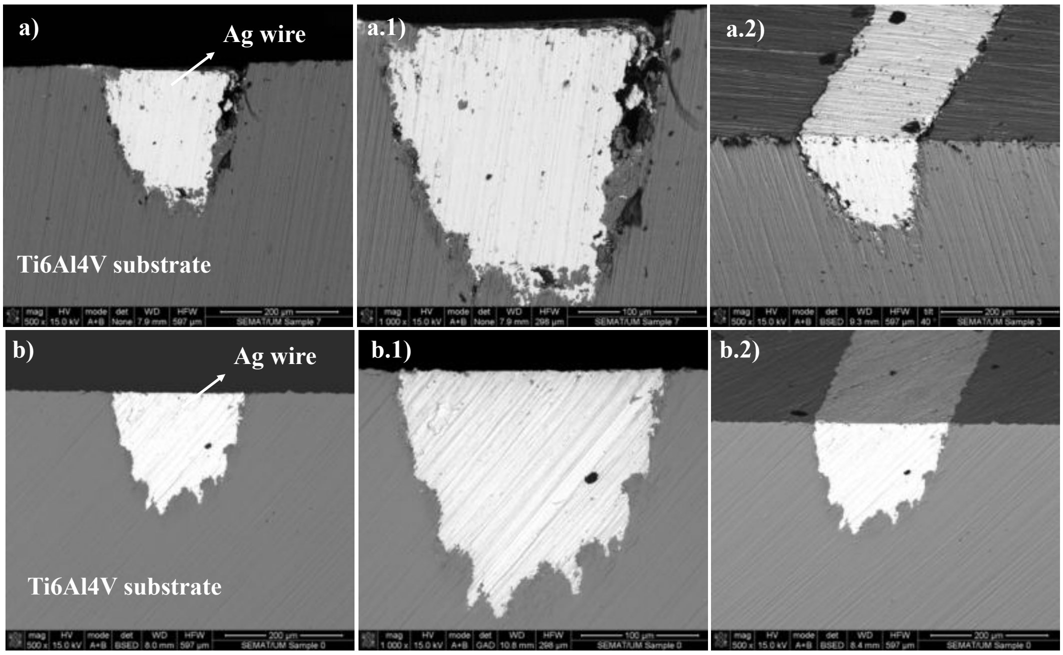

Figure 4.9 Silver wires printed on Ti6Al4V through sintering of the powder by: a) Laser and b) Hot-pressing.

In laser sintering, when the laser beam irradiates the powder surface, it absorbs the light energy and the temperature increases, giving raise to necking, grain growth and partial or fully melting in some cases, and also eventually densification [28]. Powder melting happens when the temperature reaches the material melting temperature and the dimension of molten pool will depends to the average applied energy per volume, which can be controlled through laser power and scanning speed [29]. Figure 4.10 shows the process principle of laser sintering. Compared to heating with furnace, the laser sintering provides the advantage of localized energy deposition, in which the powder is selectively irradiated and locally sintered, while the non-irradiated part of the laser stays unconsolidated [30], as occurred in our case. In Figure 4.10 it is possible to see in the extended SEM micrograph some region with non-consolidated particles. The main issue about laser sintering is related to a very steep temperature gradient that is generated due to the fast heating and cooling rate during the process. The temperature gradient induced surface tension in the molten pool can lead to convective motions (Marangoni effect) and also induce high internal stresses [31]. As can be seen in Figure 10, when the laser irradiates the top surface, the expansion of the heated layer is restricted by the surrounding area, which generates a compressive stress on the top surface. In contrast, the extent to which the laser moves away, the contraction of the top layer is restricted by the surrounding area, leading to a tensile residual stress on the top surface. This residual stress will accumulate during the laser scan, which can result in delamination and cracks formation [29]. As can be seen on Figure 4.10, there are some deficiency of molten material on the surface as a result of stress concentration by laser process. This issue has already mentioned by other works [32].

As regards hot-pressing system, a combination of pressure and temperature is responsible for a particular density at a lower temperature than would be require for sintering alone and at lower pressure. The effect of the lower temperature is that the grain growth can be avoided [33]. The sintering mechanism consists in, firstly, particles in contact and necks formation; the necks grow, and open porosity starts to decrease. Finally, necks become quite large, pores spheroidize and all open porosity disappears, the densification occurs [34]. The great advantage of sintering by HP is that there is time available for all sintering mechanisms to occur, unlike the process by LS.

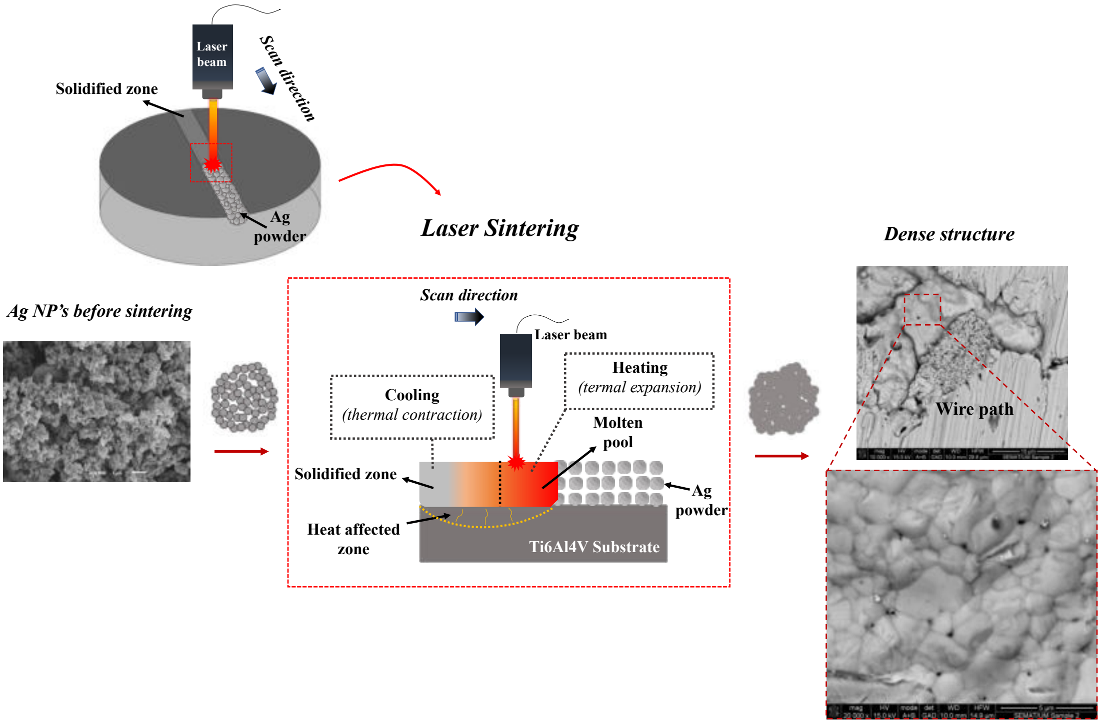

Figure 4.10 Schematic description of laser sintering of the silver wire on the Ti6Al4V substrate.

4.3.4 Electrical measurements of printed wires

In order to evaluate the electrical insulation capacity of the oxide layer formed by both laser texture and anodizing on titanium alloy surface, electrical measurements were performed. For this purpose, the four-point probe method has been used by applying an electrical current and measuring the voltage resultant. The setup of the measurement is shown in Figure 4.11 jointly to a *VxI* curves of four conditions studied, which shows the range of electrical current applied.

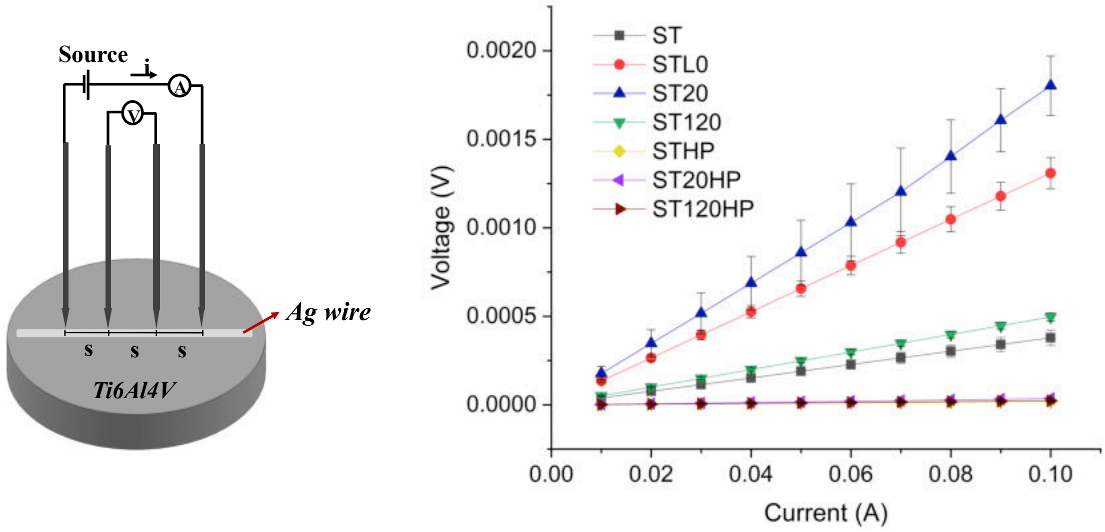

Figure 4.11 Arrangement for resistivity measurements by using four-probe method and VxI curves of the conditions studied. The letter s represents the distance between the probes, which must be known.

Thus, assuming a uniform oxide layer thickness, the resistivity (ρ) of the silver wire can be calculated through V x I curves by using Eq. 1. The results of electrical resistance aree presented in Table 4.2 and the electrical resistivity values of the Ti6Al4V titanium alloy and silver according to literature are presented in Table 4.3.

Table 4.2 Electrical resistance values calculated for each condition.

Sample	**R (Ω)**
ST	0.0038
STLO	0.0131
STA20	0.0179
STA120	0.0049
STHP	0.0008
ST20HP	0.0004
ST120HP	0.0003
Ti6Al4V substrate	**0.0003**
Wire in ZrO2 substrate	**0.0135**

Several works in literature have reported the calculation of resistivity in cases of multilayers film, but they are composed by oxide-metal-oxide multilayer, in which the resistance of the multilayer is approximately equal to the parallel resistance of the metal and oxide layers. Since the conductivity of the metal layer is about 100 times higher than that of oxide layer, the conductivity of the multilayer is mainly supplied by the metal layer present [35–37]. However, studies concerning the resistivity calculation of metal on metal substrate separated by a thin oxide layer are scarce and there is no specific equation for that. As already known in literature, TiO_2 is electrically insulating with an extremely high resistivity above 10^6 Ω.m, but the suboxidized TiO_2 with an excess of titanium is an n type semiconductor, indicating the defect disorder and O/Ti stoichiometric play an important role in the electrical properties of TiO_x [38].

Table 4.3 Electrical resistivity of the materials according to literature.

Material	**Electrical resistivity (Ω.m)**
Ti6Al4V	1.71×10^{-6} [39]
Silver	1.60×10^{-8} [40]

According to the results, there are two factors that may influence the resistance values, namely: the wire quality, and the insulator layer efficiency. The wire quality includes the impurities and imperfections which is a result of the sintering process and may further decrease the mean free path of electrons. As regard the insulator layer, its efficiency will depend not only its thickness, but also its morphology and structure formed.

The electrical resistance measured in the samples has two opposites trends depending on the sintering method: it slightly decreases as the insulating increases in HP group and it increases in LS approach. Nonetheless, the variation between the resistance values of the HP group and the resistance measured on Ti6Al4V substrate is not relevant, being in the same order of magnitude. This suggests that when hot-pressing is used, although the densification is satisfactory, the interface between the silver wire and titanium alloy substrate is damaged, decreasing the contact resistance, which will force the current to flow through the substrate rather than the wire.

On the other hand, by analyzing the LS group, the values of resistance increase as the insulation layer is improved, from ST to STLO and STA20, except the sample STA120, in which the resistance value decreases again. This behavior can be justified through the oxide layer morphology formed at 120 V, which can be seen in Figure 4.6a.2 as well as in anodizing curve. The oxide layer at 120 V presents a great porous distribution in contrast with the oxide at 20 V, although in this condition the oxide thickness is considerably lower. In addition, the current-time behavior measured during the potentiostatic preparation of oxide layer reflects this overall mechanism (Figure 4.6a.1 and a.2), in which for 20 V condition, in the first stage the current increases due to the oxide layer formation and then decreases rapidly reaching zero, as a consequence of increasing resistance of the rapidly growing oxide layer. In contrast, the anodizing curve for 120 V condition shows that after the oxide formation the current decreases but not in total, keeping constant until the end of the process [41–43].

In terms of laser sintering process, a larger grains size resultant may have influenced the electrical resistivity of the wire. In the case of LS, the energy is deposited in a very fine surface layer of the single grains that will melt partially. Then, neighboring grains will join by the liquid surface layer that re-solidifies very quickly and consequently, the grains are frozen. As a consequence of that a low grain boundary is generated, favoring the grains connectivity, affecting positively the current flow [44–46].

Taking into account the resistance measured on the wire deposited and sintered by laser in zirconia substrate, in which all the current flows to the metallic part (wire), a value of resistivity can be calculated through Eq. 1, presented in Section 2. In this case, according to Equation, *A* is the cross-section area of the wire, L is the probe distance (0.001 m) and R is the resistance of the wire. Thus, a value of 4.86 x 10^{-7} Ω.m was found, which is still far from the known value for silver (1.6 x 10^{-8} Ω.m) [40].

To verify the experimentally calculated value for the silver wire resistivity, numerical simulations were performed using the COMSOL Multiphysics software and using the main parameters shown in Table 4.4. The electric currents from the AC/DC model was used for the numerical simulations. Four geometric points (P1, P2, P3, and P4) were place on top of the silver wire with 1 mm distance between each other, in order to simulate the four points probes (Figure 4.12a). The silver wire is perfectly isolated from the substrate. At the furthest points (P1 and P4) a current source of 0.2 A and -0.2 A was applied. A wide range of resistivity values were attributed to the silver wire and the voltage output for each resistivity was measured between P2 and P3.

The electric potential value calculated experimentally for the silver wire with a current source of 0.2 A was 0.27 mV. An electric potential value of 0.277 mV between P2 and P3 can be obtained from the simulation for a silver resistivity of 5x10^{-7} Ω.m, which is in good agreements with the expected theoretical value. Figure 4.12b shows the distribution of the electric potential along the wire for a silver resistivity of 5x10^{-7} Ω.m.

Table 4.4 Numerical simulation parameters

Module	**AC/DC**
Method	Finite Element Method (FEM)
Equations Solved	$J = \sigma E + J_e$ $-\nabla(\sigma \nabla V - J_e) = Q_j$ where σ is the electrical conductivity (SI units: S/m), J_e is an externally generated current density (SI units: A/m^2) and Q_j is a current source (SI units: A)
Study	Stationary
Computational Mesh	3D mesh with triangular and tetrahedral elements (COMSOL physics controlled mesh)
Refinement of the Computational Mesh	Extremely fine (with 0.16 mm as maximum element size and 1.6 µm as minimum element size)
Convergence Criteria	Stationary iterative solver Multigrid with a relative tolerance of 1x10^{-7}.
Boundary Conditions	All surfaces were electrically isolated. At the furthest points (P1 and P4) a current source of 0.2 A and -0.2 A was applied.
Output Results	Electrical potential measured between the geometric points P2 and P3 for a wide range of resistivity values for the silver wire.

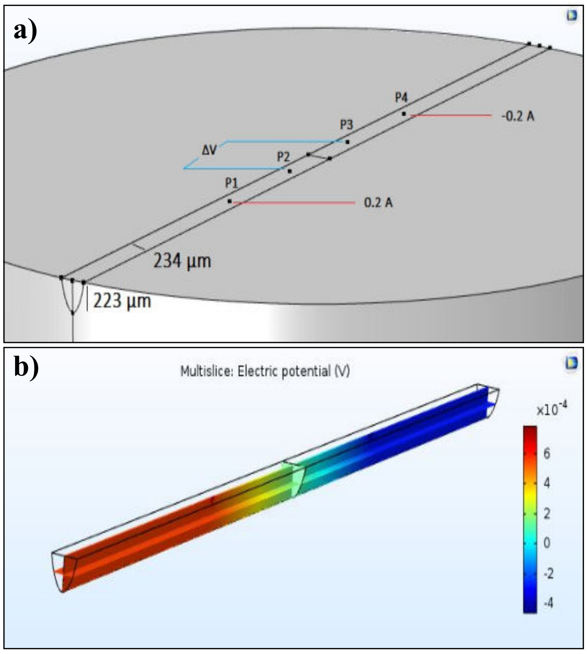

Figure 4.12 (a) Draft of the geometric configuration of the simulation conditions, (b) Distribution of the electric potential along the silver wire.

4.4 Conclusions

Print of micro communication systems in titanium alloy (Ti-6Al-4V) surface assisted by laser is presented in this work. In this context, micro-cavities were successfully produced by laser scanning and silver powder has been consolidated into the cavities, forming micro-wires. Thin oxide layers by different approaches have been produced and tested regarding their insulation performance, in order to minimize the loss of electrical current to the substrate. In summary, electrical measurements showed that both methods used to oxidize the titanium alloy surface showed great insulation capacity, since the resistance values decrease from ST to STLO and ST20 conditions. This behavior can be attributed to a greater wire contribution for the current flow. In addition, the results showed that although the condition ST120 presents an oxide layer thicker compared to ST20, its porous structure compromises its insulation performance. As regards HP groups, although HP sintering presented a satisfactory densification of the wire, the resistance measured values indicate a weak contribution of the wire to the current flow, due to the low contact resistance in the interface between the materials, as a result of the pressure and temperature used in this method. In order to know the electrical resistivity of the wire sintered by laser, a zirconia substrate was used to receive the wire. The calculated value for the wire resistivity was 4.86 x 10^{-7} Ω.m, which is in good agreement with the value from the simulation performed. This work presented a hybrid approach for printing micro-wires in metal substrate through laser technology as also showed different methods to insulate the wire from the substrate, allowing its great efficiency in the current flow.

Conflicts of interest

The authors have no conflict of interest to declare.

Acknowledgement

This work has been supported by FCT (Fundação para a Ciência e Tecnologia -Portugal) in the scope of the projects UID/EEA/04436/2019 and NORTE-01-0145-FEDER-000018-HAMaBICo and Add.Additive_Manufacturing to Portuguese Industry_POCI-01-0247-FEDER-024533. Thank the CNPq (205791/2014-0) and CAPES for the financial support.

References

[1] V.Y. Zadorozhnyy, E. V. Kaevitser, A.N. Kopylov, Y. V. Borisova, V. V. Sudarchikov, R.S. Khasenova, M. V. Gorshenkov, M.Y. Zadorozhnyy, S.D. Kaloshkin, Synthesis of the hydroxyapatite coatings on the Ti substrates by mechanical alloying, Surf. Coatings Technol. 281 (2015) 157–163. doi:10.1016/j.surfcoat.2015.09.056.

[2] E. Mohseni, E. Zalnezhad, A.R. Bushroa, Comparative investigation on the adhesion of hydroxyapatite coating on Ti-6Al-4V implant: A review paper, Int. J. Adhes. Adhes. 48 (2014) 238–257. doi:10.1016/j.ijadhadh.2013.09.030.

[3] L. Tiainen, P. Abreu, M. Buciumeanu, F. Silva, M. Gasik, Journal of the Mechanical Behavior of Biomedical Materials Novel laser surface texturing for improved primary stability of titanium implants, (2019).

[4] G. Miranda, F. Sousa, M.M. Costa, F. Bartolomeu, F.S. Silva, O. Carvalho, Surface design using laser technology for Ti6Al4V-hydroxyapatite implants, Opt. Laser Technol. 109 (2019) 488–495. doi:10.1016/j.optlastec.2018.08.034.

[5] D. Faria, C.S. Abreu, M. Buciumeanu, N. Dourado, O. Carvalho, F.S. Silva, G. Miranda, Ti6Al4V laser surface preparation and functionalization using hydroxyapatite for biomedical applications, J. Biomed. Mater. Res. - Part B Appl. Biomater. 106 (2018) 1534–1545. doi:10.1002/jbm.b.33964.

[6] J. Andreu-Perez, D.R. Leff, H.M.D. Ip, G.Z. Yang, From Wearable Sensors to Smart Implants-Toward Pervasive and Personalized Healthcare, IEEE Trans. Biomed. Eng. 62 (2015) 2750–2762. doi:10.1109/TBME.2015.2422751.

[7] E.H. Ledet, B. Liddle, K. Kradinova, S. Harper, Outcomes: a Review, (2018) 41–51. doi:10.2147/IEH.S133518.

[8] C. O'Connor, A. Kiourti, Wireless Sensors for Smart Orthopedic Implants, J. Bio- Tribo-Corrosion. 3 (2017) 1–8. doi:10.1007/s40735-017-0078-z.

[9] L.A. Korduba, M.B.M. Grabowsky, R.L. Uhl, M.M. Hella, E.H. Ledet, Radio Frequency Identification as a Testbed for Integration of Low Frequency Radio Frequency Sensors Into Orthopedic Implants, J. Med. Device. 7 (2013) 011008. doi:10.1115/1.4023499.

[10] C.G. Moura, O. Carvalho, L.M. V Gonçalves, M.F. Cerqueira, R. Nascimento, F. Silva, Laser surface texturing of Ti-6Al-4V by nanosecond laser: Surface characterization, Ti-oxide layer analysis and its electrical insulation performance, Materials Science & Engineering C. 104 (2019) 109901. https://doi.org/10.1016/j.msec.2019.109901.

[11] N.K. Kuromoto, R.A. Simão, G.A. Soares, Titanium oxide films produced on commercially pure titanium by anodic oxidation with different voltages, Mater. Charact. 58 (2007) 114–121. doi:10.1016/j.matchar.2006.03.020.

[12] A. Karambakhsh, A. Afshar, P. Malekinejad, Corrosion resistance and color properties of anodized Ti-6Al-4V, J. Mater. Eng. Perform. 21 (2012) 121–127. doi:10.1007/s11665-010-9791-1.

[13] W. Asumpinwong, K. Saengkiettiyut, V. Srimaneepong, Different constant voltages of anodization on the corrosion behavior of Ti-6Al-4V alloy, Chiang Mai J. Sci. 42 (2015) 239–248.

[14] Y.T. Sul, C.B. Johansson, Y. Jeong, K. Roser, A. Wennerberg, T. Albrektsson, Oxidized implants and their influence on the bone response, J. Mater. Sci. Mater. Med. 12 (2001) 1025–1031. dx.doi.org/10.1023/A:1012837905910.

[15] R. Narayanan, S.K. Seshadri, Phosphoric acid anodization of Ti-6Al-4V - Structural and corrosion aspects, Corros. Sci. 49 (2007) 542–558. doi:10.1016/j.corsci.2006.06.021.

[16] K. Okada, N. Yamamoto, Y. Kameshima, A. Yasumori, K.J.D. MacKenzie, Effect of Silica Additive on the Anatase-to-Rutile Phase Transition, J. Am. Ceram. Soc. 84 (2004) 1591–1596. doi:10.1111/j.1151-2916.2001.tb00882.x.

[17] H. Shin, H.S. Jung, K.S. Hong, J.K. Lee, Crystal phase evolution of TiO2 nanoparticles with reaction time in acidic solutions studied via freeze-drying method, J. Solid State Chem. 178 (2005) 15–21. doi:10.1016/j.jssc.2004.09.035.

[18] M. Rinner, J. Gerlach, W. Ensinger, Formation of titanium oxide films on titanium and Ti6A14V by O 2 -plasma immersion ion implantation, Surf. Coatings Technol. 132 (2000) 111–116. doi:10.1016/S0257-8972(00)00712-X.

[19] T.A. Young-Taeg Sul , Carina B. Johansson, Yongsoo Jeong, The electrochemical oxide growth behaviour on titanium in acid and alkaline electrolytes, Med. Eng. Phys. 23 (2001) 329–346. doi:10.1021/acs.jpca.7b04442.

[20] H. Habazaki, K. Shimizu, S. Nagata, P. Skeldon, G.E. Thompson, G.C. Wood, Ionic transport in amorphous anodic titania stabilised by incorporation of silicon species, Corros. Sci. 44 (2002) 1047–1055. doi:10.1016/S0010-938X(01)00111-1.

[21] Z.J. Liu, X. Zhong, J. Walton, G.E. Thompson, Anodic Film Growth of Titanium Oxide Using the 3-Electrode Electrochemical Technique : Effects of Oxygen Evolution and Morphological Characterizations, 163 (2016) 75–82. doi:10.1149/2.0181603jes.

[22] A. Pérez Del Pino, P. Serra, J.L. Morenza, Coloring of titanium by pulsed laser processing in air, Thin Solid Films. 415 (2002) 201–205. doi:10.1016/S0040-6090(02)00632-6.

[23] A. Pérez Del Pino, P. Serra, J.L. Morenza, Oxidation of titanium through Nd:YAG laser irradiation, Appl. Surf. Sci. 197–198 (2002) 887–890. doi:10.1016/S0169-4332(02)00447-6.

[24] A.J. Antończak, Ł. Skowroński, M. Trzcinski, V. V. Kinzhybalo, Ł.K. Łazarek, K.M. Abramski, Laser-induced oxidation of titanium substrate: Analysis of the physicochemical structure of the surface and sub-surface layers, Appl. Surf. Sci. 325 (2015) 217–226. doi:10.1016/j.apsusc.2014.11.062.

[25] A. Pérez del Pino, J.M. Fernández-Pradas, P. Serra, J.L. Morenza, Coloring of titanium through laser oxidation: Comparative study with anodizing, Surf. Coatings Technol. 187 (2004) 106–112. doi:10.1016/j.surfcoat.2004.02.001.

[26] G.Z. Chen, D.J. Fray, T.W. Farthing, Cathodic deoxygenation of the alpha case on titanium and alloys in molten calcium chloride, Metall. Mater. Trans. B Process Metall. Mater. Process. Sci. 32 (2001) 1041–1052. doi:10.1007/s11663-001-0093-8.

[27] H. Dong, X.Y. Li, Oxygen boost diffusion for the deep-case hardening of titanium alloys, Mater. Sci. Eng. A. 280 (2000) 303–310. doi:10.1016/S0921-5093(99)00697-8.

[28] J.P. Kruth, P. Mercelis, J. Van Vaerenbergh, L. Froyen, M. Rombouts, Binding mechanisms in selective laser sintering and selective laser melting, 2005. doi:10.1108/13552540510573365.

[29] C.H. Fu, Y.B. Guo, Three -Dimensional Temperature Gradient Mechanism in Sele ctive Laser Meltin g of Ti-6Al-4V, 136 (2014) 1–8. doi:10.1115/1.4028539.

[30] P. Fischer, V. Romano, A. Blatter, H.P. Weber, Highly precise pulsed selective laser sintering of metallic powders Nd : YAG, 55 (2005) 48–55. doi:10.1002/lapl.200410118.

[31] T.A.M. Bennett TD, Krajnovich DJ, Grigoropoulos CP, Baumgart PP, Mechanism in Pulsed Laser Texturing of Magnetic Disk Substrates, ASME. J. Heat Transf. 119 (1997) 589–596. doi:10.1115/1.2824146.

[32] V.S. Sufiiarov, A.A. Popovich, E. V Borisov, I.A. Polozov, D. V Masaylo, ScienceDirect The effect of layer thickness at selective laser melting, 174 (2017) 126–134. doi:10.1016/j.proeng.2017.01.179.

[33] R.M. and M.C.F. M.Basaran, T.Z.Kattamis, M.Basaran, T.Z.Kattamis, R.Mehrabian and M.C.Flemings: Metall. Trans., 1973, vol. 4, pp. 2429-34., Met. Trans. 4 (1973) 2429–34.

[34] H. V Atkinson, S. Davies, Fundamental Aspects of Hot Isostatic Pressing : An Overview, m (2000).

[35] J.-J.C. Yi-Cheng Lin, Kun-Hsin Lu, Characterization the electrical and optical properties of AZO/AgPd/AZO multilayer film using RF magnetron sputtering, Chinese J. Phys. (2016) 1–9. doi:10.1016/j.cjph.2016.06.007.

[36] B.L. Nai-fei Ren, Li-jing Huang, Ming Zhou, Introduction of Ag nanoparticles and AZO layer to prepare AZO/Ag/FTO trilayer films with high overall photoelectric properties, Ceram. Int. (2014) 1–8. doi:10.1016/j.ceramint.2014.01.087.

[37] F.-C.T. Tien-Chai Lin, We-Chang Huang, The structural and electro-optical characteristics of AZO/Cr:Cu/AZO transparent conductive film, Thin Solid Films. 11 (2015) 1–6. doi:10.1016/j.tsf.2015.06.011.

[38] J. Nowotny, T. Bak, M.K. Nowotny, L.R. Sheppard, Titanium dioxide for solar-hydrogen II . Defect chemistry˚, 32 (2007) 2630–2643. doi:10.1016/j.ijhydene.2006.09.005.

[39] E.G. L. BOLZONI, E.M. RUIZ-NAVAS, Flexural properties, thermal conductivity and electrical resistivityof prealloyed and master alloy addition powder metallurgy Ti–6Al–4V, Mater. Des. 52 (2013) 888–895. doi:10.1016/j.matdes.2013.06036.

[40] R.A.Matula, Electrical resistivity of cooper, gold, palladium, and silver, J. Phys. Chem. Ref. Data. (2009). doi:https://doi.org/10.1063/1.555614.

[41] A. Ghicov, P. Schmuki, Self-ordering electrochemistry : a review on growth and functionality of TiO 2 nanotubes and other self-aligned MO x structures, (2009) 2791–2808. doi:10.1039/b822726h.

[42] T. Ohgai, Magnetoresistance of Nanowires Electrodeposited into Anodized Aluminum Oxide Nanocavities, in: 2012. doi:http://dx.doi.org/10.5772/3367.

[43] H. Yoo, M. Kim, Y. Kim, K. Lee, Electrodes for (Photo) Electrochemical Reactions, (2018) 1–25. doi:10.3390/catal8110555.

[44] D.M. A. Yildiz, S.B. Lisesivdin, M. Kasap, Non-adiabatic small polaron hopping conduction in Nb-doped TiO2 thin film, Phys. B. (2009) 10–14. doi:10.1016/j.physb.2008.12.034.

[45] D.M. A. Yildiz, S.B. Lisesivdin, M. Kasap, Electrical properties of TiO2, J. Non. Cryst. Solids. (2008) 5–9. doi:10.1016/j.

[46] H. Zhang, G. Lee, C. Gong, L. Colombo, K. Cho, Grain Boundary Effect on Electrical Transport Properties of Graphene, (2014).

Chapter 5 - A novel approach for micro-antenna fabrication on Ti6Al4V substrate assisted by laser printing for communication systems in smart implants

Submitted to Bioelectronics and Biosensors

C. G. Moura[1]*, H. Dinis[1], O. Carvalho[1], J. Neto[1], P. Mendes[1], R. M. Nascimento[2], F.S. Silva[1]

[1]CMEMS-UMinho, University of Minho, 4800-058, Guimarães, Portugal

[2]Materials Science and Engineering Post-Graduate Program, UFRN, 59078-970 Natal, Brazil

*Corresponding author – C. G. Moura (caroline.materiais@gmail.com)

Abstract

The market of orthopedic implants is one of the biggest in medicine field and it is expected to grow significantly in the next years, mainly because of the continuously growing elderly population. Despite the technological advances, the implant-adjacent biological issues empower the implants' failures, and consequently reduce its lifetime. The development of implants with self-healing capabilities have been explored as a reliable approach to tackle the aforementioned issues. This can be accomplished through the introduction of actuators, sensors devices and antennas, which ultimately falls into the concept of smart implants. Thus, this work presents an alternative approach for printing antenna in Ti6Al4V substrate by using laser technique. The performance of the fabricated antenna was assessed through simulation and compared with an ideal condition. In both situations, the antenna presented the better results at high frequencies. Nevertheless, the defects arising from the experimental fabrication contributed in a negative manner the antenna's efficiency.

Keywords: Nd:YAG laser; smart implants; communication system; antenna; implants.

5.1 Introduction

Despite the technological advances in orthopaedic implants, the frequent occurrence of failures trigged by implant-adjacent biological issues, namely wear, loosening and misalignment, significantly reduce the implant's life cycle. At the same time, the orthopedic implants market tends to grow in the years to come as the population ages [1]. In this framework, the demand for new long-lasting implants is imperative. The development of implants with self-healing capabilities have been explored as a reliable approach to tackle the aforementioned issues. This can be accomplished through the introduction of actuators and sensors devices, which ultimately falls into the concept of smart implants.

The integration of smart components, and consequently their proper functioning, is highly dependent on the communication system, which is comprised by internal communication array of wires, antenna, and local surface areas with ability to sense and or actuate. The antenna is responsible to transmit a signal from the interior of the body to the exterior and vice versa, and hence make up the main communication cavity between the implant and the user.

In general, a combination of classical surface micromachining and self-assembly techniques, (such as evaporation and sputtering) is used to obtain micro-antennas, mostly fabricated on insulating substrates [2–5]. However, the latter methods would involve a multi-step fabrication process if applied for manufacturing antennas on implant's surface. In this regard, 3D printing is emerging as an enabling technology for a wide range of new applications, in which materials as sensors, actuators or antennas may be successively printed, giving rise to a component with smart function areas. The main advantage of 3D printing technology is the ability to fabricate components, with complex structures, in a single step process [6].

The following requirements must be met so that the antenna performs successfully when placed in the implant's surface, namely it must (i) be small and (ii) isolated from the metallic substrate. The most common approach to ensure the insulation of the antenna is to cover the substrate with a dielectric material. For this purpose, zirconia is the ideal candidate mainly due to its electrical properties. Its high permittivity and low loss-tangent values ($\varepsilon_r = 29$; tan $\delta \approx 0$) [7] allow the near fields of the antenna to concentrate in the metal-based antenna path, thus mitigating power loss [8].

With this in mind, this works present an alternative approach to print a silver-based antenna in the titanium alloy substrate, as a component of the communication system, assisted by laser technology. Although this work will focus on the printing of the antenna, as a separate step, this method will further integrate a continuous processing design, from which the implant and all other components (including the communication system) will be printed in a single step. The laser is applied as a versatile tool, whether for preparing the surface of the material in a subtractive way, by creating micro-cavities, or for print the components, in an additively way. The final design of the implant with the printed communication system is schematically presented in Figure 5.1.

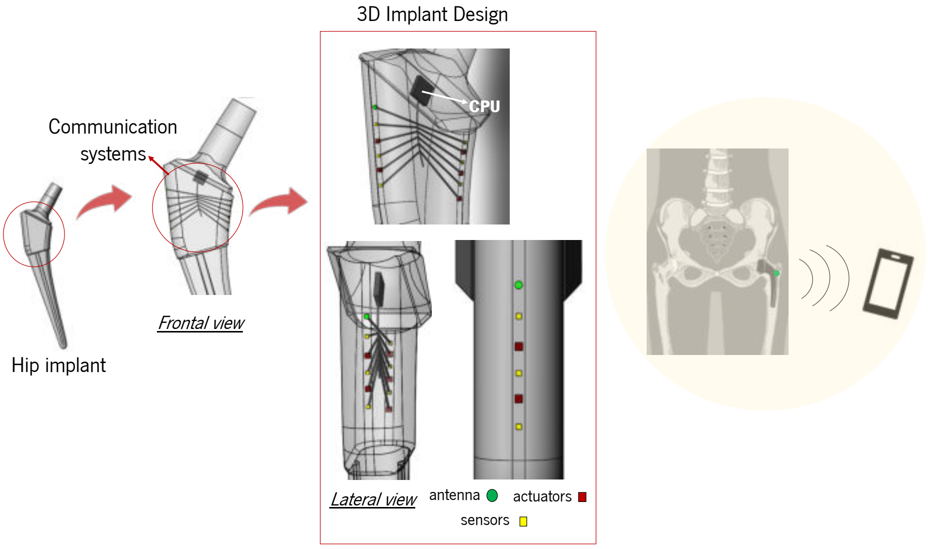

Figure 5.1 Schematically illustration of the final solution of Ti6Al4V-based implant with printed the communication system.

5.2 Experimental details

The objective of this work is the proposal of a fabrication method capable of yielding an antenna directly integrated in the metal substrate of an implant, during its fabrication, without significant modifications to its design and structure. For this, it is desired the design of a small antenna with little impact on the structure of the implant. Therefore, a wire antenna inside the substrate presents itself as a viable option that meets the aforementioned requirements. The design of such an antenna is presented in the next section of this work.

5.2.1 Proposed antenna

Bearing in mind that the preservation of the structural integrity of the substrate is of paramount importance, an antenna with a low impact on the substrate is proposed. Such antenna can be, for example, a loop antenna, and this antenna architecture will be considered in this work. To build such an antenna, it is necessary to deposit a conductive metal wire in the metal substrate and guarantee its electrical insulation from the substrate. This can be achieved by creating a small cavity in the substrate that is filled with an electrical insulator, i.e. a dielectric material, followed by the creation of a conducting wire in the insulator.

The antenna proposed in this work is presented in Figure 5.2. The dielectric material is zirconia, while the conducting metal of the antenna is silver.

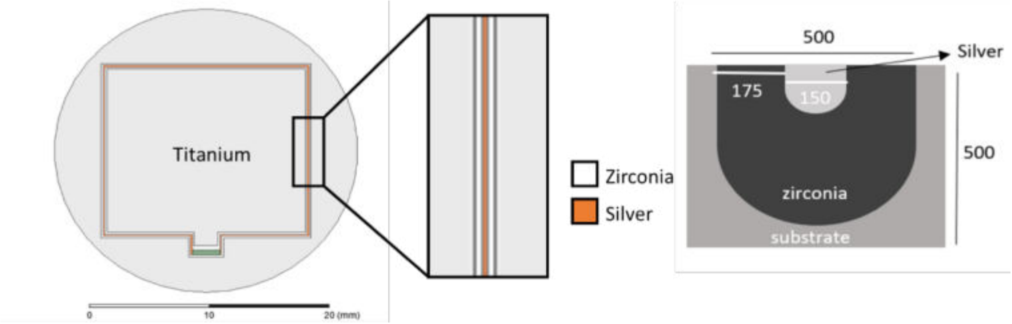

Figure 5.2 Model of the proposed antenna, where the substrate is made of titanium, the dielectric material is zirconia and the metal path is made of silver (all units in μm).

5.2.2 Simulation performance of the proposed antenna

The model of the proposed loop antenna was constructed using Ansys HFSS, and the antenna was simulated to determine its potential performance. The antenna model was also inserted inside a box with the same dielectric properties of muscle tissue, in order to mimic the implantation environment of the device, in accordance to Figure 5.3.

The antenna's return loss and impedance are presented in Figure 5.4, while its radiation pattern at 2.6 GHz and 8.4 GHz are presented in Figure 5.5.

.

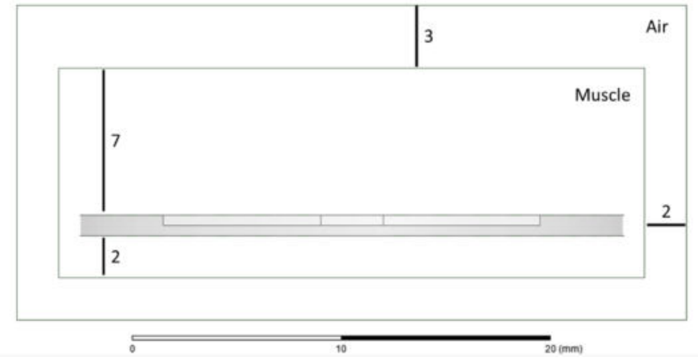

Figure 5.3 Muscle phantom placed around the model of the antenna.

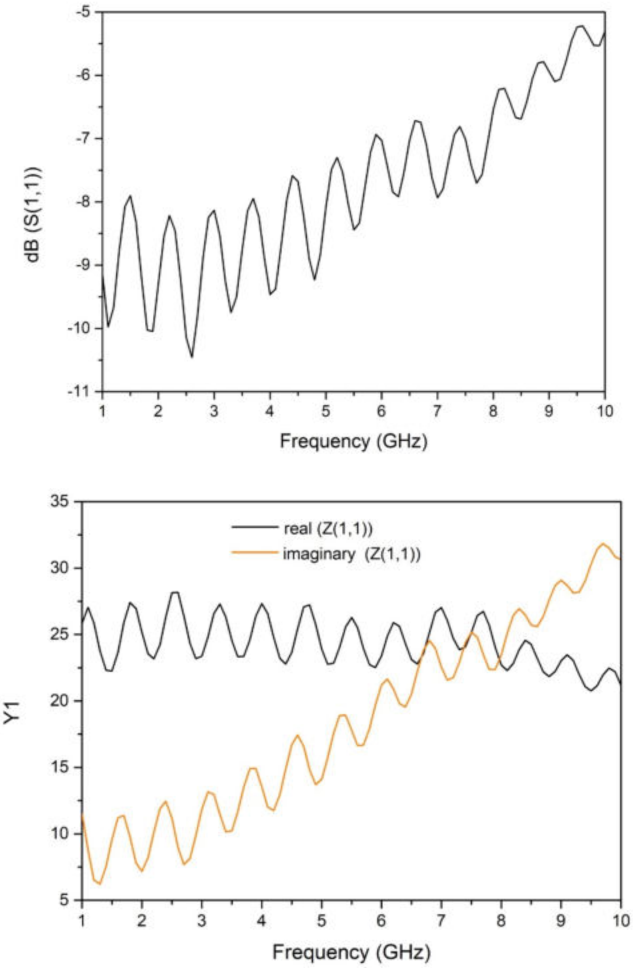

Figure 5.4 Return loss (top) and impedance (bottom) of the proposed antenna.

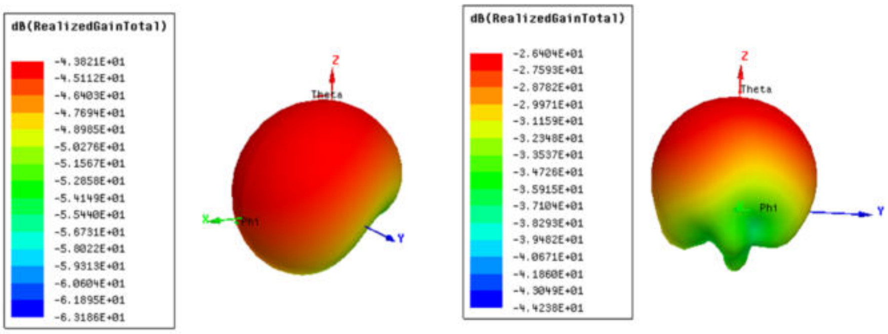

Figure 5.5 Radiation pattern of the antenna at 2.6 GHz (left) and 8.4 GHz (right).

Firstly, the return loss also presents an unusual wavy pattern, which is also observed in its impedance, leading to the conclusion that such an effect occurs due to the characteristics of the structure being simulated, and not a simulation error such as a poorly placed radiation absorption boundary.

Analysing the return loss, it is possible to conclude that the antenna operates best at lower frequencies, as the return loss is lowest in this region, as opposite to higher frequencies, where a significant part of the signal that is injected into the antenna is immediately reflected to the source. Nevertheless, when comparing the radiation patterns at 2.6 GHz and 8.4 GHz, it is possible to see that the antenna presents the highest gain at the higher frequency (-44 dB versus -26 dB). These contradictory results lead to the conclusion that, despite the fact that the antenna accepts the most power at the lower frequencies, this power is not radiated, as it is lost to the substrate through the dielectric insulator. On the other hand, at higher frequencies the dielectric material becomes thicker, electrically speaking, and is capable of better insulating the antenna from the metal substrate. Consequently, even though it doesn't accept as much power at high frequencies, the power it accepts is radiated rather than lost to the substrate. This claim is supported by the analysis of the efficiency of the antenna at each of the studied frequencies, as it increases from -44.7 dB at 2.6 GHz to -29.2 dB at 8.4 GHz, a 15 dB increase. Additional support for this conclusion comes from the analysis of the surface currents at the dielectric material, presented in Figure 5.6. As it can be seen, the current that travels through the dielectric is higher at lower frequencies, thus validating the previous claim.

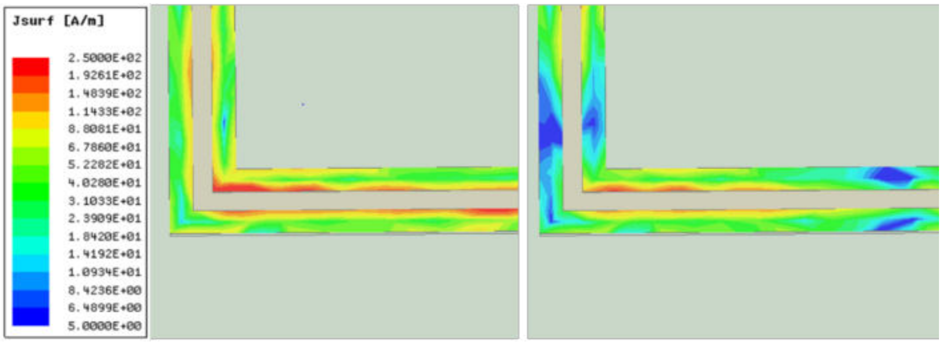

Figure 5.6 Surface currents at the dielectric at the frequencies of 2.6 GHz (left) and 8.4 GHz (right).

The next section of this paper presents a fabrication method that can be used to produce antennas such as the one designed here.

5.2.3 Antenna Fabrication

In this work, commercial Yttria-stabilized zirconia (3Y-TZP) powder with dispersion of 3 mol% Yttria (Tosoh Corporation, Japan), with particle size of 40 nm (in agglomerated size of 60 µm) was used as the dielectric material and silver powder (≥ 99% pure) with an average grain size of 230 nm, from Metalor Technologies-USA, was used as the conductor path of the antenna.

The proposed fabrication procedure consists in three steps, which are described below:

(i) Micro-cavity creation in Ti6Al4V substrate by laser;
(ii) Spray deposition and laser sintering of zirconia layer;
(iii) Deposition and laser sintering of silver powder

(i) Micro-cavity creation

In this step, a micro-cavity is created on the surface of a circular Ti6Al4V titanium alloy target with 8 mm diameter and a thickness of 2 mm for subsequently receiving the insulating layer and then, the silver powder. For this purpose, a pulsed Nd:YAG laser (OEM Plus) with a wavelength of 1064 nm and 6 W of maximum power has been used. To create the micro-cavity, a strategy consisting of overlapping lines with different wobble amplitudes and scanning speeds was performed. Thus, a sequence of 10 wobbles with different widths and scanning speed was undertaken, aiming to create a rounded shape cavity through more even distribution of laser energy. In additional, each wobble amplitude was repeated in ascending sequence, in order to achieve great depth, which resulted in 110 laser passages. Figure 5.7 shows a scheme of the laser strategy above mentioned.

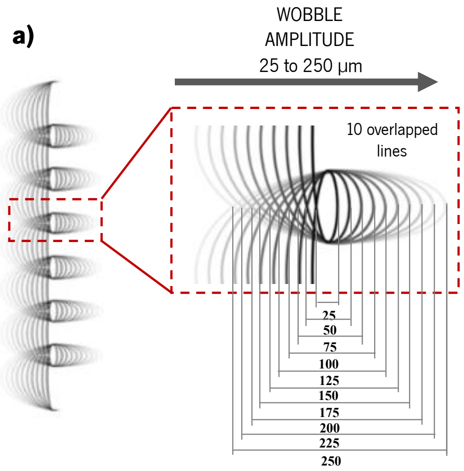

b)

Wobble amplitude (µm)	Scanning speed (mm/s)	Laser passages
25	20	2
50	18	4
75	16	6
100	14	8
125	12	10
150	10	12
175	8	14
200	6	16
225	4	18
250	2	20

Figure 5.7 Schematic illustration of the laser strategy used to create the micro-cavity on Ti6Al4V surface. (a) Scheme of the wobbles sequence. (b) Table with the parameters used in each wobble.

(ii) Zirconia layer deposition

In this step, 3Y-TZP powder was used as a dielectric material. After micro-cavity creation on titanium alloy surface, a zirconia layer was deposited on the surface by means of spray deposition process. Zirconia powder was dispersed in acetone and the suspension was sprayed using an air-brush on top of the titanium substrate. Before to spray, the solution was ultrasonically dispersed to avoid particles agglomeration. The sample was sprayed three times on the surface, in order to obtain a thick and dense layer. Then, the Ti6Al4V/ZrO_2 layer was heated by using a CO_2 laser (Bende CO_2 laser marking) with an output power of 40 Watts and a spot size of 200 µm for zirconia layer consolidation. The great advantage of this process is the possibility to sinter specific zones without compromise the substrate. Thus, a power of 20 W and a scanning speed of 200 mm/s was applied on the surface, in a frequency of 20 Hz. Figure 5.8b schematically illustrates the sintering process of zirconia layer.

(iii) Silver powder deposition and laser sintering

To print the silver-based antenna, silver powder (≥ 99% pure) with an average grain size of 230 nm, (Metalor Technologies-USA) was compacted into the cavity created in step (i) on Ti6Al4V substrate. A pressure of 8 MPa was applied to ensure the total accommodation of the powder. Then, a Nd:YAG laser (Sisma - 1064 nm of wavelength) with a spot size of 0.2 µm and 100 J of maximum energy has been used to sinter the silver powder and thus, generate conductor path of antenna. An energy of 10 J was used in the sintering process. In this last step, a support Figure 2c illustrates this process. Each step aforementioned is schematically illustrated in Figure 5.8.

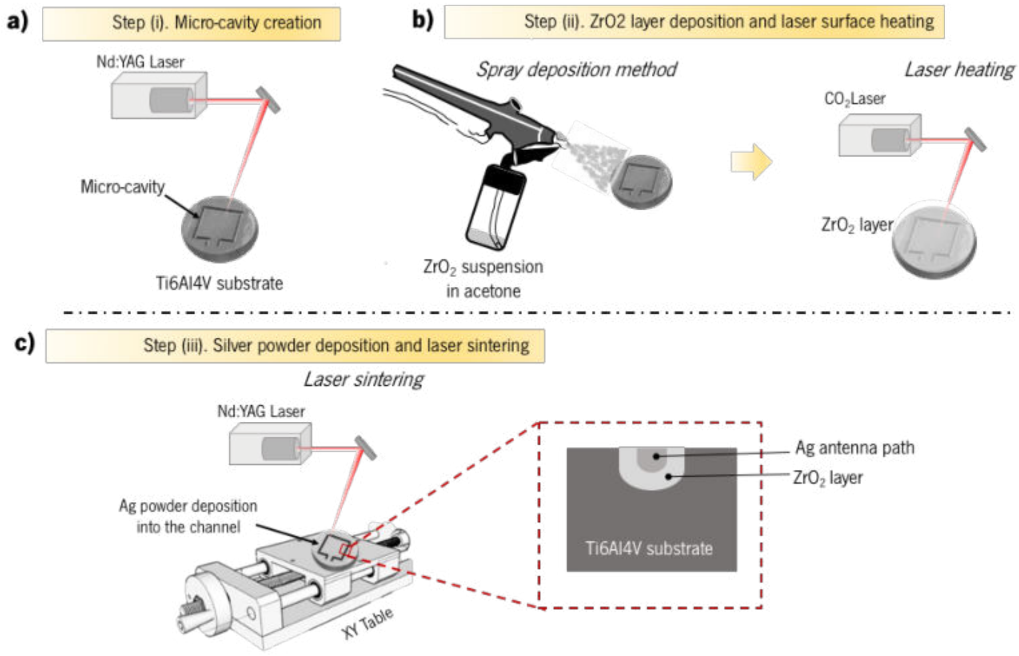

Figure 5.8 Schematic illustration of the antenna manufacturing on Ti6Al4V substrate (a-c).

The cross-section of the produced antenna was analysed using scanning electron microscopy (SEM - Nova NanoSEM 200, FEI, Netherlands) equipped with an Energy Dispersive Spectrometer (EDS). EDS analysis was performed using an energy of 15 keV.

5.3 Results and Discussion

5.3.1 Antenna characterization

A photography of the fabricated antenna is shown in Figure 5.9 below. The SEM image of the antenna fabricated is presented in Figure 5.10 with the detailed dimensions of the layers produced according to the method described in section 2.

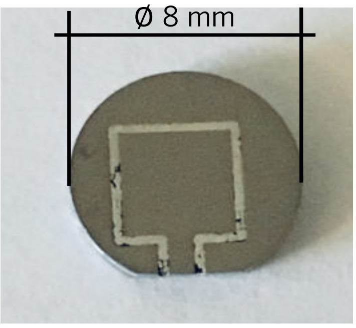

Figure 5.9 Photography of the fabricated antenna.

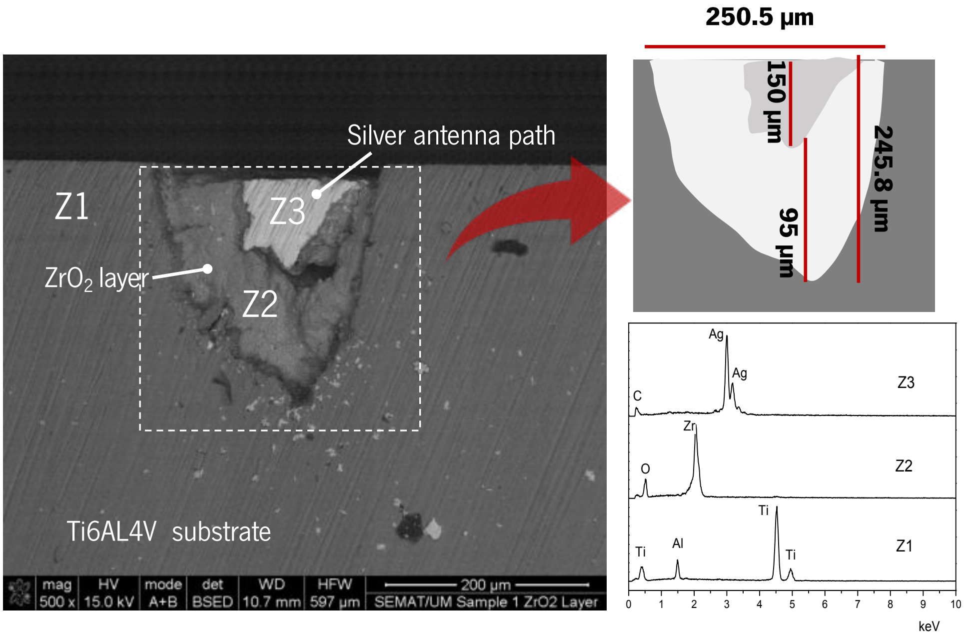

Figure 5.10 Cross-section SEM images of laser-generated micro-cavity after silver-based antenna manufacturing. On the right side, a schematic illustration of the micro-cavity and the dimensions of the layers, and EDS spectrum of each layer.

As it can be seen, the micro-cavity is completely filled by dielectric material (zirconia) and the antenna around the middle of zirconia layer. Through the laser strategy used, a cavity with a more rounded shape was obtained, due to the energy distribution. Generally, when laser beam is used to remove material from the surface through ablation mechanism, the quality of parts is reduced by melt accretions and thermal damage; however, this problem can be reduced with shorter pulse duration, although in this case, the ablation efficiency is reduced. Despite, laser ablation in the nanosecond range still offer great advantages and a good compromise between process quality and efficiency, depending on the strategy used to machine the surface and the material response.

In the laser strategy used, an increase of laser energy is obtained as increase the wobble amplitude, which is associated with the cavity width. Laser energy density (E) can be calculated through the equation showed in a previous study [9]. For instance, by varying the wobble from 25 to 250 µm, the laser energy density increases from 0.3 J/mm^2 to 30 J/mm^2, respectively. As a consequence of that, the energy is more concentrated when a larger area is machined, which avoids an acute shape of the cavity.

After the micro-cavity creation by laser ablation, as open space to antenna printing, a dielectric layer is required. For this, zirconia is the choice material, as previously mentioned. Thus, after the spray deposition of zirconia on the substrate, this layer was irradiated by means CO_2 laser source. Spray method was efficient for depositing a thick and homogeneous layer of zirconia. Others works have reported the spray deposition method as a simple and cheap technique for incorporating a material into a surface [10,11].

In comparison to laser sintering of metals, which is well established, laser sintering of ceramics encounters some difficulties. Their high melting points make difficult to melt and high energy input is required. Thus, although Nd:YAG lasers is one of the currently popular laser sources for processing ceramics, the continuous wave CO_2 laser is preferable, since its large wavelength of 10.6 µm can be absorbed directly by most of ceramics, including ZrO_2, but its focusing diameter is much bigger than that of the Nd:YAG laser, which leads to a decrease of the power intensity [12]. In additional, the CO_2 laser is less suitable for laser sintering of ceramics through the solid or liquid state mechanisms. In our case, as can be seen in the SEM images, the layer of zirconia is quite large, and they are not completely consolidated. Some grains are still released, requiring more laser energy to join them. In these cases, zirconia powder was mechanically trapped but not sintered. Even that, good adhesion was obtained of zirconia powder into the cavity.

After the process aforementioned, silver powder was filled into the laser generated micro-cavity. Through Figure 3 it is possible to see the silver path formed after the laser sintering process. It is possible to observe that silver powder was melted by laser and filled all the existing space after the dielectric deposition. As a consequence of the irregular roughness of the zirconia layer, silver path assumed an irregular shape with approximately 150 µm of depth. A successful laser sintering depends relies on fully or partially melting of the solid powder granules. Thus, the formed melt wets the un-melted powder granules, which facilitates a viscous flow and further the local consolidation. For this, it is crucial that the laser energy per volume and time is controlled carefully when converting from electromagnetic radiation to thermal heat.

Further improvements are necessary to control the final geometry of the antenna during its manufacturing as also its centralization, in order to preserve the same dielectric thickness around for enhancing the antenna performance. Despite this, all the processes applied in this proposed solution for a micro-antenna fabrication proved to be promising alternatives to the commonly applied methods, by using laser technique. Generally, these micro-devices are printed on an insulator substrate (i.e. polymeric) by using standard lithographic or chemical deposition techniques [13,14].

EDS analysis shows no silver oxide formation in the antenna path (Z3), after laser sintering. In additional, in the substrate zone (Z1), EDS presents Ti and Al peaks which is in agreement with Ti6Al4V composition. Vanadium is not present, because its amount is too low to be detected by this technique.

5.3.2 Performance assessment of the fabricated antenna by simulation

As seen in the previous section, the fabrication of the proposed antenna is not as straightforward as one would hope, and errors associated with the process itself mean that the final results aren’t exactly like the antenna that was designed in the previous section. Consequently, the simulation model was updated to represent the measurements presented in Figure 5.10. The detail of the uncentered silver line is presented in Figure 5.11. The return loss and radiation patterns at 2.6 GHz and 8.4 GHz are also presented in Figure 5.12.

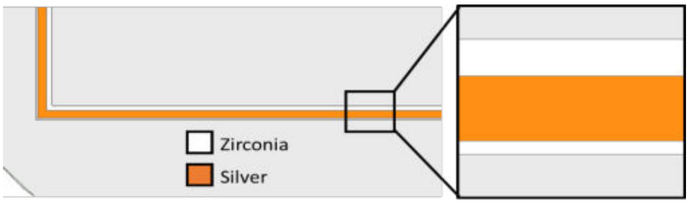

Figure 5.11 Uncentered silver line detail from the HFSS model of the fabricated antenna.

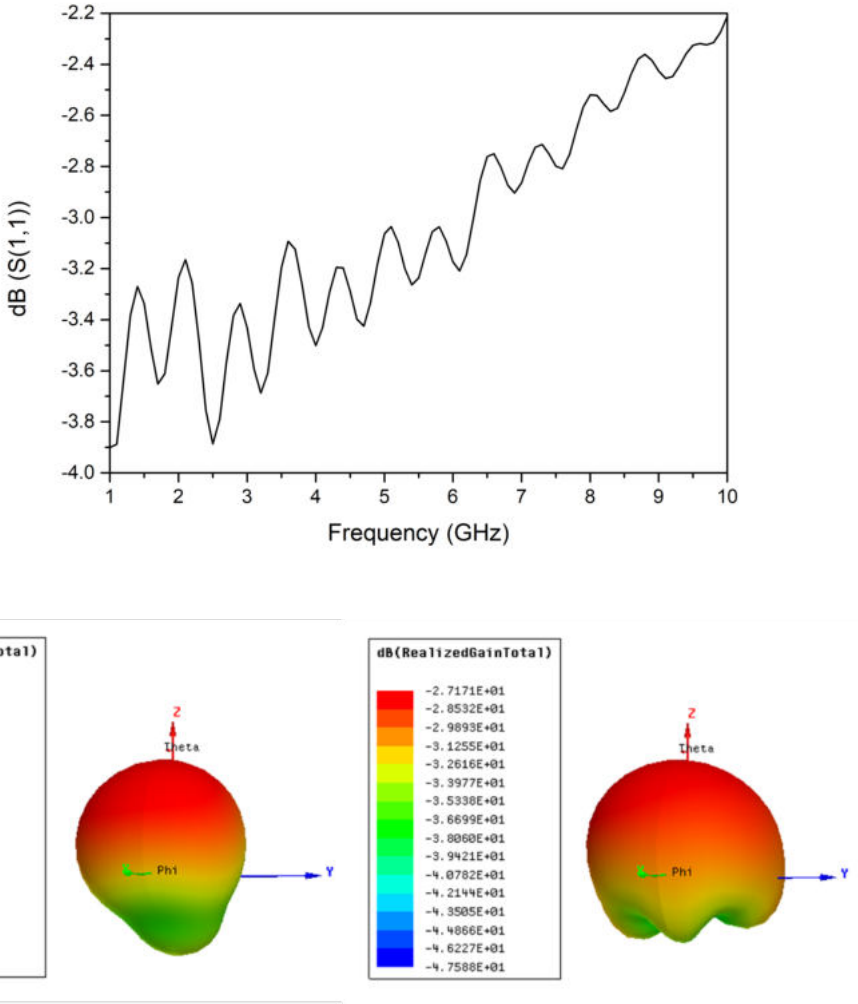

Figure 5.12 Return loss (top) and radiation patterns of the fabricated antenna at 2.6 GHz (bottom left) and 8.4 GHz (bottom right).

As it can be seen from the results of Figure 5.12, the return loss of the antenna is much higher in the entirety of the studied frequency range. This, in turn, is reflected in the decrease of the gain of the antennas at both the 2.6 and 8.4 GHz scenarios. Nevertheless, the behaviour that was observed in the previous chapter, i.e. better results at higher frequencies, are still observed in this updated model, as expected, since the same justifications are still valid. The deterioration of the results can, in turn, be due to the smaller dielectric insulator thickness that was experimentally achieved, especially in the one side where it is as thin as 30 μm.

5.4 Conclusions

The antenna plays a key role in establishing the communication between the implant and the user, through signal and data transmission. The ability to incorporate the antenna on the implant´s surface in a single step is of paramount importance to avoid further methods and to preserve its properties. The proposed approach has showed to be promising for printing antennas on Ti6Al4V-based implant surface. This achievement is made possible by using laser technique for creating the micro-cavity and also for consolidating the dielectric layer and the conductor path of the antenna.

The simulation results of the real case showed that the return loss of the antenna is much higher in the entirety of the studied frequency range. For both ideal and real cases, the better results are observed at higher frequencies and the deterioration of the outcomes in the real case can be due to the smaller dielectric insulator thickness that was experimentally achieved. Therefore, further simulations and experiments are needed in order to optimize the antenna efficiency by exploring higher and more accuracy dielectric thickness and its sintering conditions.

Conflicts of interest

The authors have no conflict of interest to declare.

Acknowledgement

This work has been supported by FCT (Fundação para a Ciência e Tecnologia -Portugal) in the scope of the projects UID/EEA/04436/2019 and NORTE-01-0145-FEDER-000018-HAMaBICo and Add.Additive_Manufacturing to Portuguese Industry_POCI-01-0247-FEDER-024533. I wish to thank the CNPq (205791/2014-0) and CAPES for the financial support.

References

[1] C. O'Connor, A. Kiourti, Wireless Sensors for Smart Orthopedic Implants, J. Bio- Tribo-Corrosion. 3 (2017) 1–8. doi:10.1007/s40735-017-0078-z.

[2] M. Pizzi, O. De Martiis, V. Grasso, Fabrication of self assembled micro reservoirs for controlled drug release, Biomed. Microdevices. 6 (2004) 155–158. doi:10.1023/B:BMMD.0000031753.02913.e2.

[3] G. Villani, R. Bose, A. Gabrielli, Evaluation of on-chip micro antennas for in vivo dosimetry application, Radiat. Meas. 46 (2011) 1963–1966. doi:10.1016/j.radmeas.2011.06.022.

[4] I. Singh, V.S. Tripathi, Micro strip Patch Antenna and its Applications : a Survey, 2 (2011) 1595–1599.

[5] D.H. Anacleto, P., Mendes, P. M., Gultepe, E., & Gracias, 3D small antenna for energy harvesting applications on implantable micro-devices., Loughbrgh. Antennas Propag. Conf. 1 (2012) 1–13. doi:doi:10.1109/lapc.2012.6402975.

[6] J.Y. Lee, W.S. Tan, J. An, C.K. Chua, C.Y. Tang, A.G. Fane, T.H. Chong, The potential to

enhance membrane module design with 3D printing technology, J. Memb. Sci. 499 (2016) 480–490. doi:10.1016/j.memsci.2015.11.008.

[7] A.K. Skrivervik, F. Merli, Design Strategies for Implantable Antennas, (2011) 1–5.

[8] Asimina Kiourti and Konstantina S. Nikita, A Review of Implantable Patch Antennas for Biomedical Telemetry : Challenges and Solutions, IEEE Antennas Propag. Mag. 54 (2012) 210–228.

[9] C.G. Moura, O. Carvalho, L.M. V Gonçalves, M.F. Cerqueira, R. Nascimento, F. Silva, Laser surface texturing of Ti-6Al-4V by nanosecond laser: Surface characterization, Ti-oxide layer analysis and its electrical insulation performance, Materials Science & Engineering C. 104 (2019) 109901. https://doi.org/10.1016/j.msec.2019.109901.

[10] K. Fujihara, A. Kumar, R. Jose, S. Ramakrishna, S. Uchida, Spray deposition of electrospun TiO2 nanorods for dye-sensitized solar cell, Nanotechnology. 18 (2007) 2–7. doi:10.1088/0957-4484/18/36/365709.

[11] A. Ranga Rao, V. Dutta, Low-temperature synthesis of TiO2 nanoparticles and preparation of TiO2 thin films by spray deposition, Sol. Energy Mater. Sol. Cells. 91 (2007) 1075–1080. doi:10.1016/j.solmat.2007.03.001.

[12] P. Regenfuss, A. Streek, L. Hartwig, S. Klotzer, T. Brabant, M. Horn, R. Ebert, H. Exner, Principles of laser micro sintering, 17th Solid Free. Fabr. Symp. SFF 2006. 4 (2006) 740–753. doi:10.1108/13552540710776151.

[13] D.T. V. Kyovtorov, I. Georgiev, S. Margenov, D. Stoychev, F. Oliveri, New antenna design approach-3D polymer printing and metallization. experimental test at 14-18 GHz, Int. J. Electron. Commun. 73 (2017) 119–128.

[14] P. Anacleto, P.M. Mendes, E. Gultepe, D.H. Gracias, Micro antennas for implantable medical devices, 3rd Port. Bioeng. Meet. ENBENG 2013 - B. Proc. (2013) 1–4. doi:10.1109/ENBENG.2013.6518405.

Chapter 6 - Laser printing of silver-based micro-wires in ZrO_2 substrate for smart implants applications

Under review in Journal of Optics and Laser Technology

C. G. Moura[1]*, D. Faria[1], O. Carvalho[1], R.S.F. Pereira[2], M. F. Cerqueira[3,4], R. M. Nascimento[5], F.S. Silva[1]

[1]CMEMS-UMinho, University of Minho, 4800-058, Guimarães, Portugal
[2]Federal Institute of Education Science and Technology of Santa Catarina, IFSC, Florianópolis, Brazil
[3]Centro de Física, University of Minho, 4710-057, Braga, Portugal
[4]International Iberian Nanotechnology Laboratory (INL), 4715 Braga, Portugal
[5]Materials Science and Engineering Post-Graduate Program, UFRN, 59078-970 Natal, Brazil

*Corresponding author – C. G. Moura (caroline.materiais@gmail.com)

Abstract

Smart implants are endowed with functions of sensing, actuating and control to solve problems that may arise during their use. The assembly of these functions along the implant surface is still a challenge. However, with the advent of 3D printing, it is possible to print on implants' surface, communication cavities or micro-antennas or even sensoric/actuating areas. Despite Ti6Al4V titanium alloy is the standard choice for implants fabrication, 3Y-TZP (tetragonal 3% mol yttria-stabilized zirconia) has emerged as a ceramic material suitable to overcome titanium alloy problems, due to its numerous advantages. In this sense, this work is concerned with the ability of printing silver-based communication system in zirconia substrates by using laser technology. For this, micro-cavities were created on ZrO_2 substrate, where the silver powder was placed and sintered into them. Through the laser approach silver-based wires with good quality and low resistivity values were achieved. The flexural strength of zirconia disks decreased after the wire printing on the surface but remained in an acceptable limit.

6.1 Introduction

Smart active implants incorporate functions of sensing, actuation, and control in order to describe and analyze a situation and make decisions based on the available data in a predictive or adaptive manner, thereby performing smart actions [1,2]. These implants need to have sensors, actuators, and communication cavities such as electrical wires and antennas (Figure 6.1). However, the assembling of these elements along the implant surface is difficult and will modify some desired characteristics of the implant for implantation, osseointegration, etc. Nevertheless, with the advent of 3D printing, mainly with multi-material approaches, it is possible to print, layer by layer, implants where a communication system, mimicking the central nervous system of lining bodies, local materials as sensors or actuators, such as piezo electric materials (for instance $BaTiO_3$), among other, may be successively printed giving rise to a component with an internal communication array of wires and local surface areas with ability to sense (temperature, PH, etc.) and or actuate (with electrical potentials, volume changing). It is also possible to print, on the implant's surface, communication cavities, or micro-antennas, or even sensoric/actuating areas.

This new concept of one component active implant with intrinsic smart functions, similar to biological bodies, is being investigated and manufactured with new complex multi-material 3D printing (Figure 6.2).

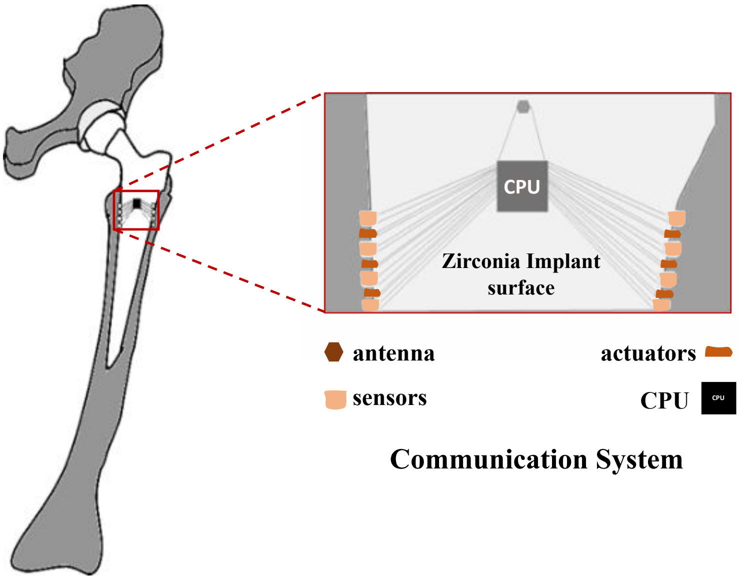

Figure 6.1 Schematic illustration of a zirconia implant with smart devices printed along the implant surface. Modified from [3].

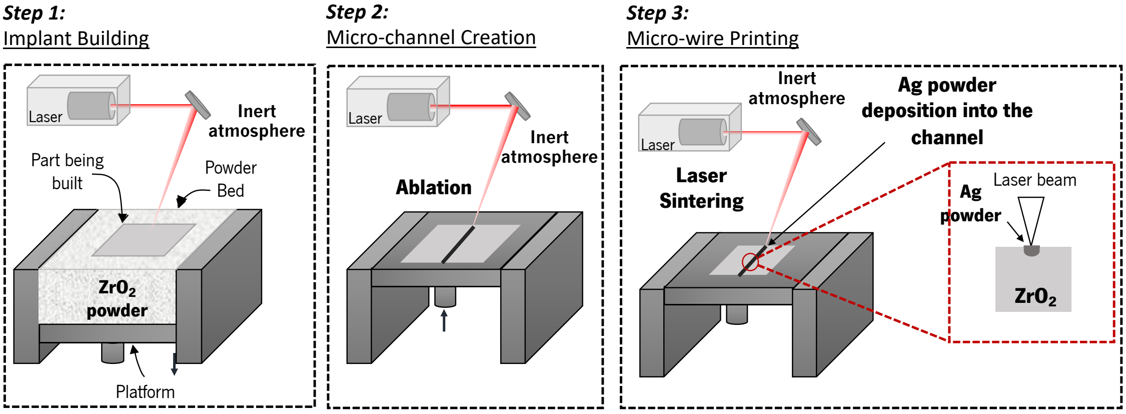

Figure 6.2 Illustrative scheme of the manufacturing steps of the antenna by 3D printing

Although titanium and its alloys are the standard choice for biomedical implants fabrication, tetragonal 3 mol% yttria stabilized zirconia (3Y-TZP) has arisen as a promising and eligible ceramic material for implants fabrication to overcome metal ions release and allergic reactions provided from titanium implants which compromise their durability. The main advantages of using zirconia is due to its high chemical and dimensional stability, mechanical strength, relatively good toughness, and low bacterial affinity [4–6].

Until this moment, the studies are focused on dental implants, in which several investigations have demonstrated a good performance of zirconia implants when compared to titanium alloy [7,8]. Several *in vivo* and *in vitro* investigations of soft tissue responses around zirconia revealed comparable or even better healing response, less inflammatory infiltrate and reduced plaque adhesion on zirconia compared to conventionally pure titanium [9–11]. Despite this, the drive towards ceramic implants to satisfy the increasing aesthetic demands and metal-free request is fraught with compromise. According to literature, there is still no valid scientific data available to recommend the routine clinical use of zirconia implants since the majority of the studies are either case reports or case series with a limited number of participants and short-term follow-up periods [8]. Furthermore, since zirconia is a brittle material with significant sensitivity to the surface defects, good control of quality during the manufacturing process is a necessity to enhance the long-term performance of the zirconia implants [12,13].

Based on the foregoing, this work is concerned with the ability of printing silver-based communication system in zirconia substrates by using laser technology. For this, micro-cavities were created on ZrO_2 substrate, where the silver powder was placed and sintered into them, forming a wire. The electrical measurements of the wires were assessed by using the four-probe method. The mechanical strength of zirconia disks before and after the wire printing was also performed.

6.2 Experimental details

6. 2.1 Zirconia disks fabrication

A commercial powder of 3% mol yttria stabilized zirconia – 3Y-TZP (TZ-3YB-E Tosoh Corporation, Japan) was used as feedstock to produce zirconia disks by press and sintering technique. The pressing of the TZ-3YB-E powder was performed on a steel cylindrical mold with an internal diameter of 18 mm. First, the TZ-3YB-E powder was placed into the mold and then, it was applied pressure of 200 MPa for 30 s. After that, the zirconia disks were sintered using a high-temperature furnace (Zirkonofen 700, Zirkonzahn, Italy) with a sintering temperature of 1500˚C, a heating and cooling rate of 8 ˚C/min and 2 h of holding time. After sintering, zirconia disks with 14.4 mm in diameter and 2 mm thick were obtained. All disks were ultrasonically cleaned in isopropyl alcohol for 10 min. to remove any loose debris or surface contamination.

6.2.2 Micro-cavities production

Surface laser texturing

A pulsed Nd:YAG laser (OEM Plus, working in wavelength of 1064 nm and 6 W of maximum power) was used to texture cavity in the surface of a 2 mm thick ZrO_2 disk. Figure 6.3 shows a schematic illustrating the used experimental set up (Figure 6.3a and b). The laser is pulsed, and the laser spot has a diameter of 3 μm, then each laser textured line consists in a sequence of several pulses with an overlap area (Figure 6.3a). For texturing the cavity, the distance between each line was changed from 10 to 50 μm in order to study the effect on the groove quality (Figure 6.3c).

As can be seen in Figure 6.3b, we have different groups of micro-cavities represented by grey and black rectangles. In each rectangle, there are five groups of lines with different distance between them, which will result in five different micro-cavities after laser scanning. The cavity was designed by using a drawing software and the width of the micro-cavities was projected to have 250 μm. Using these masks, the sample laser scanning was approached. Three laser scanning parameters were varied in this study, namely laser power, scanning speed and number of passes, in order to evaluate i) their influence on the quality of the cavity, ii) the amount of material re-solidified and iii) the depth achieved. Laser power represents the laser beam energy delivered per pulse in Watts; the scanning speed is the marking speed at the leading edge of the beam front in mm/s and the number of passes corresponds to the number of scans carried out by the laser during the process, which will affect the depth of the groove. Thus, in this study, the energy density was kept constant while the other parameters varied. Table 6.1 shows the combination of parameters used in this work.

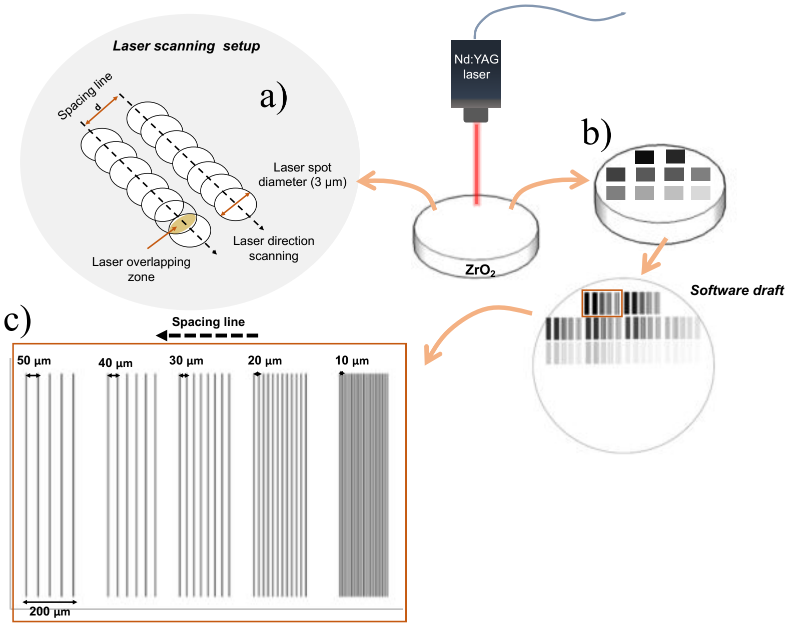

Figure 6.3 Scheme illustrating the experimental set-up of the laser processing (a and b). It is also shown a scheme illustrating the different kinds of cavity performed (b) and (c) illustrate the different line spacings tested. Modified from [3].

Table 6.1 Laser parameters combination

Sample	Power (W)	Scanning speed (mm/s)	Number of passes
Pack 1			
ZrP1.1	6	5	1
ZrP1.2	3	5	2
ZrP1.3	1.5	5	4
ZrP1.4	0.75	5	8
ZrP1.5	0.375	5	16
ZrP1.6	6	25	5
ZrP1.7	3	25	10
ZrP1.8	1.5	25	20
ZrP1.9	0.75	25	40
ZrP1.10	0.375	25	80
Pack 2			
ZrP2.1	6	50	10
ZrP2.2	3	50	20
ZrP2.3	1.5	50	40
ZrP2.4	0.75	50	80
ZrP2.5	0.375	50	160
ZrP2.6	6	100	10
ZrP2.7	3	100	20
ZrP2.8	1.5	100	40
ZrP2.9	0.75	100	80
ZrP2.10	0.375	100	160

The laser energy density (E) was calculated for each condition through the equation below:

$$E = \frac{P \times n}{v} \qquad (1)$$

Where P is the laser power, *E* is energy density in J/mm; *n* is the number of passes and *v* is the scanning speed in mm/s.

For each condition, there is a parameter combination in which the energy density corresponds to the same value, 20 J/mm.

6.2.3 Micro-wire printing

In the silver (Ag) wire printing, silver powder (≥ 99% pure) with an average grain size of 230 nm, from Metalor Technologies-USA, was deposited and compacted into the micro-cavity on ZrO_2 substrate. After the deposition, the powder was compacted by using a pressure of 8 MPa to ensure the total accommodation of the powder into the micro-cavity. The excess of the powder on the surface was removed through polishing with P800 grit SiC paper. In order to consolidate the powder into the micro-cavity, a pulsed Nd:YAG (Sisma - 1064 nm of wavelength) with a spot size of 0.3 μm and 100 J of maximum energy has been used. An energy of 10 J was used in all the samples. This value of energy was chosen as the best condition to melt the powder with fewer defects after several parameters' tests. The silver wires were characterized by Scanning Electron Microscope (SEM - FEI Nova 200) to evaluate the quality of the wire, in terms of densification. Energy Dispersive Spectrometer (EDS) was performed to verify the presence of silver oxidation.

6.2.4 Electrical measurements of the wires

In order to evaluate the electrical conductivity of the printed silver wires, the four-point probe method has been used (Figure 6.4). In this method a current is passed through the outer probes and induces a voltage in the inner voltage probes, resulting in a I x V curve. The range of applied current was 0.01 to 0.1 Ampère.

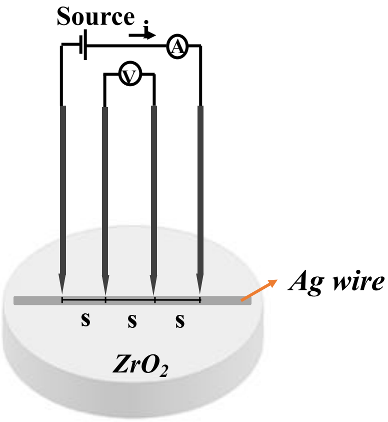

Figure 6.4 V x I curves with the resistance and the electrical resistivity values of each sample. The letter s represents the distance between the probes, which must be known.

The electrical performance was evaluated by comparing the resistivity (ρ) obtained by the application of Eq. 2 [14]:

$$\rho = R\frac{A}{L} \tag{2}$$

Where ρ is the resistivity, R is the resistance measured on the wire, L is the distance between each probe, and A is the cross-sectional area of the Ag wire. To obtain accurate resistivity, the actual cross-sectional area was assumed to be a uniform wire with approximately 200 µm of diameter. This equation for the resistivity calculation is the most adequate because as the wire is deposited in an insulating substrate, the conductivity is supplied by the metal present, since all the current flows through the wire.

6.2.5 Ball-on-three-balls (B3B) tests

In order to evaluate the effects of the silver wire printing on the zirconia surface regarding mechanical performance, the flexural strength of the samples was measured using the ball-on-three-balls test. The tests were done before the laser irradiation (as sintered sample), after the micro-cavity production by laser and after the silver wire printing on the cavity. The samples were then divided into three groups:

1. Zirconia samples as sintered (ZrAS);
2. Zirconia samples with a micro-cavity produced by laser (ZrP2.7);
3. Zirconia samples with a micro-cavity produced by laser containing a silver wire within the micro-cavity (ZrP2.7_Ag).

In the test, the intended side of the sample was positioned in the sample's holder on top of the three supporting steel balls equidistant from its center. The opposite surface was centrally loaded by a fourth ball coupled to the pin crosshead of the testing machine. The test started from a small preload and then the load increased until sample fracture. After that, the fracture load was recorded and the maximum tensile stress (σ_{max}), that occurs in the centre of the sample, on the opposite side of the loading ball, was calculated according to the Eq. 3 [15,16]:

$$\sigma_{max} = \frac{F}{t^2}\left[c_0 + \frac{c_1 + c_2(t/R) + c_3(t/R)^2 + c_4(t/R)^3}{1 + c_5(t/R)}\left(1 + c_6\frac{R}{R_a}\right)\right] \tag{3}$$

where F is the maximum force at fracture (N), t the sample thickness (mm), R the sample radius (mm), R_a the support radius (R_a=5 mm), and the parameters c0 to c6 refers to fitting factors for the geometrical correction term (c_0= -17,346 c_1= 20,774 c_2= 622.62 c_3= 76.879 c_4= 50.383 c_5= 33.736 c_6= 0.0613) [16]. It is worth noting that the latter parameters' values are dependent of Poisson's ratio of the studied material (υ= 0.3) [17]. After B3B tests, the fracture surfaces were analyzed by Scanning Electron Microscopy (SEM – FEI Nova 200). For this analysis, the samples were coated with an Au/Pd layer of 3 nm of thickness.

6.3 Results and Discussion

6.3.1 Surface morphology of the laser micro-cavity

Figure 6.5 (a and b) shows the SEM micrographs of the laser textured surface of ZrO_2 processed in air, in which (a) refers to the pack 1 and (b) refers to pack 2 of conditions. Figure 6.4 reveals the results of the parameters map tested, compound by 5 sets of micro-cavities (for each condition), with width around 200 μm, wherein each one was built by periodic lines spaced with different values: from 10 to 50 μm - as can be seen in Figure 6.3. For each combination of the used parameters, the value of energy density is the same. However, by analyzing the SEM images in Figure 6.5 it is seen that each parameter combination results in different surface changes, which means that each parameter has an important role in the surface modification.

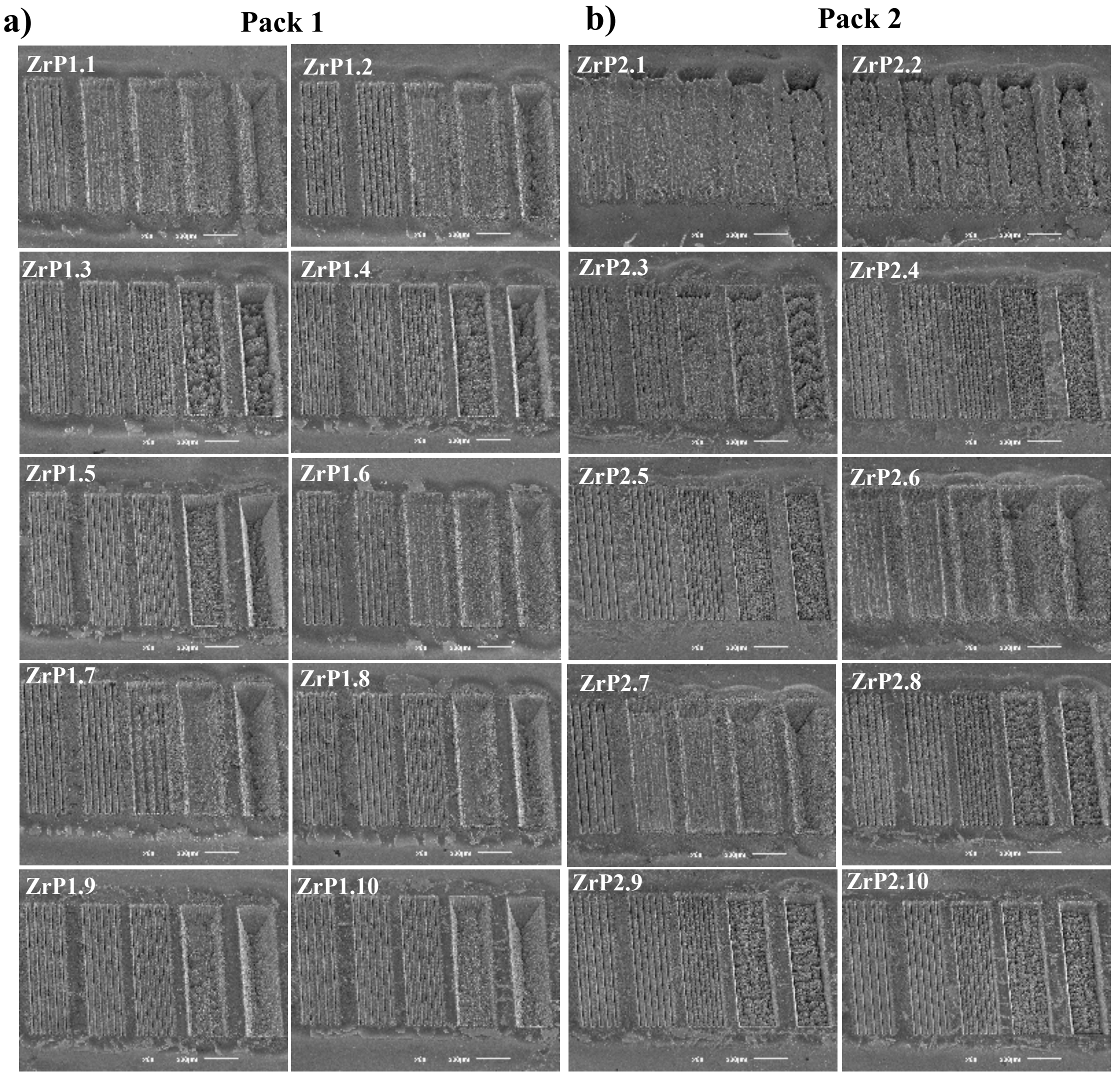

Figure 6.5 SEM micrographs of top surface of laser textured ZrO_2 with different parameters combination: a) pack 1, b) pack 2. Each textured area has 5 set of micro-cavities formed by lines with different spacing between the them, varying from 50 to 10 μm (from left to right).

In general, the laser scanning produced tracks of approximately 250 μm of width formed by overlapped lines. In addition, as can be observed that for the same energy density different surface morphologies can be obtained through combining different laser parameters. According to the images (Figure 6.5), the line spacing above 40 μm did not result in a micro-cavity formation, but a set of spaced tracks. Thus, taking into account that to print the wire, it is necessary to create a clean micro-cavity with considerable depth, only the spacing lines of 20 and 10 μm seems adequate. By analyzing the other parameters, in pack 1, from condition ZrP1.6, by increasing the scanning speed, the groove becomes cleaner and presents higher depth. However, in the conditions in which the scanning speed is lower (ZrP1.1 to ZrP1.5), the decrease of laser power is compensated by the increase of laser passes, resulting in micro-cavities with a great amount of re-solidified material droplets (debris) accumulated into the tracks. On the other hand, in pack 2, in which the scanning speed is higher, and more laser passes were performed, damaged surfaces were obtained in the conditions ZrP2.1 and ZrP2.2, presenting microcracks and holes on the surface, since higher output power is used. In general, only two conditions tested in this pack resulted in a desirable micro-cavity (ZrP2.6 and ZrP2.7), from the combination of high scanning speed and laser power with less laser passes. This result was already mentioned in previous studies, which reported the observation of microcracks on the zirconia surface after Nd:YAG treatment [18–20]. The presence of microcracks is a consequence of thermal gradients provided by rapid cooling during the laser irradiation. In literature, different methods to machining ceramics by laser for defect-free have been tested, for instance, underwater processing [21,22].

When the laser beam reaches a ceramic surface, physical phenomena take place, namely reflection, absorption, scattering and transmission. Absorption is the vital of all the effects, it is the interaction of the electromagnetic radiation with the electrons of the material and it depends on both the wavelength of the material and the spectral absorptivity characteristics of the ceramic being machined [23]. Furthermore, as the thermal conductivity of ceramics is generally less comparing to the majority of metals, the energy absorption takes place faster in ceramics and all the incident energy is immediately absorbed by the ceramic for the machining process [24–25].

6.3.2 Silver wire printing

After the study of laser parameters for the micro-cavities production on zirconia surface, the condition which resulted in a cleaner micro-cavity with a considerable depth has been selected. The main objective is to place the silver powder into the micro-cavity and sinter it by laser, forming a wire. Figure 6.6a shows the SEM micrographs of the selected micro-cavity, produced by using the parameters combination of condition ZrP2.7. For silver wire printing, the silver powder was placed and accommodated into the micro-cavity and sintered by laser with an energy of 10 Joules. Figure 6.6b presents SEM images of the silver wires after sintering into the micro-cavity. As can be observed the silver powder grains were apparently melted and spread to completely merge together with neighboring grains in both sintering conditions. However, some imperfections from the sintering is still evident. In laser sintering, localized energy is deposited, in which the powder is selectively irradiated and locally sintered, while the non-irradiated part of the laser stays unconsolidated [26], as occurred in our case. Another important aspect regarding laser sintering is related to a very steep temperature gradient that is generated due to the fast heating and cooling rate during the process. Because of the temperature gradient, during laser sintering of the wire, thermal stresses are generated due to the expansion restriction of the heated top layer, promoting compressive stresses. On the other hand, there is a contraction of the top layer of the metal powder, while the laser scans the surface, which is also restricted by the surrounding area, leading to tensile residual stress, being accumulated and resulting in cracks formation and delamination [27,28].

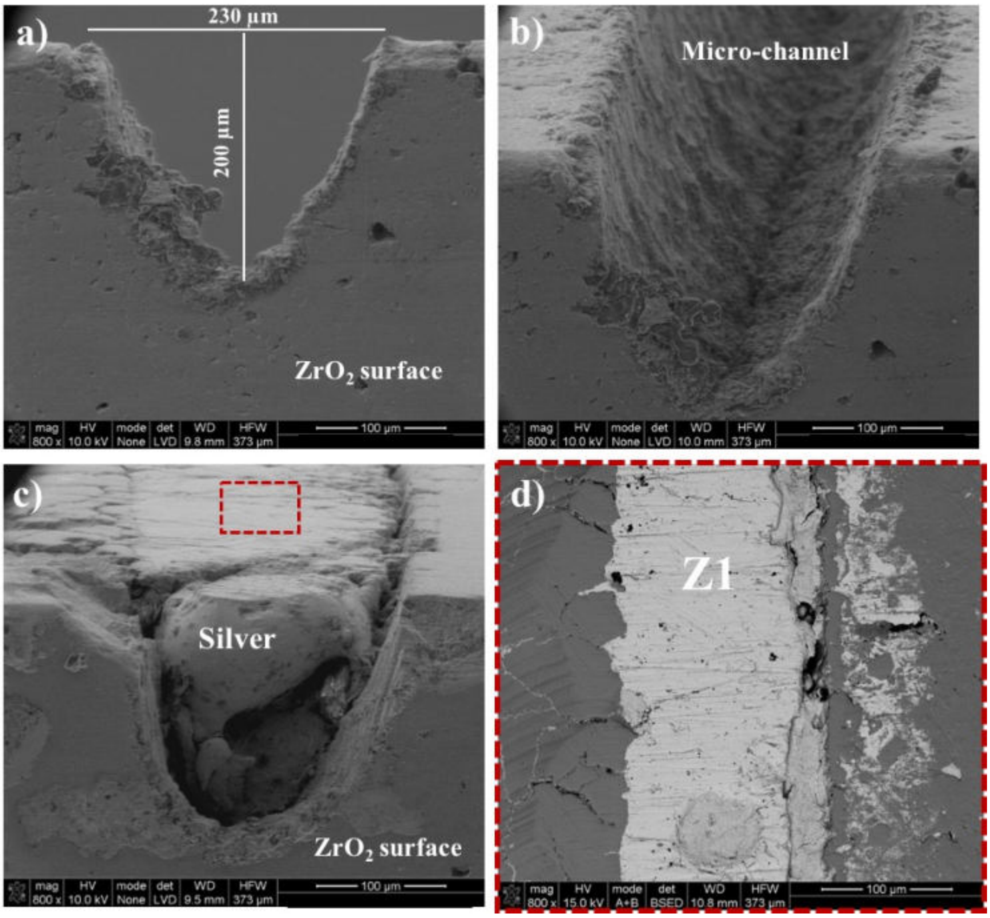

Figure 6.6 SEM micrographs of: a,b) Micro-cavity produced by ZrP2.7 condition trough laser irradiation. c,d) Micrograph of micro-cavity filled by silver powder and sintered by laser at 10 J of energy.

The EDS analyses (Figure 6.7) of the silver wire (Z1) shows the presence of the Ag element and no oxygen has been detected.

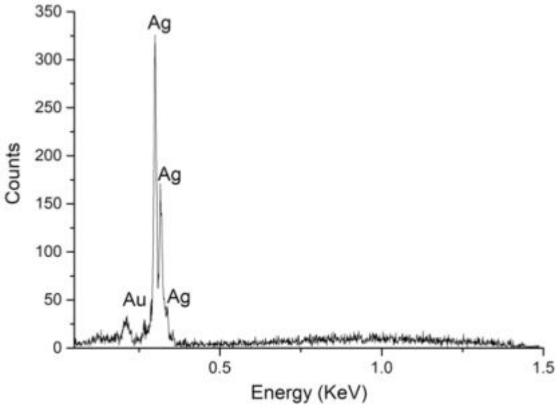

Figure 6.7 EDS spectrum of the silver wire zone (Z1) on zirconia substrate.

6.3.3 Electrical measurements of printed wires

After silver wire printing in the zirconia surface, electrical measurements were performed in order to evaluate their ability to conduct electrical current. For this purpose, the four-point probe method has been used by applying an electrical current and measuring the voltage resultant. Figure 6.8 presents the *VxI* curves of three samples prepared with the same conditions and the respective electrical resistance and resistivity values.

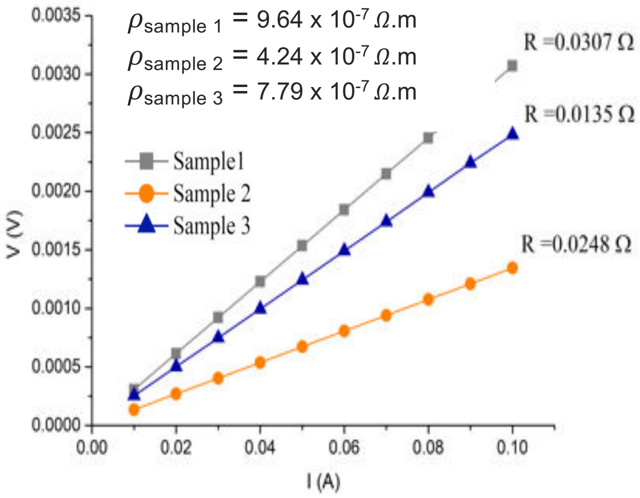

Figure 6.8 VxI curves with the electrical resistance and resistivity values of each sample measured.

Thus, assuming a uniform wire with known dimensions, the resistivity (*ρ*) of the silver wire can be calculated through VxI curves by using Eq. 2 and the values are presented in Figure 6.8. The values of zirconia and silver at room temperature, according to literature are 10^{12} and 1.6 x 10^{-8} Ω.m [29], respectively. According to the results, although the resistivity values of the silver wire are higher than the theoretical value, they are not so far apart. The difference between them may be related to the wire quality, which includes the impurities and imperfections resulting from the sintering process and may further decrease the mean free path of electrons. Such imperfection can be related mainly to the presence of porous. As it is well-known the sintering process is the atom diffusion driven by internal and external energies or forces. A denser microstructure would enhance the electrical conductivity, which indicates that good densification in the sintering process is a key to secure better electrical properties [30].

To date, the process of printing electronic devices and circuits in insulator substrates is already quite developed. However, the main processes of manufacturing involve high temperature and pressure in traditional sintering approaches, which are not tolerated by the soft substrates commonly used. Although several room-temperature and pressureless methods have been proposed, these methods are based on the use of chemical agents, compromising the electrical performance [31–33]. To the best of our knowledge, works related with printing local conductive cavities by using a single method (laser technology) are scarce. Our proposed method allows, starting from biocompatible materials, printing conductive wires on the surface of a zirconia implant, endowing it with various capacities, while using the laser for both cavity creation and sintering of conductive material. Finally, this methodology also resulted in conductive wires with good electrical performance when compared to the bulk material.

6.3.4 Flexural strength results

After verifying the electrical performance of the printed wires and taking into account that the substrate is a brittle material, it is necessary to evaluate zirconia substrate before and after receiving the wire, regarding mechanical properties. Among them, Nd:YAG pulsed laser has demonstrated to be adequate to scan the ceramic surface since, unlike the continuous mode, pulsed lasers provide easier control in their parameters [23,24]. However, due to the fast heat and cooling generated in laser scanning, the ceramic surface is damaged, and cracks can be formed [35]. In this sense, many efforts have been made in order to reduce heat related structural changes and damage on the ceramic surface. Despite this, there are still few studies focused in the influence of laser parameters on zirconia mechanical properties as well as studies related to groove production to place other materials. In Noda et al. [35], they presented the characterization of the surface damages of zirconia irradiated by Nd:YAG laser and the microstructural changes. The results revealed that cracks were formed after laser treatment and oxygen loss occurred. However, any mechanical property has been investigated in their study. Carvalho et al. [36] also presented an investigation regarding the influence of laser parameters and irradiation atmosphere on ZrO_2 surface. The main objective was creating cavities and functionalize them with bioactive materials for zirconia surface bioactivity improvement. Despite their satisfactory results of bioactive adhesion, the mechanical properties of zirconia after laser irradiation was not assessed.

Considering that the flexural strength is a mechanical property determining to evaluate the mechanical performance of zirconia implants, a biaxial bending strength test of brittle materials designated ball-on-three-balls test was performed.

According to the ISO 13356:2008 (Implants for surgery – ceramic materials based on yttria-stabilizes tetragonal zirconia (Y-TZP)), the flexural strength of zirconia should be ≥ 500 MPa [37]. In Figure 6.9 are shown the mean flexural strength values obtained from the B3B tests for each group of samples as well as the corresponding fractured samples.

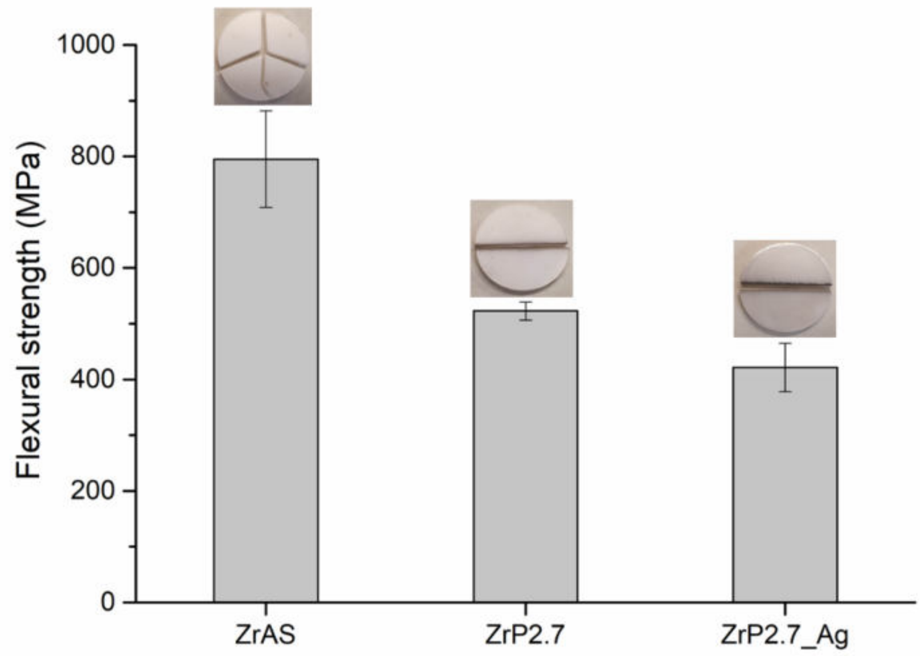

Figure 6.9 Mean flexural strength obtained from the ball-on-three-balls (B3B) test and the corresponding fragments of broken ZrAS, ZrP2.7 and ZrP2.7_Ag samples.

Analyzing the obtained results, a flexural strength value of 795 ± 87 MPa was obtained for ZrAS samples, which is in agreement with the standard defined by the ISO 13356:2008. Within the laser irradiated samples, there was a decrease in flexural strength values from 523 ± 16 MPa to 422 ± 43 MPa for ZrP2.7 and ZrP2.7_Ag samples, respectively. Additionally, by comparing flexural strength values of ZrP2.7 and ZrP2.7_Ag samples with ZrAS samples, a decrease was verified. This means that the mechanical resistance of zirconia was affected by the laser surface irradiation. Despite this reduction on the flexural strength values, it is important to highlight, that the value of ZrP2.7 samples is within the standard defined by the ISO 13356:2008. Regarding the ZrP2.7_Ag value, this found below of the one defined by the ISO 13356:2008. Reasons may lie on the fact of surfaces have been subjected twice times to the laser irradiation (laser ablation and laser sintering processes), while in the case of ZrP2.7 samples the surfaces were irradiated by laser one time in the step of micro-cavity production (laser ablation process), therefore, the mechanical performance was less compromised. Additionally, it is worth noting that the flexural strength value stated by the ISO 13356:2008 is defined for a zirconia sample without any surface treatment and in our study, the surface of the samples was irradiated by laser. Thus, it is expectable a decrease in flexural strength values after laser irradiation. Although Nd:YAG pulsed laser has demonstrated to be adequate to scan the ceramic surface, due to the fast heat and cooling generated in laser scanning, the ceramic surface is damaged.

Figure 6.10 presents the fracture surface of each group of samples. It can be seen from Figure 6.10a and b that, in all group of samples, the failure started from the bottom part of the samples, which corresponds to the tensile surface in the B3B test. The fracture surfaces exhibited typical fracture patterns of ceramic materials [38]. From Figure 6.10a.1 and b.1 there is visible a mixture of two types of fracture: intergranular and transgranular [39]. Additionally, it can be observed from Figure 6.10 that the fracture surfaces revealed the absence of detectable porosity within the samples.

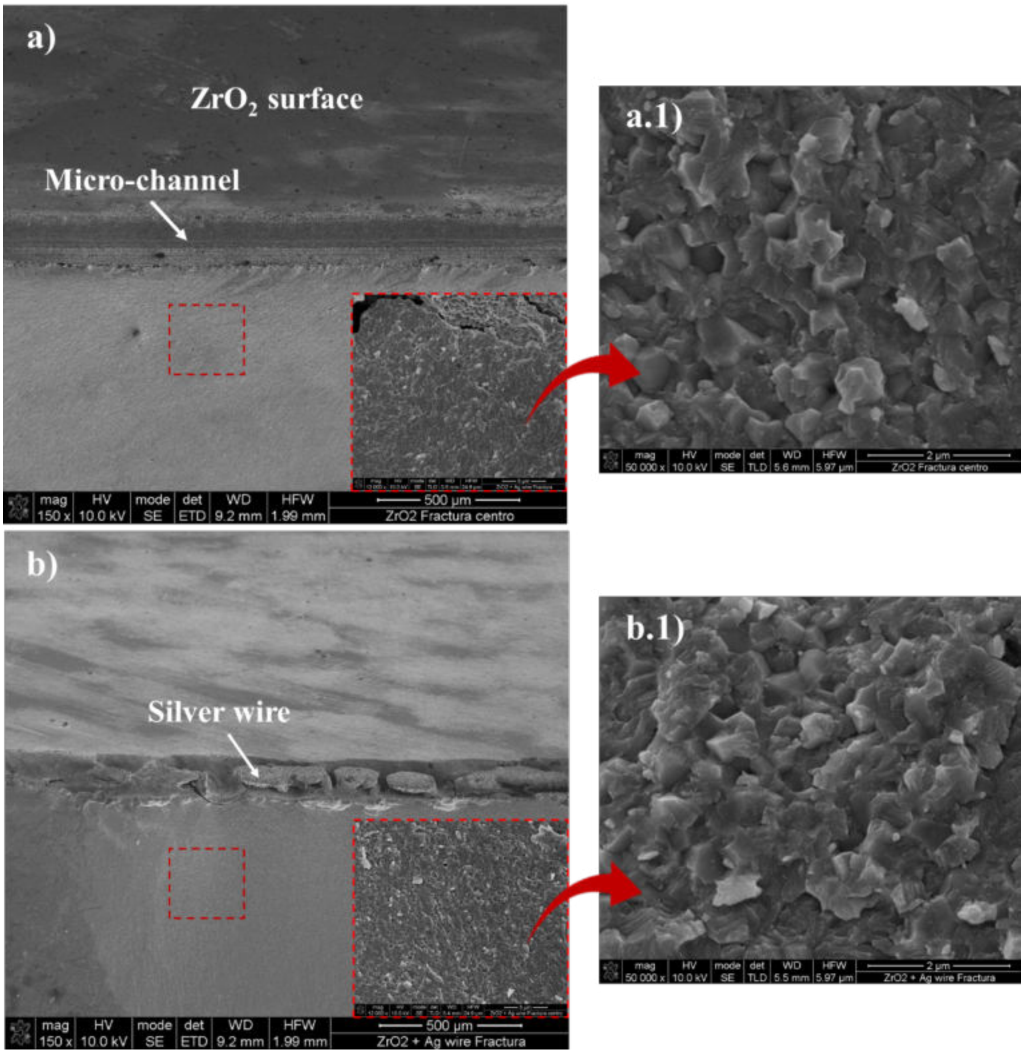

Figure 6.10. SEM micrographs of fracture surfaces of the samples: (a) and (a.1) ZrP2.7 and (b) and (b.1) ZrP2.7_Ag, after ball-on-three-balls (B3B) test.

6.4 Conclusions

In summary, laser technology proved to be a promising technique to produce micro-cavities on the zirconia surface with acceptable mechanical strength. Furthermore, laser technology was also efficient in the sintering process of silver powder into the cavities of zirconia, which resulted in wires with good quality and great electrical performance presenting low resistivity values.

In terms of mechanical performance of the substrate, although the presence of silver wire on zirconia surface decreased its mechanical strength, this result does not compromise the proposed application. Thus, taking into account that along with the implant there are different load regions, the communication system could be printed in a region with a low mechanical request. It is believed that the proposed approach is significant for the fabrication of an implant with intrinsic capacities that is useful for smart implants applications.

Conflicts of interest

The authors have no conflict of interest to declare.

Acknowledgement

This work has been supported by FCT (Fundação para a Ciência e Tecnologia -Portugal) in the scope of the projects UID/EEA/04436/2019 and NORTE-01-0145-FEDER-000018-HAMaBICo and Add.Additive_Manufacturing to Portuguese Industry_POCI-01-0247-FEDER-024533. Thank the CNPq (205791/2014-0) and CAPES for the financial support.

References

[1] C. O'Connor, A. Kiourti, Wireless Sensors for Smart Orthopedic Implants, J. Bio- Tribo-Corrosion. 3 (2017) 1–8. doi:10.1007/s40735-017-0078-z.

[2] B.S.M. Kurtz, K.L. Ong, J. Schmier, F. Mowat, K. Saleh, E. Dybvik, L.I. Havelin, O. Furnes, H. Malchau, E. Lau, U. States, N. Revision, Future Clinical and Economic Impact of Revision Total Hip and Knee Arthroplasty, 89 (2007) 144–151. doi:10.2106/JBJS.G.00587.

[3] M. Geetha, A.K. Singh, R. Asokamani, A.K. Gogia, Ti based biomaterials, the ultimate choice for orthopaedic implants – A review, Prog. Mater. Sci. 54 (2009) 397–425. doi:10.1016/j.pmatsci.2008.06.004.

[4] R.S. Park, J., & Lakes, Biomaterials: an introduction, Springer Science & Business Media, 2007.

[5] C. Ruff, B. Holt, E. Trinkaus, Perspectives Who ' s Afraid of the Big Bad Wolff ? : '" Wolff " s Law '' and Bone Functional Adaptation, 498 (2006) 484–498. doi:10.1002/ajpa.

[6] M. V Diamanti, M.P. Pedeferri, P. Milano, The Anodic Oxidation of Titanium and Its Alloys, 3 (2018) 41–54.

[7] C.L. and M. Peters, Titanium and titanium alloys: Fundamentals and applications, Wiley-VCH, 2003.

[8] M.E.T. S. Bruschi, S. Poggio, F. Quadrini, Workability of Ti-6Al-4V alloy at high temperatures and strain rates, Mater. Lett. 58 (2004) 3622–3629. doi:10.1016/j.matlet.2004.06.058.

[9] I.D. J. Robert Kelly, Stabilized zirconia as a structural ceramic: An overview, Denatl Mater. J. 24 (2008) 289–298. doi:10.1016/j.dental.2007.05.005.

[10] R.T. Garvie, R. C., Hannink, R. H., & Pascoe, Ceramic steel?, Nature. 258 (1975) 703–704.

[11] B.R.R. T.K. Gupta, J.H. Bechtold, R.C. Kuznicki, L.H. Cadoff, Stabilization of tetragonal phase in polycrystalline zirconia, J. Mater. Sci. 12 (1977) 2421–2426.

[12] A. Eichler, Tetragonal Y-doped zirconia : Structure and ion conductivity, 64 (2001) 1–8. doi:10.1103/PhysRevB.64.174103.

[13] P. Ducheyne, Comprehensive biomaterials (Vol. 1)., Elsevier, 2015.

[14] T. Sato, Transformation of yttria partially stabilized zirconia by low temperature annealing in air, 20 (1985) 1466–1470.

[15] X. Guo, On the degradation of zirconia ceramics during low-temperature annealing in water or water vapor, 60 (1999) 539–546.

[16] J. Chevalier, What future for zirconia as a biomaterial? Biomaterials. 27 (2006) 535–543. doi:10.1016/j.biomaterials.2005.07.034.

[17] W. Jin, P.K. Chu, H. Kong, Orthopedic Implants, (2017).

[18] N. Claussen, W.M. Kriven, M. Ruhle, Stability of Tetragonal Zr02 Particles in Ceramic Matrices, (n.d.) 642–650.

[19] E.H. Ledet, B. Liddle, K. Kradinova, S. Harper, Smart implants in orthopedic surgery, improving patient outcomes: a review, (2018) 41–51.

[20] A.-P. J., L. D.R., I. H.M.D., Y. G.-Z., From Wearable Sensors to Smart Implants-Toward Pervasive and Personalized Healthcare, IEEE Trans. Biomed. Eng. 62 (2015) 2750–2762. doi:10.1109/TBME.2015.2422751.

[21] F. Graichen, R. Arnold, A. Rohlmann, G. Bergmann, Implantable 9-Cavity Telemetry System for In Vivo Load Measurements With Orthopedic Implants, 54 (2007) 253–261.

[22] V.L. Roberts, Strain-gage Techniques in Biomechanics response of biological system to mechanical inputs, (n.d.) 19–22.

[23] G. Bergmann, Four-cavity measurement, J Biomed Eng. 13 (1991) 370–374.

[24] F. Burny, M. Donkerwolcke, F. Moulart, R. Bourgois, R. Puers, Concept , design and fabrication of smart orthopedic implants, 22 (2001) 469–479.

[25] G. Bergmann, F. Graichen, Hip joint contact forces during stumbling, (2004) 53–59. doi:10.1007/s00423-003-0434-y.

[26] L.A. Ferrara, A.J. Fleischman, D. Togawa, T.W. Bauer, E.C. Benzel, S. Roy, An in vivo Biocompatibility Assessment of MEMS Materials for Spinal Fusion Monitoring, (2003) 297–302.

[27] R. Melik, N.K. Perkgoz, E. Unal, C. Puttlitz, H.V. Demir, Bio-implantable passive on-chip RF-MEMS strain sensing resonators for orthopaedic applications, J. Micromechanics Microengineering. 18 (2008) 115017. doi:10.1088/0960-1317/18/11/115017.

[28] P.J. Sell, Instrumented, J. Biomed. Eng. 11 (1989) 111–112.

[29] R.E. Newnham, ensors, Actuators, and Smart Materials, (1993) 27–33.

[30] R.K.S. Parul Gupta, Vineet Tirth, Structural Applications of Smart Materials in Construction Engineering Using Robotics, IEEE. (2006) 8–11.

[31] K.Y. Yazdandoost, Wireless Communications for Body Implanted Medical Device, (2007).

[32] A. Kiourti, K.A. Psathas, K.S. Nikita, Review Implantable and Ingestible Medical Devices WithWirelessTelemetry Functionalities: A Review of Current Status and Challenges, 15 (2014). doi:10.1002/bem.21813.

[33] A. Kiourti, K.S. Nikita, S. Member, A Review of In-Body Biotelemetry Devices: 64 (2017) 1422–1430.

[34] M.M. Ahmadi, G.A. Jullien, L. Fellow, A Wireless-Implantable Microsystem for Continuous Blood Glucose Monitoring, 3 (2009) 169–180.

[35] A.K. Skrivervik, F. Merli, Design Strategies for Implantable Antennas, (2011) 1–5.

[36] R.F. Harrington, Effect of Antenna Size on Gain, Bandwidth, and Efficiencyl, 64 (1960).

[37] P. Soontornpipit, C.M. Furse, Y.C. Chung, Design of Implantable Microstrip Antenna for Communication With Medical Implants, 52 (2004) 1944–1951.

[38] Asimina Kiourti and Konstantina S. Nikita, A Review of Implantable Patch Antennas for Biomedical Telemetry: Challenges and Solutions, IEEE Antennas Propag. Mag. 54 (2012) 210–228.

[39] J. Abadia, F. Merli, 3D-Spiral Small Antenna Design and Realization for Biomedical Telemetry in the MICS band, 18 (2009) 359–367.

Chapter 7 - Laser printing of silver-based micro-antenna on ZrO_2 substrate for smart implants applications

Submitted to Bioelectronics and Biosensors

C. G. Moura[1]*, H. Dinis[1], O. Carvalho[1], P. M. Mendes[1], R. M. Nascimento[2], F.S. Silva[1]

[1]CMEMS-UMinho, University of Minho, 4800-058, Guimarães, Portugal

[2]Materials Science and Engineering Post-Graduate Program, UFRN, 59078-970 Natal, Brazil

*Corresponding author – C. G. Moura (caroline.materiais@gmail.com)

Abstract

3Y-TZP (tetragonal 3% mol yttria-stabilized zirconia) has emerged as a ceramic material suitable to overcome titanium alloy in implants' fabrication, due to its numerous advantages. The metal ions releases and aesthetic problems of titanium alloy implants are the main reasons for this trend. In addition to meeting expectations regarding properties, the implant must own intrinsic capacities, such as auto-diagnostic and auto-treatment. Thus, based on smart implants concept, this work purposes a hybrid approach for printing a part of the communication system of zirconia implant by using laser technology, aiming to endow the implant with intrinsic capacities. In this sense, the antenna designed was printed on zirconia surface through laser technology. Silver powder was used as the conductor material of the antenna.

Keywords: Nd:YAG laser; smart implants; communication system; antenna; zirconia implants.

7.1 Introduction

In the biomedical field, titanium and its alloys have been the gold standard choice for implants, mainly due to their mechanical performance and excellent biocompatibility [1–3]. Despite this, the release of ions and allergic reactions have been reported as the main causes of the titanium implant failure.

In this sense, tetragonal 3 mol% yttria stabilized zirconia (3Y-TZP) has arisen as a promising and eligible ceramic material for implant fabrication, capable to overcome titanium implant deficiencies [4–7]. To date, studies regarding zirconia-based implants are mainly directed to dental field. Several authors have demonstrated that, for the concerned application, zirconia implants present a good performance when compared to titanium alloy [8,9]. Nevertheless, the trend for implants in zirconia is fraught of compromises, mainly because zirconia is a brittle material with significant sensitivity to surface defects. Therefore, a good quality control during the manufacturing process is necessary for a satisfactory long-term performance of zirconia implants.

Consequently, future works should focus on evaluating the optimal design for the next generation of zirconia implants aligned with the concept of smart implants, in order to endow the implant with intrinsic capacities. Some of these capacities are related to sensing, actuating, and control, in order to describe and analyze issues and make decisions based on the available data in a predictive or adaptive manner, thereby performing smart actions. Thus, these implants should have sensors, actuators and a communication array of wires and antennas (Figure 7.1). The latter is responsible to transmit information between the implant-adjacent environment and the user. To be printed in the implant, the antenna should be very small and require very low power, thus designing an efficient antenna is a key requirement for the communication system [10].

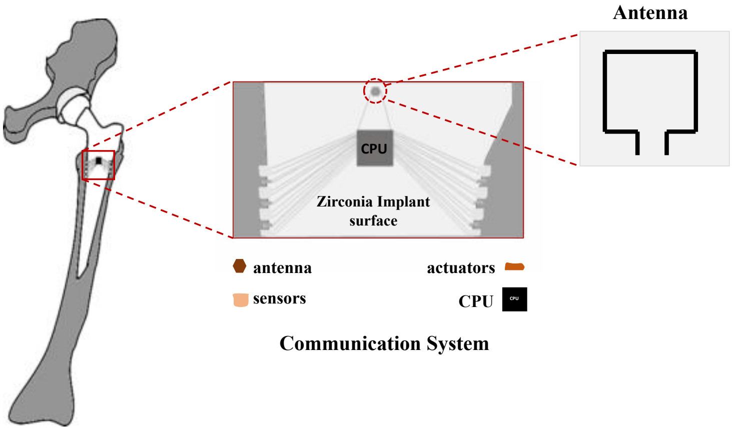

Figure 7.1 Schematic illustration of a hip implant with smart components printed on its surface, highlighting the antenna. Modified from [3].

Within the smart implants manufacturing, the conventional methods used to fabricate antennas in an insulator substrate may entail time-consuming and additional fabrication steps [11,12]. However, resorting to 3D printing technology, it is possible to print, layer by layer, implants with smart components, such as sensors, actuators, and antennas in a single step.

Therefore, this works is concerned with the ability to print a silver-based communication antenna in zirconia substrate by 3D printing-based approach. It provides the manufacturing steps and determines the suitability of the printed antenna to be used in an implant for communication purposes.

7.2 Experimental details

7.2.1 Materials

In this work, commercial Yttria-stabilized zirconia (3Y-TZP) powder with dispersion of 3 mol% Yttria (Tosoh Corporation, Japan), with particle size of 40 nm (in agglomerated size of 60 μm) was used to produce zirconia disks, as the antenna substrate. As the conductor material of antenna, silver powder (≥ 99% pure) with an average grain size of 230 nm, from Metalor Technologies-USA was used.

7.2.2 Samples preparation

Zirconia disks were produced by press and sintering technique. The pressing of the TZ-3YB-E powder was performed on a steel cylindrical mold with an internal diameter of 18 mm. First, the TZ-3YB-E powder was placed into the mold and then, it was applied pressure of 200 MPa for 30 s. After that, the zirconia disks were sintered using a high-temperature furnace (Zirkonofen 700, Zirkonzahn, Italy) with a sintering temperature of 1500 °C, a heating and cooling rate of 8 °C/min and 2 h of holding time. After sintering, zirconia disks with 14.4 mm in diameter and 1.8 mm thick were obtained.

7.2.3 Antenna production

The antenna printing was performed by three steps:

a) Micro-cavity creation by laser scanning;
b) Silver powder deposition into the cavity;
c) Laser sintering of the silver powder.

The schematic representation of laser machining is illustrated in Figure 7.2.

Micro-cavity creation by laser scanning

In this step, a Nd:YAG laser (OEM Plus) working in a wavelength of 1064 nm, a spot size of 3 μm and 6 W of maximum power was used to create the micro-cavity on zirconia surface. To create the micro-cavity a sequence of lines was performed with a distance of 10 μm between them, forming a cavity of approximately 350 μm width. The cavity was created by using a laser energy of 0.72 J/mm and a scanning speed of 50 mm/s. Figure 7.2a illustrates this step.

Silver powder deposition into the cavity

After the cavity creation on zirconia surface, the silver powder was deposited and compacted into the cavity on zirconia substrate (Figure 7.2b). After the deposition, the powder was compacted by using a pressure of 8 MPa to ensure the total accommodation of the powder into the cavity. The excess of the powder on the surface was removed through polishing with P800 grit SiC paper.

Laser sintering of the silver powder

In the silver powder consolidation, a Nd:YAG laser (Sisma) with 1064 nm of wavelength, a spot size of 0.3 µm and 100 J of maximum energy has been used. An energy of 10 J was used in the sintering process.

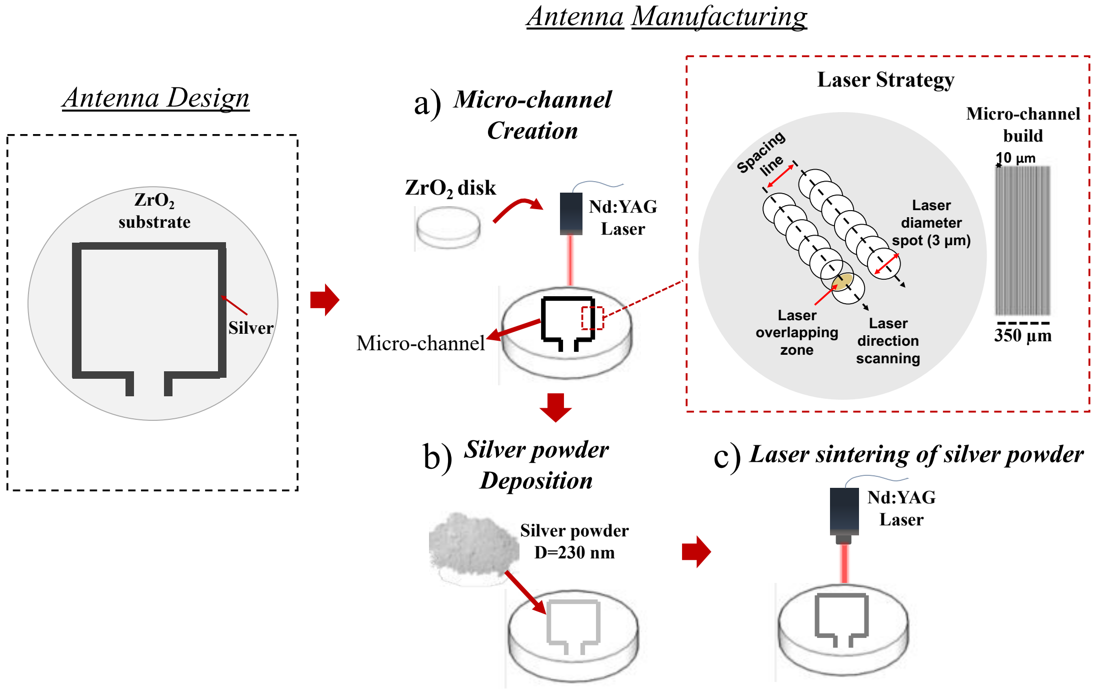

Figure 7.2 Schematic illustration of the antenna design and manufacturing (a-c), highlighting the laser strategy used to create the micro-cavity

7.2.4 Antenna performance

Characterization and testing of the fabricated antenna began by interfacing it with standard measurement equipment. For that, a U.FL cable was cut in half and its ground and signal lines were separated, as shown in Figure 7.3a. Each of these terminations was then connected to the antenna resorting to silver conductive paint, resulting in the device of Figure 7.3b.

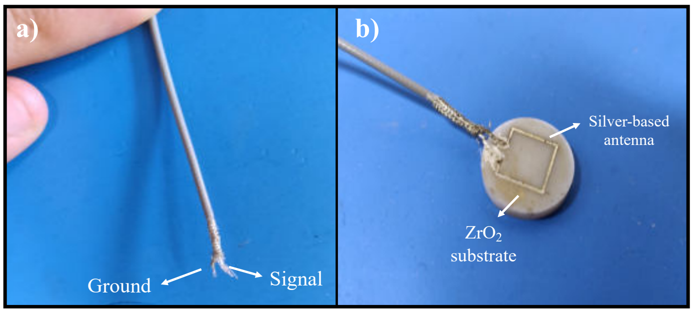

Figure 7.3 Photographs of the U.FL cable with signal and ground terminations separated (a) and of the fabricated antenna ready for testing

The antenna was connected to a Keysight E5071C VNA to measure its properties and determine its suitability for use inside the human body as a communication antenna. To do so, the antenna under test was placed between two 1 cm thick beef steaks to approximate the test's conditions to the antenna's operating conditions once it is implanted. This is an important step because the surrounding environment has a profound effect in the radiation characteristics of an antenna. The measurement setup is presented in Figure 7.4. A Q-par Angus WBH2-18S horn antenna was used as a transmitter, and it placed 25 cm away from the fabricated antenna. A polymeric foam was used to hold the structure of DUT test, and it is invisible to electromagnetic waves in the frequency range used (it behaves as air).

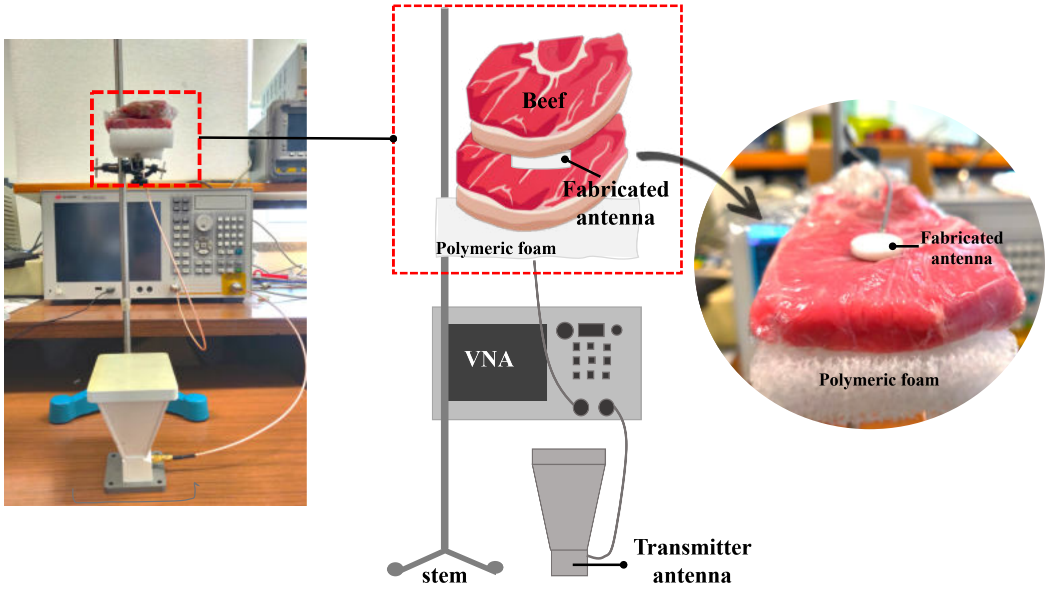

Figure 7.4 Photograph of the antenna testing setup. The transmitter antenna is distanced 25 cm from the fabricated antenna, which is placed between two 1 cm thick beef steaks for human.

7.3. Results and Discussion

7.3.1 Antenna production

Figure 7.5 presents the SEM images of the micro-cavity created by laser on zirconia surface. The micro-cavity was produced in accordance with the defined antenna design.

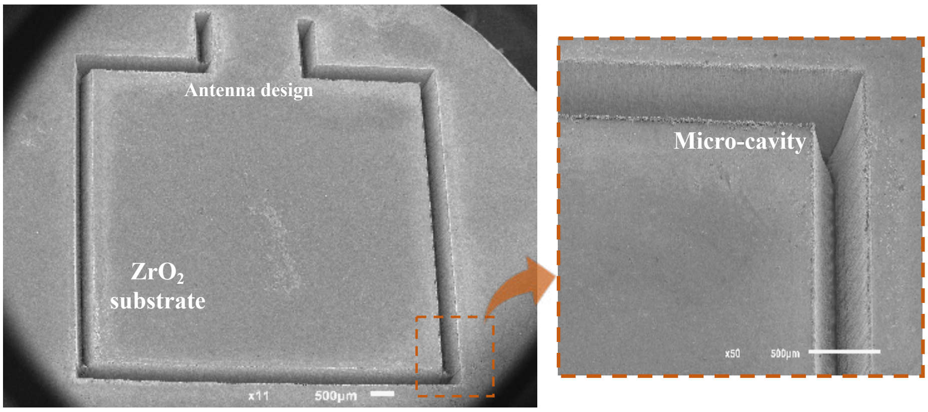

Figure 7.5 Micro-cavity of the antenna created by laser on zirconia surface.

After the micro-cavity created on the surface, silver powder was placed into the cavity and consolidated by laser sintering/melting approach. Figure 7.6 shows a part of the antenna after laser consolidation.

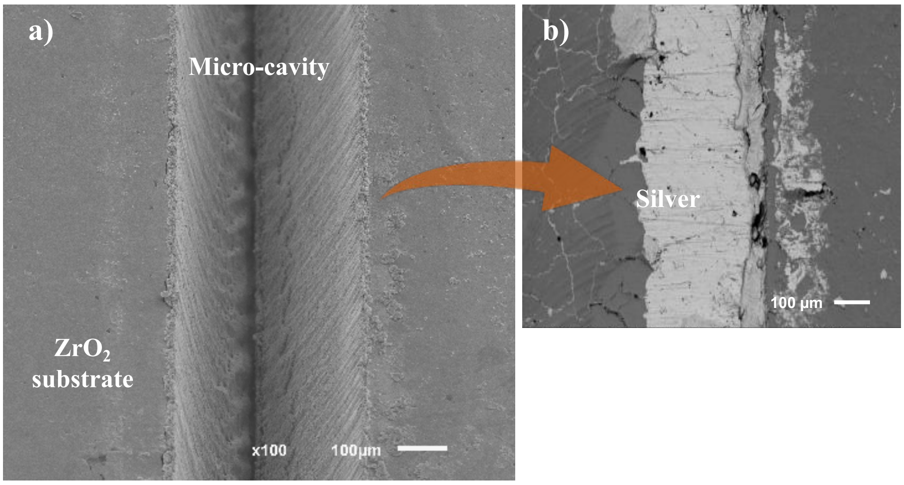

Figure 7.6 (a) A part of the micro-cavity of the antenna created by laser on zirconia surface, (b) the micro-cavity filled with silver powder after laser sintering/melting.

As it can be observed, the silver powder grains were apparently melted in the sintering condition. However, some imperfections from the sintering is still evident, such as voids due to gases accumulation during the process. The great advantage regarding this technique is the possibility to sinter specific zones by concentrating the laser energy. Despite that, due to the inherent nature of rapid heating and cooling during the laser sintering, the materials normally receive high residual stress. In some cases, even cracks may be initiated in the surrounding area. The distribution and magnitude of the residual stress are influenced by the laser scanning strategy, materials properties and environmental conditions. This aspect is evidenced by Figure 7.6b, in which some micro-cracks are present in zirconia substrate, after laser sintering process of the antenna. Although the laser beam focused only in silver path, the heat from laser irradiation promoted thermal stress on ceramic substrate.

7.3.2 Antenna performance

The return and transmission losses of the antenna are displayed in Figure 7.7. Through their analysis, it is possible to conclude that the antenna, when placed inside biological tissue, operates best at 2.4 GHz, as its S11 parameter is the lowest at that frequency and the S21 parameter is the highest. Operation at 2.4 GHz, i.e. the ISM band, is an attractive feature of the antenna, as common communication protocols, e.g. Wi-fi and Bluetooth, also utilize this band, thus making it easier to establish a communication link with the implanted device.

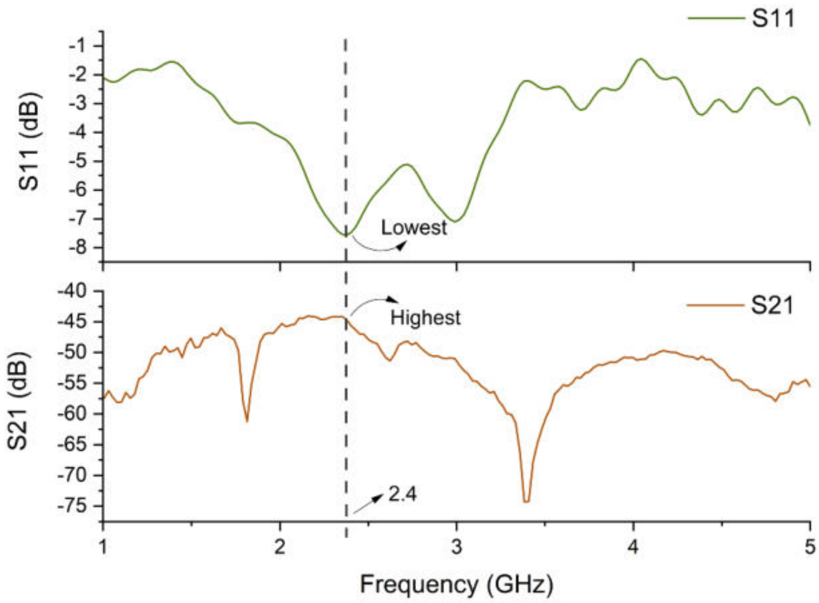

Figure 7.7 S11 (top) and S21 (bottom) parameters measured through the VNA for a frequency range of 1 to 5 GHz, which demonstrate that the antenna is better suited to operate at 2.4 GHz.

Further analysis of the experimental results, namely the S_{21} parameter, indicate that the fabricated antenna is capable of receiving -45 dBm of power from the transmission antenna at 2.4 GHz when they are 25 cm apart. These -45 dBm are well above what is required for a communication system's antenna, as these can operate at values between -90 dBm and -125 dBm, and there are cases where the receiver's sensitivity is as low as -150 dBm [10].

Consequently, it is possible to affirm that the antenna fabricated through the proposed method can be used in an implant to communicate data with the outside world without the need to have the exterior antenna attached to the skin (due to the 25 cm separation used in the tests), thus allowing for truly tether-less applications.

7.4 Conclusions

A promising approach to produce a silver-based antenna on a ceramic substrate was presented in this work. Laser technology was employed as a versatile tool to produce micro-cavity in zirconia substrate (as a subtractive process) and also to sinter the antenna material into the cavity (as an additive process). A micro-cavity with the desired antenna design was created by laser on the zirconia surface and then, silver powder was successfully sintered into this cavity, forming a conductor path. Besides being a fast and inexpensive manufacturing technique, this approach can be applied also for other and more complex designs. The results showed the efficiency of the used approach regarding the signal transmission from inside the human body environment to the exterior. The fabricated antenna is capable of receiving -45 dB of power at 2.4 GHz from a transmitter, which is above of the required for a communication system's antenna and well below safety electromagnetic exposure limits. Consequently, it is made possible its use in an implant for data communication with the outside world without needing to have an exterior antenna attached to the skin.

Conflicts of interest

The authors have no conflict of interest to declare.

Acknowledgement

This work has been supported by FCT (Fundação para a Ciência e Tecnologia -Portugal) in the scope of the projects UID/EEA/04436/2019 and NORTE-01-0145-FEDER-000018-HAMaBICo and Add.Additive_Manufacturing to Portuguese Industry_POCI-01-0247-FEDER-024533. Thank the CNPq (205791/2014-0) and CAPES for the financial support.

References

[1] V.Y. Zadorozhnyy, E. V. Kaevitser, A.N. Kopylov, Y. V. Borisova, V. V. Sudarchikov, R.S. Khasenova, M. V. Gorshenkov, M.Y. Zadorozhnyy, S.D. Kaloshkin, Synthesis of the hydroxyapatite coatings on the Ti substrates by mechanical alloying, Surf. Coatings Technol. 281 (2015) 157–163. doi:10.1016/j.surfcoat.2015.09.056.

[2] E. Mohseni, E. Zalnezhad, A.R. Bushroa, Comparative investigation on the adhesion of hydroxyapatite coating on Ti-6Al-4V implant: A review paper, Int. J. Adhes. Adhes. 48 (2014) 238–257. doi:10.1016/j.ijadhadh.2013.09.030.

[3] C.G. Moura, O. Carvalho, L.M. V Gonçalves, M.F. Cerqueira, R. Nascimento, F. Silva, Laser surface texturing of Ti-6Al-4V by nanosecond laser: Surface characterization, Ti-oxide layer analysis and its electrical insulation performance, Materials Science & Engineering C. 104 (2019) 109901. https://doi.org/10.1016/j.msec.2019.109901.

[4] H. Reveron, M. Fornabaio, P. Palmero, T. Fürderer, E. Adolfsson, V. Lughi, A. Bonifacio, V. Sergo, L. Montanaro, J. Chevalier, Towards long lasting zirconia-based composites for dental implants: Transformation induced plasticity and its consequence on ceramic reliability, Acta Biomater. 48 (2017) 423–432. doi:10.1016/j.actbio.2016.11.040.

[5] C. Piconi, G. Maccauro, Zirconia as a ceramic biomaterial, Biomaterials. 20 (1999) 1–25. doi:10.1016/S0142-9612(98)00010-6.

[6] N. Cionca, D. Hashim, A. Mombelli, Zirconia dental implants: where are we now, and where are we heading?, Periodontol. 2000. 73 (2017) 241–258. doi:10.1111/prd.12180.

[7] P. Bergschmidt, R. Bader, D. Ganzer, C. Hauzeur, C.H. Lohmann, A. Krüger, W. Rüther, D. Tigani, N. Rani, J.L. Esteve, F.L. Prats, C. Zorzi, V. Madonna, S. Rigotti, F. Benazzo, S.M.P. Rossi, W. Mittelmeier, Prospective multi-centre study on a composite ceramic femoral component in total knee arthroplasty: Five-year clinical and radiological outcomes, Knee. 22 (2015) 186–191. doi:10.1016/j.knee.2015.02.003.

[8] J. Mellinghoff, Quality of the peri-implant soft tissue attachment of zirconia implants-abutments, Implants. 26 (2010) 62–71.

[9] R.B. Osman, M. V Swain, P. Dentistry, S.D. Hospital, S. Hills, A Critical Review of Dental Implant Materials with an Emphasis on Titanium, (2015) 932–958. doi:10.3390/ma8030932.

[10] K.Y. Yazdandoost, Wireless Communications for Body Implanted Medical Device, (2007).

[11] P. Anacleto, P.M. Mendes, E. Gultepe, D.H. Gracias, Micro antennas for implantable medical devices, 3rd Port. Bioeng. Meet. ENBENG 2013 - B. Proc. (2013) 1–4. doi:10.1109/ENBENG.2013.6518405.

[12] D.H. Anacleto, P., Mendes, P. M., Gultepe, E., & Gracias, 3D small antenna for energy harvesting applications on implantable micro-devices., Loughbrgh. Antennas Propag. Conf. 1 (2012) 1–13. doi:doi:10.1109/lapc.2012.6402975.

Chapter 8 - Effect of laser surface texturing on primary stability and surface properties of zirconia implants

Published in Ceramics International, 2017, 43: 15227-15236

C. G. Moura[1]*, R.S.F. Pereira[2], M. Buciumeanu[3], O. Carvalho[1], R. M. Nascimento[4], F.S. Silva[1]

[1]Centre for Micro-Electro Mechanical Systems (CMEMS), University of Minho, 4800058, Guimarães, Portugal
[2]Ceramics and Composites Materials Research Center (CERMAT)-UFSC, 88040-900 Florianópolis, Brazil
[3]Faculty of Engineering, "Dunărea de Jos" University of Galaţi, Domneasca 47, 800008 Galati, Romania
[4]Materials Science and Engineering Post-Graduate Program, UFRN, 59078-970 Natal, Brazil

*Corresponding author – C. G. Moura (caroline.materiais@gmail.com)

Abstract

The aim of this study was to investigate the influence of different laser surface texturing parameters on static and dynamic coefficient of friction values of Yttria-tetragonal zirconia polycristals (3Y-TZP) against bone to assess primary stability of implants. Ability of the textures to promote osseointegration, as measured by wettability, and eventual changes in roughness, due to possible aging during sterilization, were also assessed. 3Y-TZP disks were divided into four groups: as sintered sample, sandblasting and etching treatment, laser irradiation using an output power of 0.9 W and laser irradiation using an output power of 1.8 W. The friction tests were carried out using a pin-on-plate configuration. Pins were the 3Y-TZP disks and plates were bone. The surfaces were inspected by SEM/EDS and by surface roughness profilometer. Wettability characteristics were also evaluated by drop contact angle, and aging was assessed, after laser treatments, by XRD analysis. Results demonstrate that with laser surface texturing of zirconia it is possible to combine better wettability, better aging performance, and better primary stability, as compared to traditional - Sand blasting and Etching treatments. Thus, it is shown that the laser irradiation technique is a promising alternative to conventional sandblasting and etching procedures.

Keywords: zirconia; laser treatment; roughness; hydrophilicity; coefficient of friction.

8.1 Introduction

Yttria-stabilized tetragonal zirconia polycrystalline (Y-TZP) was introduced in the biomaterials field several years ago, mainly due to its combination of mechanical properties and aesthetic quality and durability [1,2]. Nowadays, zirconia bioceramics are often applied as implants in knee, bone screws, and dental applications [2]. Moreover, in vitro and in vivo studies also reported that the osseointegration capability of zirconia Y-TZP implants has been shown to be very similar to titanium implants, proving its suitability as an implant material [3,4]. This is possible notwithstanding the poor chemical connection with bone [5], since zirconia is a chemically inert material when introduced in human body [6].

To enhance zirconia surface properties, several surface treatments have been applied and the most common are etching, sandblasting, polishing and coating.

The conventional approach is performed by a sandblasting followed by an acid-etching, which is known to be the gold standard surface treatment [7]. It allows achieving micro-roughness values from 0.5 until 4 μm (Ra) [8]. However, the main disadvantage of this method is the potential undesirable chemical modification of the base material [9].

More recently, laser treatments have been proposed as a solution to modify the surface properties of biomaterials. This is an easily controllable and very flexible technique that promotes a rapid and oriented modification of the surface [10]. Although there are several attempts to modify zirconia surface and investigate its influence on biological response and mechanical properties, there is still little knowledge about the effects of surface modification on primary stability, as measured by static and dynamic friction response against bone. Moreover, effect of sterilization (aging) on surface roughness, and wettability is also scarce.

There are two important factors to ensure that the prosthesis mimics the mechanical and physical functions of a natural joint, which are important to mention: are the primary and secondary stability. The press-fit procedure during the total hip arthroplasty, for instance, guarantees that both the acetabulum cup and stem are anchored to the bone – referred to as primary stability – and the subsequent bone ingrowth insures the long-term bonding between the prosthesis and bone – referred to as secondary stability [11]. The integration between implant and bone is conducted by several events (e.g. surface topography and chemistry), which determines the performance of implant, and take place largely at the tissue-implant interface. The development of this interface depends on interactions of bone matrix and osteoblast with the biomaterial. Thus, the improvement of initial attachment of osteoblasts precursor cells to implant surfaces plays an important role in the bone integration of the implant and longer-term stability [12].

Furthermore, protein adsorption and subsequent cell behaviour will depend on surface topography, wettability and electric charge [13,14]. The relation between the hydrophilicity of a material surface and cell adhesion has been widely investigated, and several works have reported that high surface wettability, which means high surface energy, promote higher cell adhesion in comparison to low surface energy [15,16]. Tarumi et al. [17] studied the relation between surface roughness and wettability of zirconia after various treatments (silicone wheel polishing treatment, sandblast treatment, tribochemical treatment), and reported that by increasing the surface roughness (obtained in the case of sandblast treatment, tribochemical treatment) the water contact angle decreases thus increasing wettability.

Besides, in an implant design, other aspects have to be taken into account such as mechanical properties and tribological behaviour [18]. Tribological aspects are important, mainly during insertion of the prosthesis, which produce a friction pressure in the bone-implant interface.

Primary stability of the implants is dependent on the friction between implant and bone, and in the case of screw type implants (screws, dental implants) depend mainly on the upper surface of the threads and the bone [11].

Studies concerning the tribological behaviour, in particular, friction coefficient of zirconia against bone are very scarce. Notwithstanding, there are a few studies on this field, but only Ti and its alloys, as well as other metallic materials, against bone are included. Mischler and co-authors reported the tribological behaviour of Ti sliding against cow bone, in a lubricated medium and their results showed a severe wear of the bone, evidenced by the great amount of bone in the metal surface. The values of friction coefficient varied from 0.34 to 0.39 in their study [19]. Davim and co-authors studied the friction and wear behaviour of bovine cancellous bone against stainless steel, under water lubrification. They showed that, the prevalent mechanism found was abrasion and their average friction coefficient value was 0.25 [20]. Dantas and co-authors studied the tribological performance of Ti6Al4V bioactive composites to evaluate the friction response and surface damage. Surface treatment was also used and their results showed that the static friction increased with surface roughness (from 0.20 to 0.60), when compared to polished samples [11].

Finally, and regarding eventual surface topography changes, due to aging as a consequence of common sterilization processes, after laser surface treatments, there is also no information in literature. Thus, in this study a preliminary analysis of aging effect on surface properties, namely roughness, was performed.

It is worth to mention at this stage that the effect of laser surface treatments or textures in mechanical properties and in aging is out of the scope of this paper. Another paper is being prepared with detailed information of mechanical properties as a function of laser treatments and aging. However, it may be said at this moment that laser treatment, including texturing, is not necessarily detrimental in terms of mechanical properties.

The main aim of this study is to comprehend the friction behaviour on the implant-bone interface during the implant insertion in the bone and to evaluate the influence of surface properties of zirconia modified by laser treatment in comparison to the conventional treatment.

8.2 Experimental details

8.2.1 Preparation and surface treatment of zirconia disks

A commercial powder of 3% mol yttria stabilized zirconia – 3Y-TZP (TZ-3YB-E Tosoh, Japan) was used to produce disks with 14.5 mm radius by biaxial pressing under 200 MPa. Zirconia disks were sintered in air for 2h at 1500 °C in a heating rate of 8 °C/min, resulting in a grain size of 0.42 ± 0.031 μm. A total of 12 disks were prepared.

The 3Y-TZP disks were divided into four groups according to a surface treatment:

(i). AS – as sintered sample;

(ii). SE - sandblasting and etching treatment. The 3Y-TZP disks were subjected to grit-blasting procedure, using 100 μm alumina particles. The grit-blasting was carried out at a constant pressure of 6 bar, at a distance of 10 mm from the blasting nozzle and with an impact angle of 90° for 30s. Then, the samples were immersed in hydrofluoridine acid (48 %) for 30 minutes;

(iii). LI - laser irradiation using an output power of 0.9 Watts.

(iv). LII - laser irradiation using an output power of 1.8 Watts.

The samples were subjected to a laser treatment in order to produce a moderate and high roughness topography. For this, a Nd:YAG laser (OEM Plus 6 W, Italy) working in a fundamental wavelength of 1064 nm and a repetition rate of 20 KHz. was employed to carry out the laser treatments. The nominal focal length of the focusing lens was 160 mm. The surface samples were irradiated using two output laser power values, 0.9 Watts (LI) and 1.8 Watts (LII), with a scan speed of 15 mm/s at room temperature in air. To relieve the stresses caused by laser irradiation and recover the oxygen content to the zirconia surface, the laser irradiation groups (LI and LII) were subjected to a thermal treatment (in air) of 1200 °C for 1h with a heating rate of 5 °C/min (named here LIT and LIIT).

8.2.2. Preparation of the plates (bone)

The plates used in this study were prepared from a fresh young femur of bovine (8 months). The bone was cut into rectangular samples (4x16x20). The samples were continuously kept wet with PBS [21,22] solution during sample preparation. After machining, the bone plates were covered with gauge immersed in PBS solution and kept in the freezer until the friction tests. Before the friction tests the samples were defrosted.

8.2.3 Surface roughness measurements

After the surface treatments, the roughness was measured using a contact profilometer (Surftest SJ 201, Mitutoyo, Tokyo, Japan) at 2.5 mm measurement length and 0.25 mm/s. In the case of samples treated by laser, the profilometer ran the samples in the perpendicular direction in relation to the direction of the textures. Five measured were perfomed for each test sample. The measured surface roughness parameters were: (i) average roughness, *Ra*, (average obtained between peaks and valleys distance), (ii) skewness, Rsk, (the curve asymmetry in terms of frequency of valleys and peaks along to the profile, i.e. this parameter indicates the proportion between the amount of peaks and valleys) and (iii) kurtosis, Rku, (the distortion of the curve regarding the normal distribution).

8.2.4 Autoclave procedure

The standard steam sterilization procedure, according to ISO 13356 (134 °C, under 2 bars pressure for 1h) was performed after all the surface treatments. Monoclinic content was monitored after each treatment, including autoclave test, through XRD analysis with an incidence angle held in 2°, using Toraya modification of Garvie & Nicholson equation, considering the maximum intensities of peaks [23,24].

8.2.5 Contact angle measurements

The wettability of the zirconia discs was determined using the contact angle measurement (drop method) between the water droplet and the treated surface, using a fluid medium of de-ionized water. A drop was placed on the surface of each sample with volume controlled (0.0076 mL) and several pictures were taken by a camera. The tests were carried out at room temperature and the contact angle for each surface treatment was achieved by the average contact angle value determined using AutoCAD 2010 software (Figure 8.1). For each condition, three samples of zirconia disks were used in this test.

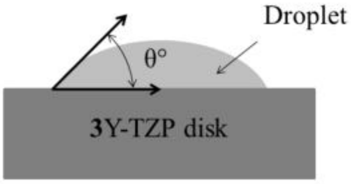

Figure 8.1 Contact angle measurements of zirconia surface.

8.2.6 Friction test procedure

To determine both the static and dynamic coefficient of friction a reciprocating pin-on-plate tribometer (Bruker-UMT-2, USA) was used. The plates were the bones. The pins were the studied materials. The bone plates were mounted in an acrylic electrochemical cell attached to the tribometer. The schematic representation of the friction tests performed in this work is presented in Figure 8.2.

The friction tests were carried out in three steps: (i). a displacement in one direction to measure the initial static coefficient of friction (Figure 8.2a – solid arrow); (iii). 17 seconds of reciprocating sliding in order to measure the dynamic coefficient of friction (Figure 8.2b) and (iii). a displacement in the opposite direction of the first reading, in order to get the static coefficient of friction after the dynamic test (Figure 8.2a – dashed arrow).

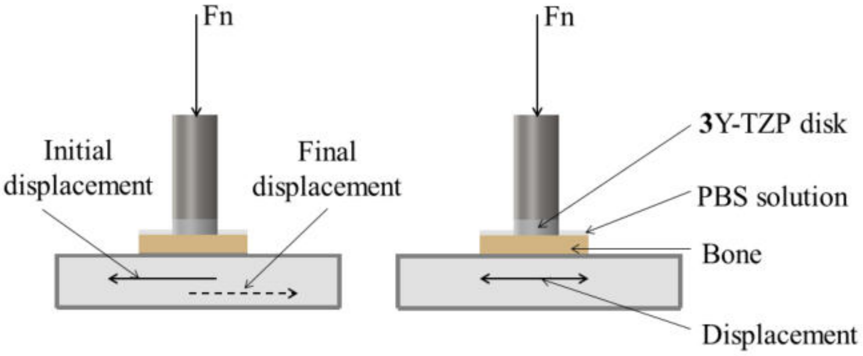

a b

Figure 8.2 Schematic representation of the friction test: (a) Initial and final static friction test and (b) dynamic friction

The friction tests were carried out by continuously hydrating the bones with a Phosphate Buffered Saline (PBS) fluid, with a normal load of 100 N on the pin, at a frequency of 1Hz and a stroke length of 5 mm of the plate. All the tests were carried out under the same conditions and the only variable was the surface treatment applied to zirconia samples. In the case of the samples treated by laser, the displacement was performed in the perpendicular direction of the texture's direction. For each condition, three samples were tested, by using a new bone plate for each test.

After reciprocating friction test, the surfaces of zirconia blocks and also of the plates (bones) were inspected by Scanning Electron Microscopy/Energy Dispersive Spectroscopy (SEM/EDS).

8.3 Results and discussion

8.3.1 Microstructural characterization

SEM images of the microstructure for all different surface treatments are presented in Figure 8.3. It can be seen a clear difference in the morphologic patterns of the zirconia surfaces.

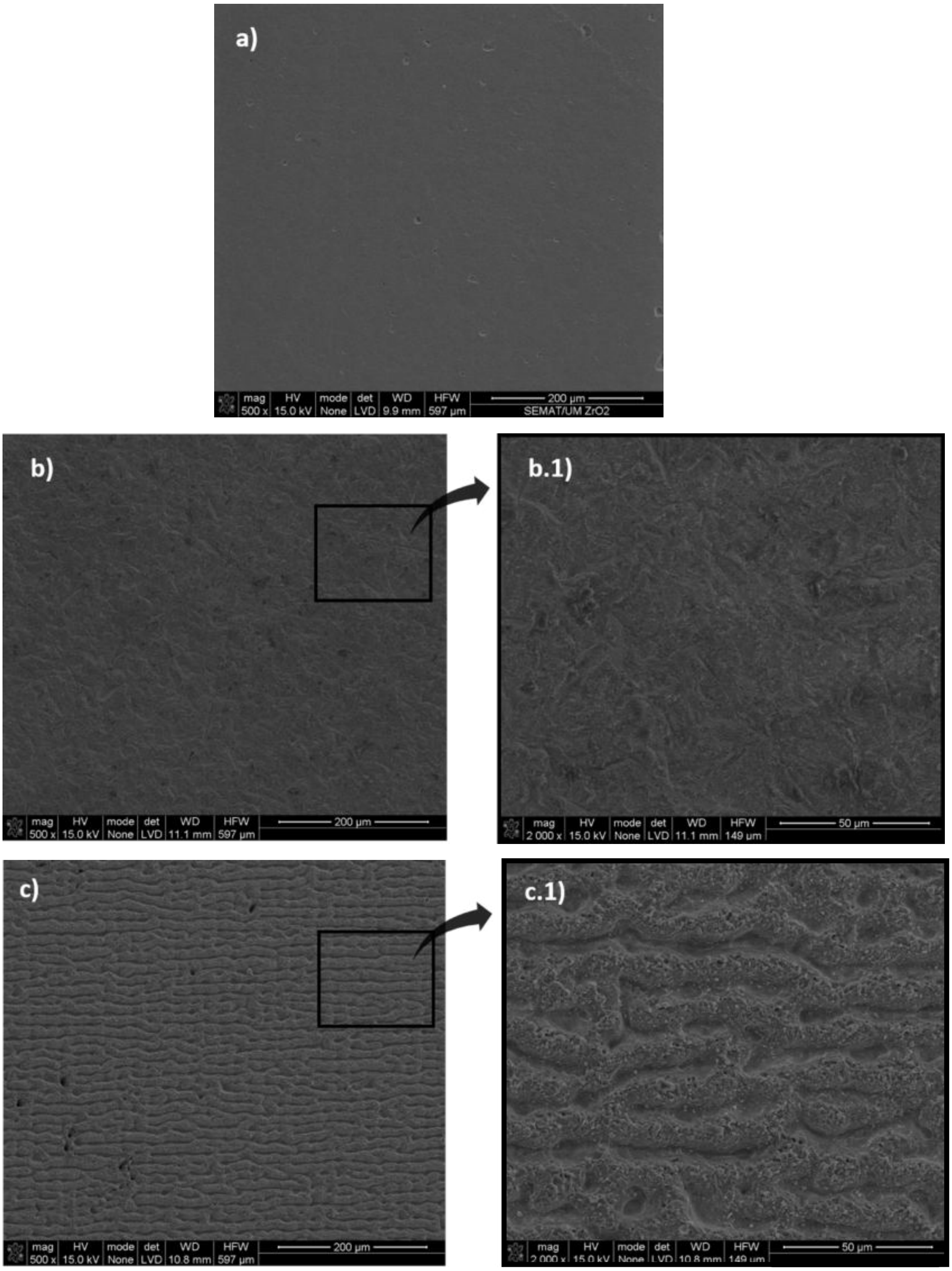

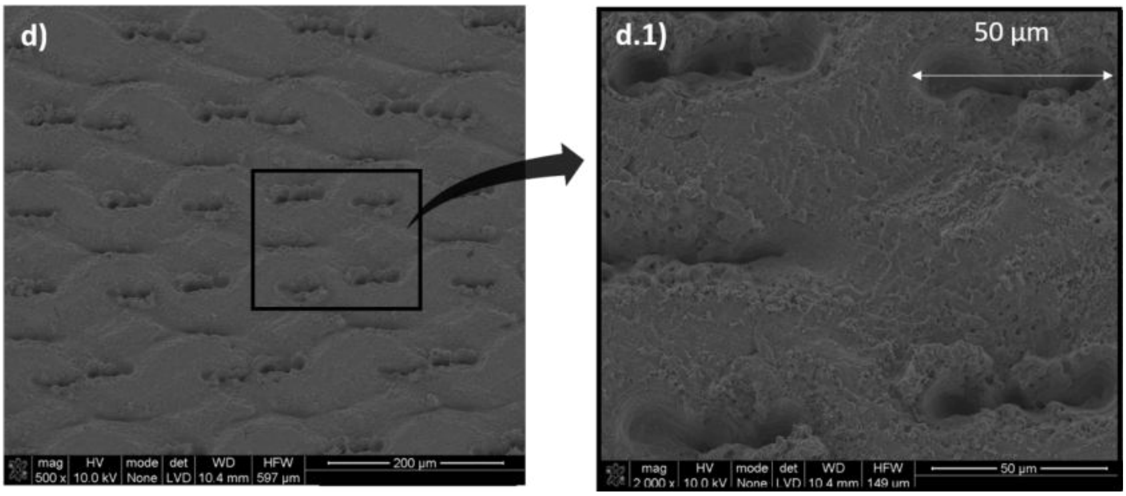

Figure 8.3 SEM images of the zirconia surfaces: (a) AS 500x; (a.1) AS 2000x. (b) SE 500x; (b.1) SE 2000x. (c) LI 500x; (c.1) LI 2000x. (d) LII 500x and (d.1) LII 2000x.

It can be observed from Figure 8.3a the smooth surface of zirconia surface, after sintering, that did not suffer any surface treatment (AS).

Figure 8.3b shows the SEM images (500× and 2000× magnification) of the zirconia disks where was applied the combination of blasting and etching treatment. This is the surface treatment that has the most clinical use in the market of the implants. It resulted into a surface with a uniform roughness throughout the surface.

In Figure 8.3c and Figure 8.3d are presented, in two magnifications, the SEM micrographs of the samples treated by laser. It seems that the roughness of the samples subjected to laser treatment is formed of two components. In the case of LI samples can be seen surface irregularities, forming cavities through the removal of material by laser (like “grooves” b – peaks and valleys), which can be considered as a micro-roughness, while from the SEM images with a higher magnification (Figure 8.3c - 2000×) can be observed that the peaks present irregularities (like a sub-micro-roughness).

The SEM micrographs, in two magnifications, of the LII samples are shown in Figure 8.3d. It can be clearly seen that the higher roughness induced in this case was obtained by a pattern formed essentially by regular pits of around 50μm length and 15μm width, surrounded by ridges.

8.3.2 Surface roughness

Surface roughness values of the zirconia discks for all different surface treatments before and after aging are presented in Table 8.1.

Table 8.1 Roughness values as function of different surface treatments

	Roughness Parameters			
	Surface Treatment	Ra (μm)	Rsk (μm)	Rku (μm)
Before Aging	AS	0.43 ±0.10	-1.72 ±2.25	12.93 ±16.65
	SE	1.24 ±0.18	-0.04 ±0.29	0.07 ±0.40
	LI	1.06 ±0.20	-0.63 ±0.70	1.80 ±3.75
	LII	2.66 ±0.31	-0.52 ±0.13	-0.13 ±0.11
After Aging	AS	0.39 ±0.25	-3.36 ±4.10	33.35 ±47.81
	SE	1.38 ±0.23	0.02 ±0.40	0.06 ±0.44
	LI	1.04 ±0.19	-0.70 ±0.28	0.50 ±0.81
	LII	2.82 ±0.38	-0.50 ±0.13	0.00 ±0.50

The description of surface morphology can be achieved using other parameters beyond the usual average roughness (Ra), such as skewness (Rsk) and kurtosis (Rku). If Rsk = 0, the number of peaks is equivalent to number of valleys. Profiles with predominance of valleys, Rsk is negative. However, if the valleys are filled, forming a plateau-peak, Rsk becames positive [25].

Regarding the, Rku roughness parameter, if Rku = 3 then the curve is Gaussian. However, for values of Rku < 3, the profile presents a few high peaks and deep valleys, while for values of Rku >3, indicate many low peaks and shallow valleys in the profile [25].

Taking into account these concepts and according to data from Table 8.1, the SE and laser groups brought an increase in roughness as compared to AS group. As expected, after surface treatments Rsk decreased, since it was created more valleys on the surface. For SE samples, according to Rsk values, the number of peaks and valleys are equivalent. Regarding the laser groups, it can be observed that by increasing the laser power energy there is an increase in roughness, resulting in two levels of roughness, an intermediate value, in the case of LI and a higher value, in the case of LII. According Rku values, the surface treatment allowed profiles with a thin form, in which, laser treatment formed few high peaks and deep valleys on the surface. All the samples were submitted to the standard steam sterilization in autoclave for 1h [26]. Roughness measures were done before and after autoclave tests to evaluate their effects, since it was already reported the influence of aging on roughness of zirconia surface [26,27]. Concerning the roughness after the standard sterilization no meaningful change was found. Maybe it can be attributed to a small change in phase transformation, as observed in Figure 8.5. It is the phase transformation that could generate expansion in some grains and consequently an increase in roughness [28]. In our case the transformation is not substantial, and the added roughness maybe included in the measurement error, since we already have a substantial roughness value, due to the surface treatments [28].

For zirconia, sandblasting and etching treatments still remain as popular choice to modify the material surface. However, the undesired contamination on the surface by the abrasive particles is still a matter of concern, in which often the acid etching treatment is not able to remove completely [29,30]. Thus, laser treatment is a novel technique to improve zirconia surface that has gained interest to replace the conventional treatments, since this method exerts no risk for surface contamination because there is no contact between the material and laser. Moreover, laser is very versatile allowing the design of the surface with any desired pattern and with desired roughness value, which is not possible with common existing surface modification techniques such as sandblasting or etching. Lastly laser is becoming a low-cost technology. In this work, laser treatment promoted surface modifications with controlled roughness and contamination-free surfaces. The laser acted over zirconia by removing content from its surface due to ablation induced by laser, forming voids. SEM analysis shows that samples irradiated by laser present a kind of melting pattern, which contributed to a Ra mean value almost eight times higher than the samples without treatment and also two times higher than the SE samples, in case of LII and slightly lower than SE for LI. This can be attributed to the formation of higher peaks and valleys, promoted by this melting pattern, that increased the Ra values.

8.3.3 Surface wettability

Considering that the surface wettability is one of the important factors in the process of osseointegration and thus, in the short and long-term stability of implant, the contact angles of the surface samples were measured. According to definition, surfaces which have contact angles of water above 90° are designated hydrophobic, while those below 90° are designated hydrophilic [31]. Figure 8.4 shows the correlation between average contact angle values and Ra as a function of different surface treatments.

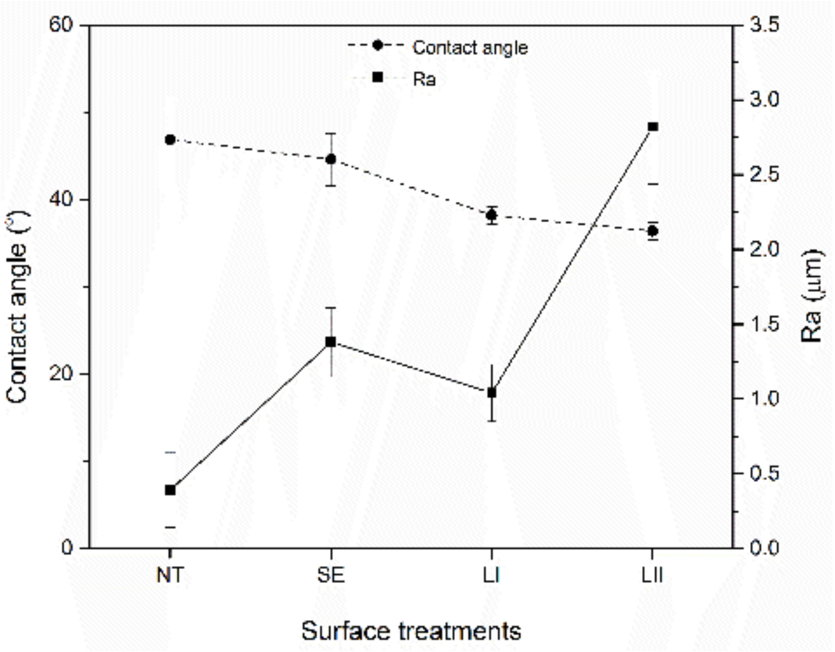

Figure 8.4 Correlation between average contact angle values and average roughness (Ra) as function of different surface treatments: AS: as sintered; SE: sandblasting and etching treatment; LI: laser treatment with 0.9 W of power; LII: laser treatment with 1.8 W of power.

The average contact angle was strongly influenced by the type of surface treatment used, because not only surface chemistry affects the contact angle, but also the surface roughness [31]. The laser groups exhibited the lowest contact angles 36.4 ± 1° for LII group and 38.2 ± 1° for LI group while the AS and SE groups presented much higher contact angles values (46.9 ± 5° for AS and 44.6 ± 3° for SE). These results showed that in the case of laser groups there is higher wettability, and it is observed a correlation between roughness and wettability.

Many studies have reported the improvement of wettability using laser treatments on ceramics surfaces [32–34]. In Hao et. al. the wettability of MgO-PSZ was proven to be improved by laser treatment compared to untreated control group [35]. Lauwrence and co-authors attributed the changes in wetting properties achieved by laser treatment to the altered surface topography, composition and energy [36]. Hao and co-authors modified the surface of MgO-PSZ using a continuous-wave laser (CO_2) and correlated the laser parameters, wettability and cell attachment. They concluded that the surface energy and surface oxygen exerted influence on the wettability, while the effect of surface roughness was not significant [35]. The investigation regarding the effects of surface characteristics on cellular response have been extensively reported. It has been shown that the surface topography, which includes surface roughness, affects cell growth and activity [37–39]. Perhaps the most important conclusion in this section is that laser surface treatments in zirconia allow control of wettability, probably as no other technique, since all type of patterns are possible with laser.

8.3.4 XRD analysis

Figure 8.5 shows the results of monoclinic content based on XRD analysis on the zirconia blocks for all different surface treatments before and after the standard sterilization in autoclave for 1h. In the graph, the studied specimens are divided in to four groups: No aging (represents the monoclinic content of all samples after the surface treatment applied), LI + thermal treatment and LII + thermal treatment (indicates the monoclinic content of the samples submitted to a thermal treatment at 1200 °C after surface treatment by laser) and Aging (represents the monoclinic content of all samples after aging for 1h).

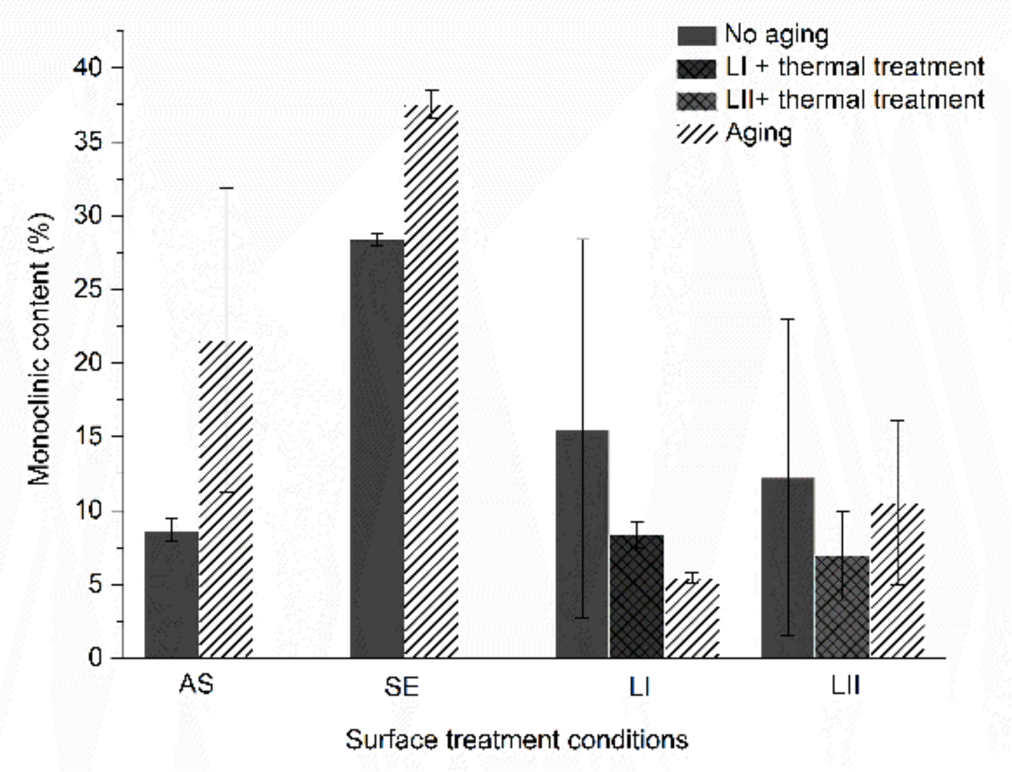

Figure 8.5 Relative amounts of monoclinic zirconia (Xm in %) on the surface of 3Y-TZP ceramics samples before and after aging, according to the studied groups. AS: as sintered; SE: sandblasting and etching treatment; LI: laser treatment with 0.9 W of power; LII: laser treatment with 1.8 W of power; LI + thermal treatment: laser treatment I followed by thermal treatment; LII+ thermal treatment: laser treatment II followed by thermal treatment. No aging: before aging. Aging: After aging (standard sterilization in autoclave for 1h).

As already stated, surface treatments in zirconia lead to damage in its microstructure, followed by the monoclinic transformation on surface (which is called low temperature degradation LTD). LTD has been associated to the roughening of the implants after steam sterilization [40]. The relative amounts of the monoclinic phase on zirconia surface were measured in untreated (control) and surface-treated specimens. These measurements were done in each group, after the treatment and also after the steam sterilization. However, since laser treatment causes changing color on zirconia surface, due to the exposure to elevated temperature gradients followed by oxygen loss, a thermal treatment at 1200 °C was performed. This thermal treatment was able to make the samples recover the oxygen content and thus regaining the white color. In this case, the monoclinic content was also measured after the thermal treatment.

Some works reported that during laser treatment, local temperature changes might create internal tensions, which consequently spreads gradually along the surface and penetrates into the depth of the material. Thus, laser treatment can induce tetragonal to monoclinic phase transformation of zirconia, which is harmful to mechanical characteristics [41–44]. However, as can be seen in Figure 8.5, the highest amount of the monoclinic phase was found after sandblasting and etching treatment, when compared to the control group (as sintered). Inokoshi et al. also reported that sandblasting treatment on zirconia surface resulted in the highest monoclinic content when compared to untreated samples. They studied the influence of zirconia surface treatments on aging behavior, however, laser treatments were not included [45].

In this present study, we concluded that laser treatment allowed to achieve desired roughness with less monoclinic transformation in comparison to sandblasting and etching treatment. After steam sterilization, there was no relevant change on the monoclinic content for the laser groups, while for SE group the low temperature degradation was significant.

Although not the focus of the present paper it is interesting to observe that laser treatment enhanced aging resistance of samples compared to the samples subjected to SE treatment. This issue will be explored in detail in another paper of the same authors.

8.3.5 Static and dynamic coefficient of friction

Figure 8.6 shows a representative evolution of the coefficient of friction (COF) - with time for zirconia disks sliding against bone (as sintered sample). Figure 8.6a shows the difference between the static and dynamic coefficient of friction values. The evolution of COF is similar for all the tests performed.

When two bodies are in contact in relative motion, the static friction force represents the force necessary to start the movement (µs – static coefficient of friction) and the dynamic friction force is the resistance to the movement (µd – dynamic coefficient of friction). Typically, the dynamic coefficient of friction is smaller than the static coefficient of friction. In this particular case, at the end of the dynamic test (representing the implantation), after approximately 170 mm of relatively displacement, the movement stopped for some seconds (2s) and it was carried out another static friction test (Figure 8.6b). This final static friction test may be important to prove the adhesion of the bone to the implant, after implantation, representing primary stability of the implant. It can be observed that, the final static COF value is higher than the dynamic COF and higher than the initial static COF.

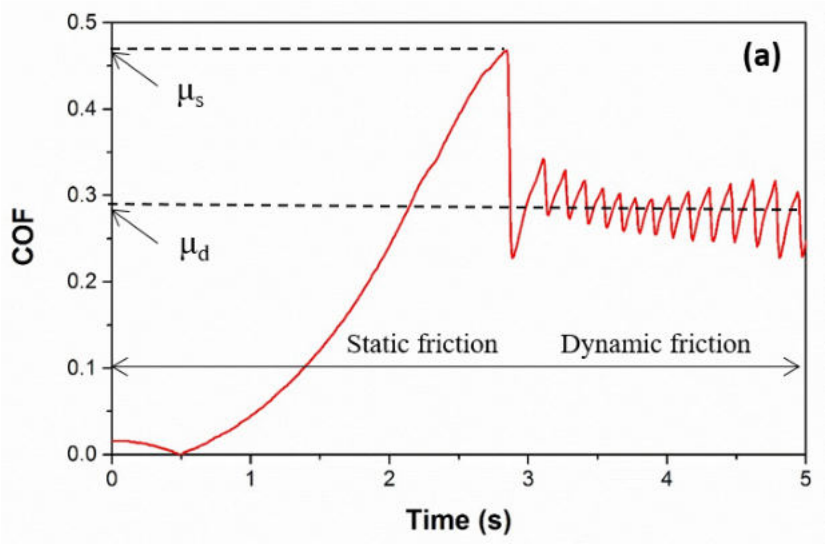

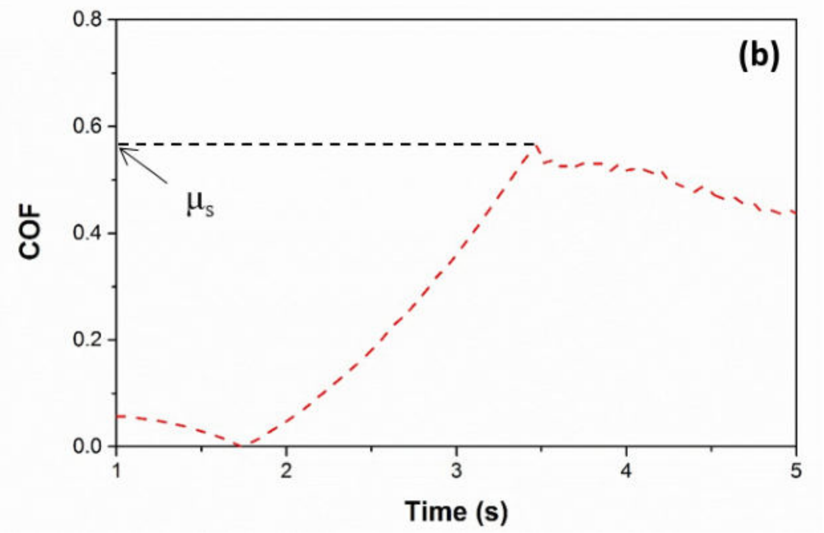

Figure 8.6 Evolution of the COF with time: (a). initial static and dynamic COF and (b) final static COF.

According to the available literature, both static and dynamic coefficient of friction values resulted from several mechanisms, which depends on geometry of the contact, properties of the contact materials, surface integrity (roughness parameter), conditions used in the friction tests (loading, sliding speed etc.) and operating conditions such as lubricated or unlubricated conditions (surface wettability) etc. [46–50]. Regarding the static coefficient of friction, it has been reported that the most important parameters that influence its value are the chemical composition and morphology of the surfaces [47].

Figure 8.7 shows the average values of static and dynamic coefficient of friction as a function of the surface treatments.

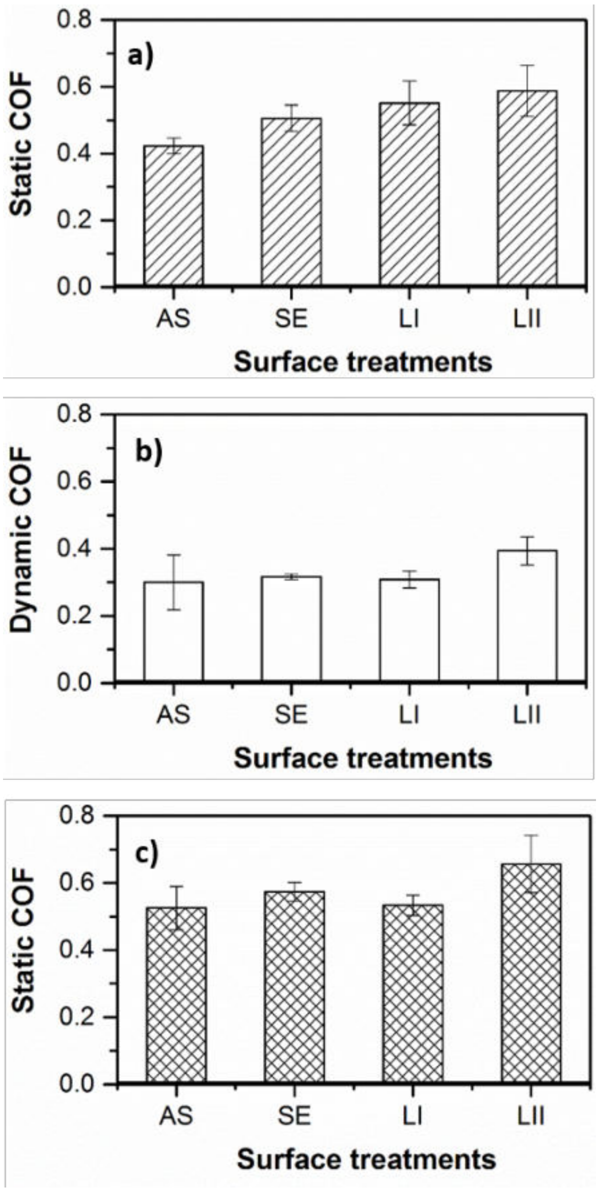

Figure 8.7 Average coefficient of friction (COF) as a function of the surface treatments: (a) initial static COF, (b) dynamic COF and (c) final static coefficient of friction.

In the case of zirconia disk/bone tribo-system, the average initial static COF values increased from 0.42 to 0.51 when changing from AS group to SE group. The initial static COF values increased more in the case of laser groups. It can be seen from Figure 7a that the static COF value was 0.55 in the case of LI group and slightly higher in the case LII group, 0.59. Thus, based on the initial static COF values, among all the studied cases, it can be highlighted that in the case of laser samples/bone tribo-systems, it is necessary a higher energy to initiate the motion between the bone and zirconia disk.

As expected, the values of static coefficient of friction were higher when compared to the values of dynamic coefficient of friction. Usually, the dynamic COF is considered to be 70% of the static COF [49]. Based on the explanation of Bowden and Tabor [51], this is related to the chemical bonding between bone and implant material.

As can be seen, it was not found a significant difference in the dynamic coefficient of friction values, among the studied cases. Although the roughness increased, it was found just a slight increasing tendency in the dynamic COF values, in which it was more pronounced in the case of LII/bone tribo-system (0.4). This fact may prove that, in this case, the roughness induced by laser is still valid after the bone adhesion (imprisonment) to the zirconia disk.

Regarding the final static COF, the values were much higher when compared to the initial static COF ones. This increase of final static COF may be attributed to the good adhesion of the bone to the zirconia disks. Thus, based on the final static COF values, it is necessary a higher energy to move bone against zirconia disk, in the case of LII/bone tribo-system. In this case (LII group), the final static COF increased from 0.53 to 0.66, which seems that the adhesion component of friction is very active in this case.

The COF results validate the roughness responses, but the effect seems to be more marked in the case of static coefficient of friction. This can be related to the fact that, firstly, the contact is between the pick of asperities (smaller contact areas), then, when the sliding starting, after few cycles all the valleys/voids are filled/covered by bone. From this moment, the effect of roughness seems to be minimized (a new surface was formed). Regarding the relation between roughness and coefficient of friction, contradictory results were reported [52,53]. If the normal load is lower, a significant influence of the roughness on the COF value was observed, while for a higher contact load, the influence of roughness on the static friction is less significant [53]. This is due to the high normal load, which leads to an increase into the contact area (increase of the number of asperities in contact) [48]. As stated by Panagouli et al. [52], the interlocking phenomena is more pronounced in the case of rough surfaces.

8.3.5 Surface analysis after the friction tests

Figure 8.8 shows the SEM images (with two different magnifications, 500× and 2000×) of the zirconia disks after the friction tests for all the surface treatments. It can be noticed substantial differences in the topographies.

In order to identify if the bone adhered the zirconia disks, EDS analysis were performed in the marked zones (Z1 and Z2). The results of the EDS analysis are presented in Table 8.2.

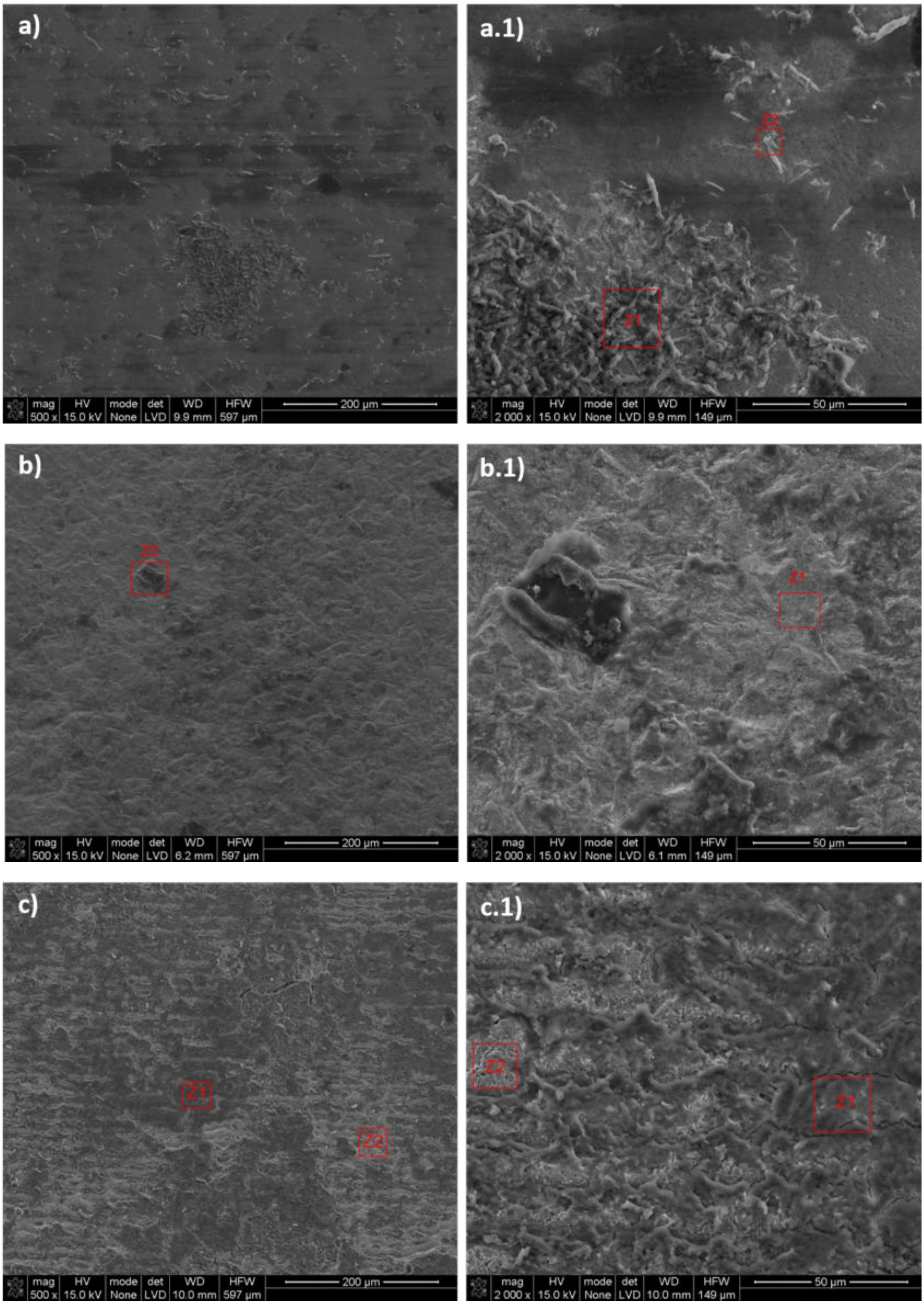

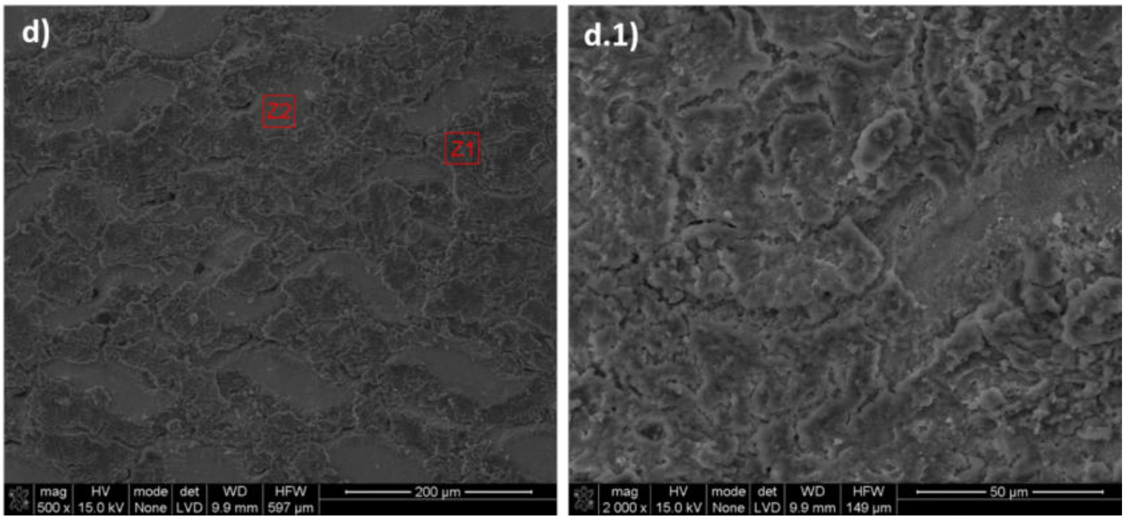

Figure 8.8 SEM images of zirconia samples after the friction test against bone: a) AS 500x; a.1) AS 2000x. b) SE 500x; b.1) SE 2000x. c) LI 500x; c.1) LI 2000x. d) LII 500x and d.1) LII 2000x.

Table 8.2 Chemical composition (wt.%) of the marked zones (Z1 and Z2) in Figure 4 for all zirconia samples after friction tests, obtained by EDS

Zones	Elements	AS	SE	LI	LII
Z1	Zr	20.05	22.74	9.02	9.84
	Y	5.94	4.46	5.45	5.28
	Ca	17.50	1.95	24.09	23.43
	P	7.23	1.01	11.07	9.87
	O	29.18	17.99	33.83	32.44
	C	16.33	50.66	13.04	16.28
Z2	Zr	33.70	18.39	48.32	49.74
	Y	7.09	3.67	8.66	8.72
	Ca	9.99	3.04	5.69	4.50
	P	4.75	1.89	3.36	2.66
	O	27.69	22.07	24.58	23.52
	C	14.61	49.04	9.38	10.01

It can be observed from Figure 8a (as sintered sample – AS), some slight sliding grooves on the zirconia disk (aligned with the sliding direction) and also material (bone) adhered all over the surface.

EDS analysis revealed the presence of Zr and Y from the zirconia disk as well as calcium (Ca) and phosphorus (P) that are common chemical elements on bone tissue composition, which confirms the transfer of the bone to the zirconia samples (suggesting an adhesive mechanism). This transfer is observed in case of all the studied cases. It should be highlighted that in the case of SE samples (Figure 8.8b) there are localized bone adherence. However, comparing the different treatments, the surface morphology achieved by laser treatment allowed a higher bone imprisonment on surface. A little amount of bone was found on surface of samples treated by SE, even compared to untreated samples, which seems that zirconia naturally has a good chemical affinity with bone.

As known, implant surface characteristics, including roughness have influence on primary stability, since the rough surface allows a firmer mechanical link to the surrounding tissues [54]. Several works have reported the importance of a high bone-to-implant contact for primary stability and how much this can be improved through surface treatments of the implant [55,56].

As the average roughness of the AS group was around 0.39 ±0.25 μm, it should be highlighted that the increase of COF value is not due to the roughness, but it is due to the chemical affinity between the bone and zirconia disk as all over the surface after the friction test is bone (Figure 8.8a). The samples treated by laser at condition I (LI), show on the surface two types of regions, smooth regions, where the bone was adhered to the surface (regions where the cavities are covered by bone), and some rougher regions, where all the cavities created by laser were filled. However, it is still possible to see the picks of the cavities (Figure 8.8c). In the laser treatment, in condition II (LII), the samples show regular pits (see Figure 8.3d). The formation of these pits increased the surface roughness as compared to the SE group. It seems that the bone filled all the pits created by laser.

The results indicated that the surface treatments play a relevant role into the coefficient of friction and surface properties of zirconia, and consequently into the connection between zirconia and the bone.

It is well known that the coefficient of friction has a major influence on stability and, as consequence, on the lifetime of the implant. Since during insertion of the implant the bone is in contact with the peaks of the asperities (depending on the distribution of the asperities), the roughness may has influence on the static friction. The influence of roughness on the static COF was also reported in [47].

According to available literature, during the lifetime of implant, in order to avoid retraction of the bone and space closure, a low coefficient of friction is required. However, during implantation (insertion of the implant) seems that a high coefficient of friction may leads to a better initial stability and, as a consequence, to a long lasting stability of the implant [57,58]. Also, Biemond et al. [59] proved that the coefficient of friction value has direct effect on the stability of implant to the bone surface.

This work puts in evidence the laser surface treatment as a promising alternative to conventional surface modifications, since it brings a good control of the roughness, which allowed an enhance of bone adhesion and surface wettability. In additional, regarding monoclinic transformation on the surface, laser treatment allowed less monoclinic transformation when compared to conventional methods, being a great advantage in terms of mechanical issues and lifetime of implant.

8.4 Conclusions

1) Surface treatments played a significant role on the friction behaviour of the bone/ 3Y-TZP disks tribopair. The initial static coefficient of friction, which represent the initial moment of implantation, was higher in all laser groups. The dynamic coefficient of friction, representative of the contact between bone and implant during the primary stability, was higher for the samples of group LII when compared to SE surfaces of zirconia.
2) Regarding monoclinic content, it was observed in laser treatment a less amount of phase transformation, when compared to SE treatment;
3) The roughness has a more pronounced effect in the static coefficient of friction value then in the case of dynamic coefficient of friction;
4) There is a higher chemical affinity between bone and 3Y-TZP disks when the laser treatments were used, which promoted a higher bone imprisonment on surface.
5) Laser treatment seems to be a promising alternative to conventional sandblasting and etching procedure to promote surface modifications with controlled roughness and contamination-free of zirconia.

Conflicts of interest

The authors have no conflict of interest to declare.

Acknowledgements

This work has been supported by FCT (Fundação para a Ciência e Tecnologia -Portugal) in the scope of the projects UID/EEA/04436/2013 and NORTE-01-0145-FEDER-000018-HAMaBICo. Thank the Cnpq and CAPES for financial support.

References

[1] A.S. Rizkalla, D.W. Jones, Mechanical properties of commercial high strength ceramic core materials, Dent. Mater. 20 (2004) 207–212. doi:10.1016/S0109-5641(03)00093-9.

[2] A. Sundh, G. Sjögren, Fracture resistance of all-ceramic zirconia bridges with differing phase stabilizers and quality of sintering, Dent. Mater. 22 (2006) 778–784. doi:10.1016/j.dental.2005.11.006.

[3] M. Gahlert, S. Roehling, C.M. Sprecher, H. Kniha, S. Milz, K. Bormann, In vivo performance of zirconia and titanium implants: A histomorphometric study in mini pig maxillae, Clin. Oral Implants Res. 23 (2012) 281–286. doi:10.1111/j.1600-0501.2011.02157.x.

[4] R. Depprich, H. Zipprich, M. Ommerborn, C. Naujoks, H.-P. Wiesmann, S. Kiattavorncharoen, H.-C. Lauer, U. Meyer, N.R. Kübler, J. Handschel, Osseointegration of zirconia implants compared with titanium: an in vivo study., Head Face Med. 4 (2008) 30. doi:10.1186/1746-160X-4-30.

[5] M. Araújo, M. Miola, A. Venturello, G. Baldi, J. Pérez, E. Verné, Glass coatings on zirconia with enhanced bioactivity, J. Eur. Ceram. Soc. 36 (2016) 3201–3210. doi:10.1016/j.jeurceramsoc.2016.04.042.

[6] T.J. Webster, R.W. Siegel, R. Bizios, Osteoblast adhesion on nanophase ceramics, Biomaterials. 20 (1999) 1221–1227. doi:10.1016/S0142-9612(99)00020-4.

[7] S. Park, K. Park, S. Cho, Comparison of removal torques of SLActive ® implant and blasted , laser-treated titanium implant in rabbit tibia bone healed with concentrated growth factor application, (2016). doi:10.4047/jap.2016.8.2.110.

[8] Straumann, Scientific Evidence First Edition (2011), 1–36. http://www.straumann.co.uk/content/dam/internet/xy/resources/summary/en/straumann–sla-scientific-evidence-first-edition–2011—straum/152.909-low.pdf.

[9] J.C. Balza, D. Zujur, L. Gil, R. Subero, E. Dominguez, P. Delvasto, J. Alvarez, Sandblasting as a surface modification technique on titanium alloys for biomedical applications: abrasive particle behavior, IOP Conf. Ser. Mater. Sci. Eng. 45 (2013) 12004. doi:10.1088/1757-899X/45/1/012004.

[10] L. Hao, J. Lawrence, K.S. Chian, Osteoblast cell adhesion on a laser modified zirconia based bioceramic, J. Mater. Sci. Mater. Med. 16 (2005) 719–726. doi:10.1007/s10856-005-2608-3.

[11] T.A. Dantas, C.S. Abreu, M.M. Costa, G. Miranda, F.S. Silva, N. Dourado, J.R. Gomes, Bioactive materials driven primary stability on titanium biocomposites, Mater. Sci. Eng. C. 77 (2017) 1104–1110. doi:10.1016/j.msec.2017.04.014.

[12] D.A. Puleo, R. Bizios, Formation of focal contacts by osteoblasts cultured on orthopedic biomaterials, J. Biomed. Mater. Res. 26 (1992) 291–301. doi:10.1002/jbm.820260303.

[13] M. Yoshinari, K. Matsuzaka, T. Inoue, Y. Oda, M. Shimono, Bio-Functionalization of Titanium Surfaces for Dental Implants., Mater. Trans. 43 (2002) 2494–2501. doi:10.2320/matertrans.43.2494.

[14] M. Yoshinari, K. Matsuzaka, T. Inoue, Surface modification by cold-plasma technique for dental implants-Bio-functionalization with binding pharmaceuticals, Jpn. Dent. Sci. Rev. 47 (2011) 89–101. doi:10.1016/j.jdsr.2011.03.001.

[15] J.L. Dewez, A. Doren, Y.J. Schneider, P.G. Rouxhet, Competitive adsorption of proteins: Key of the relationship between substratum surface properties and adhesion of epithelial cells, Biomaterials. 20 (1999) 547–559. doi:10.1016/S0142-9612(98)00207-5.

[16] W. Att, M. Takeuchi, T. Suzuki, K. Kubo, M. Anpo, T. Ogawa, Enhanced osteoblast function on ultraviolet light-treated zirconia, Biomaterials. 30 (2009) 1273–1280. doi:10.1016/j.biomaterials.2008.11.024.

[17] N. Tarumi, M. Uo, E. Yamaga, F. Watari, SEM observation and wettability of variously processed and fractured surface of dental zirconia, Appl. Surf. Sci. 262 (2012) 253–257. doi:10.1016/j.apsusc.2012.08.105.

[18] juan, Total Hip Arthroplasty, 2003. doi:10.2788/31286.

[19] S. Mischler, G. Pax, Tribological behavior of titanium sliding against bone, Eur. Cells Mater. 3 (2002) 28–29.

[20] J.P. Davim, N. Marques, Dynamical experimental study of friction and wear behaviour of bovine cancellous bone sliding against a metallic counterface in a water lubricated environment, J. Mater. Process. Technol. 152 (2004) 389–394. doi:10.1016/j.jmatprotec.2004.04.420.

[21] F. Bartolomeu, M. Buciumeanu, E. Pinto, N. Alves, F.S. Silva, O. Carvalho, G. Miranda, Wear behavior of Ti6Al4V biomedical alloys processed by selective laser melting, hot pressing and conventional casting, Trans. Nonferrous Met. Soc. China (English Ed. 27 (2017) 829–838. doi:10.1016/S1003-6326(17)60060-8.

[22] V.K. Balla, J. Soderlind, S. Bose, A. Bandyopadhyay, Microstructure, mechanical and wear properties of laser surface melted Ti6Al4V alloy, J. Mech. Behav. Biomed. Mater. 32 (2014) 335–344. doi:10.1016/j.jmbbm.2013.12.001.

[23] A. Kushima, B. Yildiz, Oxygen ion diffusivity in strained yttria stabilized zirconia: where is the fastest strain?, J. Mater. Chem. 20 (2010) 4809. doi:10.1039/c000259c.

[24] J. Chevalier, C. Olagnon, G. Fantozzi, Study of the residual stress field around Vickers indentations in a 3Y-TZP, J. Mater. Sci. 31 (1996) 2711–2717. doi:10.1007/bf00687305.

[25] R.A. Mezari, R.S.F. Pereira, F.J.P. Sousa, W.L. Weingaertner, M.C. Fredel, Wear mechanism and morphologic space in ceramic honing process, Wear. 362–363 (2016) 33–38. doi:10.1016/j.wear.2016.05.002.

[26] US Food and Drug Administration., Steam re-sterilization causes deterioration of zirconia ceramic heads of total hip prostheses, Http://www.fda. Gov/cdrh/steamst.html. (1997). doi:10.5772/55746.

[27] J. Chevalier, L. Gremillard, S. Deville, Low-Temperature Degradation of Zirconia and Implications for Biomedical Implants, Annu. Rev. Mater. Res. 37 (2007) 1–32. doi:doi:10.1146/annurev.matsci.37.052506.084250.

[28] K. Haraguchi, N. Sugano, T. Nishii, H. Miki, K. Oka, H. Yoshikawa, Phase transformation of a zirconia ceramic head after total hip arthroplasty., J. Bone Joint Surg. Br. 83 (2001) 996–1000. doi:10.1302/0301-620X.83B7.12122.

[29] F.P. Nothdurft, D. Fontana, S. Ruppenthal, A. May, C. Aktas, Y. Mehraein, P. Lipp, L. Kaestner, Differential Behavior of Fibroblasts and Epithelial Cells on Structured Implant Abutment Materials: A Comparison of Materials and Surface Topographies, Clin. Implant Dent. Relat. Res. 17 (2015) 1237–1249. doi:10.1111/cid.12253.

[30] B.R. Chrcanovic, N.L.C. Leão, M.D. Martins, Influence of different acid etchings on the superficial characteristics of Ti sandblasted with Al2O3, Mater. Res. 16 (2013) 1006–1014. doi:10.1590/S1516-14392013005000067.

[31] R.J. Ann Wennerberg, Tomas Albrektsson, Implant Surfaces and their Biological and Clinical Impact, 2015. doi:10.1007/978-3-662-45379-7.

[32] L. Hao, D.R. Ma, J. Lawrence, X. Zhu, Enhancing osteoblast functions on a magnesia partially stabilised zirconia bioceramic by means of laser irradiation, Mater. Sci. Eng. C. 25 (2005) 496–502. doi:10.1016/j.msec.2005.03.003.

[33] L. Hao, J. Lawrence, CO2 laser induced microstructure features in magnesia partially stablised zirconia bioceramic and effects thereof on the wettability characteristics, Mater. Sci. Eng. A. 364 (2004) 171–181. doi:10.1016/j.msea.2003.08.011.

[34] L. Hao, J. Lawrence, Effects of Nd:YAG laser treatment on the wettability characteristics of a zirconia-based bioceramic, Opt. Lasers Eng. 44 (2006) 803–814. doi:10.1016/j.optlaseng.2005.08.001.

[35] L Hao and J Lawrence, CO 2 Laser Modification of the Wettability Characteristics of, J. Phys. D Appl. Phys. 36 (2003) 1292–1299.

[36] J. Lawrence, L. Li, On the mechanisms of wetting characteristics modification for selected metallic materials by means of high power laser radiation, J.Laser Appl. 14 (2002) 107–113. doi:10.2351/1.1471560.

[37] A.B. Faia-Torres, S. Guimond-Lischer, M. Rottmar, M. Charnley, T. Goren, K. Maniura-Weber, N.D. Spencer, R.L. Reis, M. Textor, N.M. Neves, Differential regulation of osteogenic differentiation of stem cells on surface roughness gradients, Biomaterials. 35 (2014) 9023–9032. doi:10.1016/j.biomaterials.2014.07.015.

[38] X.H. Liu, L. Wu, H.J. Ai, Y. Han, Y. Hu, Cytocompatibility and early osseointegration of nanoTiO2-modified Ti-24 Nb-4 Zr-7.9 Sn surfaces, Mater. Sci. Eng. C. 48 (2015) 256–262. doi:10.1016/j.msec.2014.12.011.

[39] R.A. Gittens, T. McLachlan, R. Olivares-Navarrete, Y. Cai, S. Berner, R. Tannenbaum, Z. Schwartz, K.H. Sandhage, B.D. Boyan, The effects of combined micron-/submicron-scale surface roughness and nanoscale features on cell proliferation and differentiation, Biomaterials. 32 (2011) 3395–3403. doi:10.1016/j.biomaterials.2011.01.029.

[40] J. Chevalier, What future for zirconia as a biomaterial?, Biomaterials. 27 (2006) 535–543. doi:10.1016/j.biomaterials.2005.07.034.

[41] A. Usumez, N. Hamdemirci, B.Y. Koroglu, I. Simsek, O. Parlar, T. Sari, Bond strength of resin cement to zirconia ceramic with different surface treatments, Lasers Med. Sci. 28 (2013) 259–266. doi:10.1007/s10103-012-1136-x.

[42] P. Kohorst, L. Borchers, J. Strempel, M. Stiesch, T. Hassel, F.W. Bach, C. Hübsch, Low-temperature degradation of different zirconia ceramics for dental applications, Acta Biomater. 8 (2012) 1213–1220. doi:10.1016/j.actbio.2011.11.016.

[43] B. Gökçe, B. Ozpinar, M. Dündar, E. Cömlekoglu, B.H. Sen, M. a Güngör, Bond strengths of all-ceramics: acid vs laser etching, Oper. Dent. 32 (2007) 173–178. doi:10.2341/06-52.

[44] M. Noda, Y. Okuda, J. Tsuruki, Y. Minesaki, Y. Takenouchi, S. Ban, Surface damages of zirconia by Nd:YAG dental laser irradiation., Dent. Mater. J. 29 (2010) 536–541. doi:10.4012/dmj.2009-127.

[45] M. Inokoshi, K. Vanmeensel, F. Zhang, J. De Munck, G. Eliades, S. Minakuchi, I. Naert, B. Van Meerbeek, J. Vleugels, Aging resistance of surface-treated dental zirconia, Dent. Mater. 31 (2015) 182–194. doi:10.1016/j.dental.2014.11.018.

[46] H.A. Ching, D. Choudhury, M.J. Nine, N. Azuan, A. Osman, Effects of surface coating on reducing friction and wear of orthopaedic implants, Sci. Technol. Adv. Mater. Sci. Technol. Adv. Mater. 15 (2014) 14402–21. doi:10.1088/1468-6996/15/1/014402.

[47] B. Ivkovic, M. Djurdjanovic, D. Stamenkovic, The Influence of the Contact Surface Roughness on the Static Friction Coefficient, Tribol. Ind. 22 (1990) 41–44.

[48] D.H. Hwang, K.H. Zum Gahr, Transition from static to kinetic friction of unlubricated or oil lubricated steel/steel, steel/ceramic and ceramic/ceramic pairs, Wear. 255 (2003) 365–375. doi:10.1016/S0043-1648(03)00063-2.

[49] H. Reza, S. Hosseinzadeh, A. Eajazi, A.S. Shahi, The Bearing Surfaces in Total Hip Arthroplasty – Options, Material Characteristics and Selection, Recent Adv. Arthroplast. (2012) 163–210. doi:10.5772/1445.

[50] I. Hasan, L. Keilig, M. Staat, G. Wahl, C. Bourauel, Determination of the frictional coefficient of the implant-antler interface: Experimental approach, Biomed. Tech. 57 (2012) 359–363. doi:10.1515/bmt-2012-0010.

[51] Bowden, F.P., Tabor, D., The Friction and Lubrication of Solids, Clarendon, Oxford., 1954.

[52] O.K. Panagouli, K. Iordanidou, Dependence of friction coefficient on the resolution and fractal dimension of metallic fracture surfaces, Int. J. Solids Struct. 50 (2013) 3106–3118. doi:10.1016/j.ijsolstr.2013.05.020.

[53] H. Jiang, R. Browning, J. Fincher, A. Gasbarro, S. Jones, H.J. Sue, Influence of surface roughness and contact load on friction coefficient and scratch behavior of thermoplastic olefins, Appl. Surf. Sci. 254 (2008) 4494–4499. doi:10.1016/j.apsusc.2008.01.067.

[54] F. Javed, H.B. Ahmed, R. Crespi, G.E. Romanos, Role of primary stability for successful osseointegration of dental implants: Factors of influence and evaluation., Interv. Med. Appl. Sci. 5 (2013) 162–167. doi:10.1556/IMAS.5.2013.4.3.

[55] A.A. Veis, S. Papadimitriou, P. Trisi, A.T. Tsirlis, N.A. Parissis, J.N. Kenealy, Osseointegration of Osseotite?? and machined-surfaced titanium implants in membrane-covered critical-sized defects: A histologic and histometric study in dogs, Clin. Oral Implants Res. 18 (2007) 153–160. doi:10.1111/j.1600-0501.2006.01316.x.

[56] M. Degidi, D. Nardi, A. Piattelli, Immediate restoration of small-diameter implants in cases of partial posterior edentulism: a 4-year case series., J. Periodontol. 80 (2009) 1006–12. doi:10.1902/jop.2009.080649.

[57] M. Dammak, M. Schwartz, L. Gustavson, Friction Properties at the Bone – Metal Interface: Comparison of Four Different Porous Metal Surfaces, J Biomech. 35 (1997) 329–336.

[58] S. Arango, A. Peláez-Vargas, C. García, Coating and Surface Treatments on Orthodontic Metallic Materials, Coatings. 3 (2012) 1–15. doi:10.3390/coatings3010001.

[59] J.E. Biemond, R. Aquarius, N. Verdonschot, P. Buma, Frictional and bone ingrowth properties of engineered surface topographies produced by electron beam technology, Arch. Orthop. Trauma Surg. 131 (2011) 711–718. doi:10.1007/s00402-010-1218-9.

Chapter 9 - General conclusions

This chapter presents the general conclusions, according to the fulfillment of the proposed objectives, the suggestions for future works and the further contributions of this thesis. Since this thesis is organized as a compilation of researches papers, which have their specific conclusion, the present chapter touch on the general conclusions intending to integrate all the studies developed in this work.

This thesis is concerned with the printing of communication system components on titanium alloy and zirconia surface resorting to laser technology. In this sense, the study was divided according to the substrate material as follows.

Ti6Al4V substrate

Chapter 3 presents a study of laser parameters on surface texturing with a detailed characterization of the textured surface. In this study the main goal was to evaluate the surface oxidation as a result of the laser texturing, mainly regarding its electrical insulation properties. The results revealed that the oxide layer formed as a result of laser texturing on Ti6Al4V surface exhibited good electrical insulation performance.

Thereafter to the study aforementioned, Chapter 4 deals with the laser printing of the silver-based micro-wires in Ti6Al4V substrate by combining different laser processes, such as: (i) laser machining (in the micro-cavity creation), (ii) laser oxidation (for generating the insulation layer) and (iii) laser sintering (for wire consolidation). In addition, the last two processes have been compared to conventional techniques, namely anodizing oxidation and hot-pressing sintering, respectively.

In comparison to the conventional techniques (anodizing method), the obtained results show that laser is a competitive approach for oxidizing the Ti6Al4V surface. Moreover, silver powder was successfully consolidated into the micro-cavity by means laser sintering. Consequently, the micro-wires printed by using only the laser approach have good results in terms of electrical conductivity, actuating as the conductor path for electrical flow.

Building on the printing of communication system components, Chapter 5 presents a possible strategy for silver-based antenna on titanium alloy substrate. Trough the simulation results, the fabricated antenna presented a great return loss in the frequency range studied. The deterioration of the outcomes in the real case can be due to the smaller dielectric insulator thickness, which was experimentally achieved. The most challenge task was linked to the drawing up of a dense and thick insulator layer, by using only laser sintering process.

Zirconia substrate

In Chapter 6, the assessment of laser parameters on the micro-cavity creation at zirconia surface was undertaken. The concerned study was mainly directed to the laser printing of conductive micro-wires on ZrO2 surface, with minimal damage to its mechanical properties. The results showed that the approach used allowed to print micro-wires with low electrical resistivity, while the mechanical strength of the samples remained at an acceptable level. Despite the results, further mechanical tests are still needed for a deep evaluation of damages caused by laser.

In the sequence of the components printing for the communication systems, Chapter 7 dealt with the laser printing of the micro-antenna on zirconia substrate, based on the previous chapter. In this regard, a set up was arranged in order to simulate the antenna in a human body environment and the transmission signal was assessed. The results revealed that the micro-antenna produced by the proposed approach is fully capable to hold a communication cavity from inside the human body to the exterior. These results validated the use of the produced antenna in an implant for data communication with the outside world.

Taking into account the application of the current research, and the possible effects caused by the printing of communication system along the zirconia-based implant surface, it seemed relevant to assess the implications brought by the laser surface treatment on primary stability of the implant (presented in Chapter 8). Comparison with a standard surface treatment was also undertaken, in which sandblasting followed by acid-etching treatment was performed to obtain a surface roughness typically used in an implant manufacturing. ZrO2-bone interaction tests were carried out to replicate, in some extension, the insertion of the implant. The obtained results, together with a high amount of adhered bone at the zirconia surface, are promising evidences that laser surface treatments can enhance the implant stability.

Overall, the results from this thesis showed that Laser Technology can be applied as a reliable tool for printing communication system components in both, metallic and ceramic-based implants. Therefore, as a rapid, innovative and versatile technique, the laser can open up a range of approaches to design new implants for the next generation, endowed with smart functions.

9.2 Further contributions of this thesis

Publications based on this PhD work:

Moura, C.G., et al. "Effects of laser fluence and liquid media on preparation of small Ag nanoparticles by laser ablation in liquid." Optics & Laser Technology 97 (2017): 20-28.

Moura, C. G., et al. "Effect of laser surface texturing on primary stability and surface properties of zirconia implants." Ceramics International 43.17 (2017): 15227-15236.

Moura, C. G., et al. "Laser surface texturing of Ti-6Al-4V by nanosecond laser: Surface characterization, Ti-oxide layer analysis and its electrical insulation performance." Materials Science and Engineering: C (2019): 109901.

Moura, C. G., et al. "Laser printing of silver-based micro-wires in ZrO_2 substrate for smart implants applications." Under review in Journal of Optics and Laser Technology (October 2019).

Moura, C. G., et al. "Laser printing of micro-electronic communication systems for smart implants applications." Under review in Journal of Optics and Laser Technology (October 2019).

Moura, C. G., et al. "A novel approach for micro-antenna fabrication on Ti6Al4V substrate assisted by laser printing for communication systems in smart implants." Submitted to Bioelectronics and Biosensors.

Moura, C. G., et al. " A novel approach for micro-antenna fabrication on ZrO_2 substrate assisted by laser printing for wireless communication in smart implants." Submitted to Bioelectronics and Biosensors.

National and International conferences resulted from this PhD work:

C.G. Moura, G. Miranda, R.M. Nascimento, F. Silva, "Production of Silver nanoparticles by pulsed laser ablation in liquid", 14th IUVSTA School on "Nano-Optics: from principle to basic research and applications", 11-15 of April of 2016, INL - International Iberian, Nanotechnology Laboratory, Braga, Portugal-
(Conference paper and oral presentation).

C. G. Moura, R. S. F. Pereira, R. M. Nascimento, F. S. Silva, “Surface modification of zirconia by Nd:YAG laser irradiation”, 7th Portuguese Congress on Biomechanics, 10-11 of February of 2017, University of Minho, Guimarães, Portugal
(Oral presentation).

C. G. Moura, R. S. F. Pereira, R. M. Nascimento, F. S. Silva, “Influence of liquid medium and laser fluence on production of silver nanoparticles by pulsed laser ablation”, Materials 2017, 9-12 April of 2017, Aveiro, Portugal.
(Oral presentation).

C. G. Moura, R. S. F. Pereira, M. Buciumeanu, R. M. Nascimento, F. S. Silva, “Effect of zirconia surface treatments on friction coefficient and surface properties”, 15th Conference and Exhibition of the European Ceramic Society (ECers2017), 9-13 of July of 2017, Budapest, Hungry.
(Conference paper).

9.1 Suggestions for future works

Based on the developed work and results obtained, some suggestions of complementary and prospective investigations may include:

- A deeper analyze regarding laser sintering process of the silver-based wires, including chemical and thermal characterizations;
- Mechanical properties assessment of Ti6Al4V after micro-components printing;
- Carry through further mechanical tests regarding ZrO2 substrate upon micro-components printing. Efforts should be conducted to minimize laser damages on zirconia substrate.

In a broader perspective:

- Keep on building the system by adding the following layers of material, in order to insulate the wire and antenna from the superior layer. In Ti6Al4V substrate, an insulator layer is required, which can be performed by zirconia or titanium oxide.
- The integration of the communication system with the smart implants, such as actuators and sensors should be undertaken, in order to validate its operation.
- Present the final prototype and evaluate the antibacterial effects, biocompatibility and bioactivity.